Thermodynamic and Gasdynamic Aspects of a Boiling Liquid Expanding Vapour Explosion

Thermodynamic and Gasdynamic Aspects of a Boiling Liquid Expanding Vapour Explosion

Proefschrift

ter verkrijging van de graad van doctor
aan de Technische Universiteit Delft,
op gezag van de Rector Magnificus Prof. ir. K.C.A.M. Luyben,
voorzitter van het College voor Promoties,
in het openbaar te verdedigen
op donderdag 29 augustus 2013 om 15:00 uur
door

Mengmeng XIE

Master of Science in Computational and Experimental Turbulence
Chalmers University of Technology, Sweden

geboren te Shandong, China P.R.

Dit proefschrift is goedgekeurd door de promotor:

Prof. dr. D.J.E.M. Roekaerts

Samenstelling promotiecommissie:

Rector Magnificus,	voorzitter
Prof. dr. D.J.E.M. Roekaerts,	Technische Universiteit Delft, promotor
Prof. dr. ir. T.J.H. Vlugt,	Technische Universiteit Delft
Prof. dr. ir. C. Vuik,	Technische Universiteit Delft
Prof. dr. R.F. Mudde,	Technische Universiteit Delft
Prof. dr. ir. B. Koren,	Technische Universiteit Eindhoven
Prof. dr. D. Bedeaux,	Norwegian University of Science and Technology
Dr. ir. J. Weerheijm,	TNO

ISBN 978-90-8891-674-8

Keywords: BLEVE, Tunnel Safety, Shock, PLG, Non-equilibrium thermodynamics

The research described in this thesis was performed in the section Reactive Flows and Explosions, of the department Multi-Scale Physics (MSP), of Delft University of Technology, Delft, The Netherlands.

Printed by: Proefschriftmaken.nl || Uitgeverij BOXPress
Published by: Uitgeverij BOXPress, 's-Hertogenbosch, The Netherlands

Dedicated to my family
and
in memory of Zhengchuan Su

Financial support
This project was financially supported by the Delft Cluster (www.delftcluster.nl), project Bijzondere Belastingen : Ondiep Bouwen.

Contents

CHAPTER 1

INTRODUCTION

1.1 BLEVE and tunnel safety

The risk of explosion due to rupture of a truck filled with pressurised liquefied gas (PLG) is one of the risks to be considered in the context of studies on tunnel safety. When a vessel containing liquid well above its boiling point at normal atmospheric pressure fails catastrophically, a Boiling Liquid Expanding Vapour Explosion (BLEVE) can occur. A vessel containing PLG can rupture due to the consequences of mechanical impact and or external fire. Because at ambient pressure the thermodynamic equilibrium state of PLG is the gaseous state, after the sudden depressurisation caused by the vessel rupture, a rapid vapourisation takes place possibly leading to blast waves propagating in the surroundings and possibly damaging the tunnel wall and tunnel structure. On the other hand, projectile damage from the container pieces and impingement damage from ejected liquids and solid is also possible.

The motivation for this study on thermodynamic and fluid dynamic aspects of a BLEVE is the need for more accurate predictive models for explosion hazards in tunnels. The topics of investigation in this thesis are the rapid vapourisation immediately following rapid depressurisation and the creation of an overpressure close to the vessel. These phenomena can be described using thermodynamics and fluid dynamics. Other aspects of the event of tank rupture and explosion in

a tunnel are the mechanics of vessel rupture and the mechanics of the impact of the pressure waves on the tunnel wall and the surroundings were studied in other parts of the project.

It should be remarked that in the literature on safety engineering, BLEVE often refers to a chemical explosion, occurring after the ignition of the released flammable vapour. Here we do not use the term in that sense and the term BLEVE is used to denote the physical explosion due to rapid vapourisation. As a consequence this study not only covers explosion of a flammable PLG, e.g. propane, but also explosion of a non-flammable PLG, e.g. carbon dioxide (CO_2). The occurrence of a physical explosion of a flammable PLG not followed by chemical explosion is possible because (i) the tunnel geometry limits the supply of the oxygen compared to the amount needed for combustion of a flammable PLG; (ii) a preceding external fire can result in an oxygen-lean environment. Due to its relatively weak explosive effect, compared to chemical explosion, and the complexity of the phenomenon, the physical BLEVE has rarely been studied in large scale experiments of safety engineering, and relatively few relevant large scale experimental data are available.

In general, vessel failure can have several causes such as an external fire, mechanical impact, corrosion, excessive internal pressure or metallurgical failure (2, 20, 47). This leads to many possible scenario's to be considered. Here we only consider those of direct relevance for our study.

1.1.1 Tank rupture by mechanical impact

Imagine a PLG tank suffering a mechanical impact in a tunnel, e.g. due to a road accident. The mechanical impact leads to a crack on the tank wall. Depending on the crack geometry and the strength of the tank wall, there are two possibilities of the tank wall: 1) total tank rupture; 2) non-total tank rupture.

In the case of non-total tank rupture, the crack will either remain unchanged or develop into a larger opening without leading to total tank rupture. In this case, PLG liquid will be ejected from the opening and vapourise in the surroundings, e.g. on the ground. On the other hand, because the containment is lost, the PLG in the tank can not remain at high pressure and phase transition occurs inside the tank also. So the PLG liquid jet will change into a two-phase mixture jet. Because the vapourisation of PLG liquid occurs gradually at various locations (on the ground

and in the jet), there is only a low probability that a blast wave is generated and if it is generated, it is a local phenomenon and will not propagate along the tunnel.

In the case of total rupture, the tank is fully opened, separated into several parts and parts of the tank can be projected a certain distance away from the PLG liquid. Total tank rupture occurs when the initial crack is generated rapidly and rapidly develops further in a crack of the size of the vessel. In this case the boundaries of the liquid are in contact with the surroundings at ambient pressure and the initial conditions is created for a very rapid vapourisation of a large part of the liquid, which is essential necessary condition for the creation of a significant blast.

1.1.2 Tank engulfed in fire

Another possible incident is the occurrence of a fire engulfing a PLG tank in a tunnel. Due to the heating of the tank by the fire the temperature and pressure in the tank will rise and also the mechanical properties of the vessel wall will change. This can lead to conditions of tank rupture even if the tank was still undamaged before the fire started. It can lead to variants of BLEVE starting from different initial temperature and pressure than the conditions during normal transport.

1.2 Important concepts

Before addressing the key issues in BLEVE research, some important concepts need to be introduced and/or clarified.

1.2.1 Two superheat limits

As will be explained in detail in Chpt.(3), the thermodynamic states of a substance at various pressures and temperatures are described by an equation of state (EOS). Fig.(1.1) shows a typical $p-v$ (pressure-specific volume) diagram for a cubic EOS. A cubic EOS is called such because it can be written as a cubic function of the specific volume v. The isotherm at temperature T is $abefb'd$. c is the critical point. bcb' is the saturation curve or the binodal. b and b' are equilibrium states on the binodal. p_{sat} is the equilibrium pressure at T.

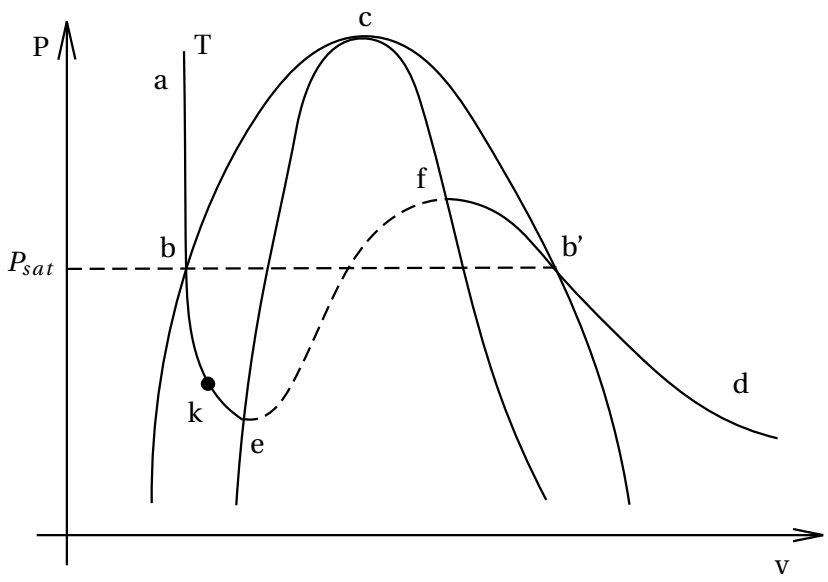

Figure 1.1: $p-v$ diagram for a cubic EOS. Coexistence line (bcb'), isotherm at equilibrium ($abb'd$), liquid spinodal (ce) and vapour spinodal (cf).

When the liquid state is between a and b, it is called the subcooled liquid. The liquid at point b is called the saturated liquid. When the liquid state is between b and e, it is called the superheated liquid because its temperature has been higher than the saturation temperature of its pressure or its pressure has been lower than the saturation pressure of its temperature. When the liquid becomes superheated, it also becomes metastable which means its stability can be easily broken by external perturbations. If so, it can no longer maintain its liquid state and phase transition must occur. When the metastability of the liquid becomes larger (the liquid is approaching point e), the minimum perturbation required to break the stability of the liquid becomes smaller and finally at point e, the thermodynamic stability limit has been reached, which means phase transition will spontaneously occur without any external perturbations. The stability of the liquid can be broken by the density fluctuations of the liquid itself. Point e is called the thermodynamic superheat limit (TSL) of the liquid and ce is called the superheated liquid spinodal or briefly the liquid spinodal.

Correspondingly, we also have the superheated vapour between b' and d; the sat-

urated vapour at point b'; the supercooled vapour between f and b' and point f is called the thermodynamic supercooling limit of the vapour and cf is called the supercooled vapour spinodal or briefly the vapour spinodal. Unstable states are shown by the dash curve ef.

Because of the relevance for the BLEVE phenomenon and for reason of simplicity, the following discussion is limited to a discussion of instability of the liquid. The thermodynamic superheat limit (TSL) has a clear mathematical definition from the stability analysis (23) as

$$\left(\frac{\partial p}{\partial V}\right)_{T,N} = 0 \tag{1.1}$$

in which N is the number of the molecules. Any cubic equation of state can be used to predict this TSL. The phase separation occurring at the TSL is called spinodal decomposition. Experimentally the spinodal decomposition has only been observed by light scattering techniques at a temperature very close to the critical point in binary mixture systems and the process is too fast to allow transient measurement of thermodynamic properties. Detailed information on the spinodal decomposition can be found in (23). Direct correspondence between a BLEVE and the spinodal decomposition has never been proven by experimental data.

In experiments on superheating of a liquid, bubble nucleation (generation of small bubbles) will start when point k on the isotherm in Fig.(1.1) is reached, and before the point e of the TSL is reached. Point k is called the kinetic superheat limit (KSL). The KSL can be measured experimentally provided early bubble generation by impurities of wall effects is prevented. When the term superheat limit is used, it can refer either to the KSL measured from experiments or to the TSL predicted by an EOS. Therefore confusion can arise when the distinction between the two superheat limits is not taken into account. In R.C. Reid's superheat limit theory (68) which will be introduced in Chpt.(2), Reid attributes the severity of the hazard of a BLEVE to the fact that the KSL has been reached, not the TSL. Abbasi et al. (1) presented an evaluation of seven cubic equation of state by comparing the TSL predicted by these EOS with the experimental KSL at atmospheric pressure and did not clearly make the distinction. The accuracy of an equation of state to predict the TSL can not be demonstrated by such comparisons unless the measured KSL has been proven to be very close to the real TSL, which has not been done in any experiment yet. Throughout a study on BLEVE one should bear in mind the difference between the two superheat limits definitions and the differ-

ence between the an experimentally observed phenomenon (KSL) and a theoretical thermodynamic property (TSL).

1.2.2 Homogeneous and heterogeneous nucleations

When a liquid becomes superheated, vapour embryos can be formed because the excess energy of the superheating can be used to cover energy needed for phase change and to maintain surface tension. This process called bubble nucleation, has two forms, depending on the locations where vapour embryos form: homogeneous nucleation, as the name indicates, occurs in the middle of the fluid where no phase boundaries are present while heterogeneous nucleation occurs on phase boundaries such as rough walls or suspending solid impurities.

Fig.(1.2) indicates three modes of heterogeneous nucleation at a liquid-solid interface. To form a vapour embryo with the same volume, heterogeneous nucleation requires less energy than homogeneous nucleation because the presence of the phase boundaries allows a lower interface area of the vapour embryo. Generally speaking, heterogeneous nucleation occurs at a lower degree of superheat than homogeneous nucleation.

For a BLEVE to occur it is necessary that a large part of the liquid vapourises in very short time. This will be more easy to realise in the presence of homogeneous nucleation. In small scale experiments the surface to volume area of a container is larger than in large scale systems. Therefore in the design of small scale BLEVE experiments special attention has to be paid in the suppression of heterogeneous nucleation at wall, e.g. using polished inner wall. Also, sometimes homogeneous and heterogeneous nucleation are not easy to distinguish, e.g. when the liquid contains evenly suspended very small solid impurities or when gaseous impurities start to separate out when the liquid is getting superheated.

Nucleation phenomena are not limited to generation of bubbles in liquid. They can also occur in solid-liquid phase transition and solid-vapour phase transition. Oxtoby has written a very good review article on the subject (54).

1.2.3 Volume fraction and mass fraction

From the fluid dynamic point of view BLEVE is a two phase problem. The most basic concepts in the description of a two phase problem are volume fraction and

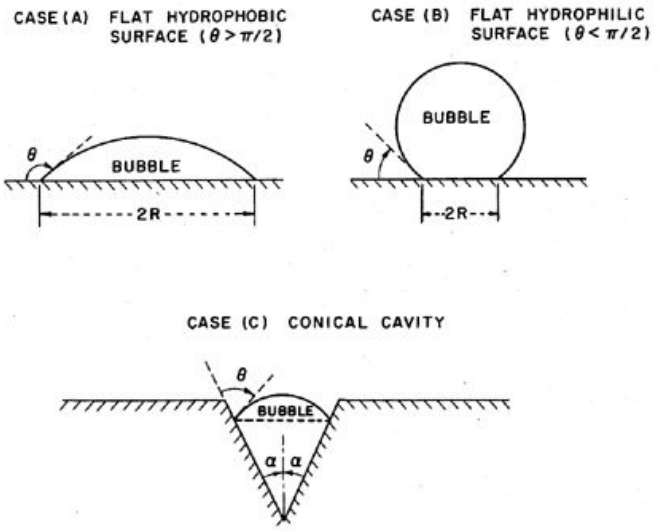

Figure 1.2: Various modes of heterogeneous nucleation. Reproduced from (13)

mass fraction of the two phases, and resulting density of the two-phase mixture. These concepts will be introduced here, because they play a important role in all chapters of this thesis. Consider a fixed region in space (control volume), filled with two phase mixture. Whatever the shape of the boundary between the phases, the volume of the gaseous part V_g and the volume of the liquid part V_l sum up to the volume of the mixture V_m

$$V_m = V_g + V_l \tag{1.2}$$

ρ_g and ρ_l are the densities of gas and liquid, respectively. For simplicity we here assume that they are constants. Mass is the product of density and volume

$$M_g + M_l = M_m \tag{1.3}$$

$$M_g = \rho_g V_g \quad M_l = \rho_l V_l \tag{1.4}$$

The volume fraction of the phases is denoted as α_g and α_l

$$\alpha_g = \frac{V_g}{V_g + V_l} \quad \alpha_l = \frac{V_g}{V_g + V_l} \tag{1.5}$$

where $\alpha_l = 1 - \alpha_g$. It follows that the density of the two-phase mixture ρ_m is given by

$$\rho_m = \alpha_g \rho_g + \alpha_l \rho_l \tag{1.6}$$

For simplicity, the volume fraction of the gases phase is also called void fraction α, hence

$$\alpha_g = \alpha \tag{1.7}$$

$$\alpha_l = 1 - \alpha \tag{1.8}$$

The fraction of the mass of the mixture which is in gaseous or liquid form can be calculated from the volume fractions and the densities of the phases via

$$Y_g = \frac{\alpha_g \rho_g}{\alpha_g \rho_g + \alpha_l \rho_l} \quad Y_l = \frac{\alpha_l \rho_l}{\alpha_g \rho_g + \alpha_l \rho_l} \tag{1.9}$$

The amount of mass in the gas phase and the liquid phase can also be written as

$$M_g = (V_g + V_l)\alpha_g \rho_g \quad M_l = (V_g + V_l)\alpha_l \rho_l \tag{1.10}$$

The density of the gas and the liquid phases referred to the volume of the mixture is

$$\rho_{g,m} = \alpha_g \rho_g = \frac{M_g}{V_g + V_l} \quad \rho_{l,m} = \alpha_l \rho_l = \frac{M_l}{V_g + V_l} \tag{1.11}$$

Both ρ_k and $\rho_{k,m}$ are physically well defined quantities, but they are different. We see that care has to be taken to make it clear whether a density is with respect to the volume of one phase or with respect to the volume of the mixture. The two quantities defined by choosing these two reference volumes are related by a factor α_k.

1.3 Key problems of BLEVE numerical simulation

As mentioned, the main features of a BLEVE can be described by combining thermodynamics and fluid dynamics. In order to create an adequate model for BLEVE simulation the following four key problems have to be addressed.

1. An appropriate simplified form of the conservation equations of mass, momentum and energy has to be formulated;
2. A solution algorithm of the model equations of two-fluid two-phase compressible flow has to be formulated;
3. An equation of state has to be chosen to describe the relations between the relevant thermodynamic variables;
4. Models have to be formulated for mass, momentum and heat transfer between liquid and vapour phase.

The challenges in dealing with the four key problems are from various aspects and often correlated. For example, there are different ways to formulate transport equations for a multi-phase multi-component flow. In the so-called Eulerian-Eulerian approach both liquid phase and vapour phase are described by continuum equations. Consistent formulation of these continuum equations is a difficult topic. In particular incorporating slip between the phases is presenting problems due to the fact that this often leads to non-hyperbolic equations and a mathematically ill-posed problem. This is avoided in our model which uses the assumption of equal velocity of liquid and vapour (in an average sense, on a length scale of several bubble or droplet diameters). This assumption seems reasonable but may be challenged at a later stage. Since heat transfer between the phases is a key feature of the phenomenon, another assumption that has been made during formulating the transport equations is the unequal temperature assumption in which separate transport equations are solved for the energy or temperature of the liquid and vapour phases. The assumption has a direct influence on the development of the interfacial flux models. The accuracy of the interfacial flux model also depends on the quality of the equation of state because only several state parameters can be directly solved from the transport equations and most state parameters are solved from the equation of state.

So the common challenge in all four key problems is verification and validation. The accuracy of an equation of state is a key parameter for evaluation during its development, therefore all we need to do is to select the best equation of state from our resources. It turns out that the solution algorithm can be verified using standard numerical test cases. In our current implementation, the one-dimensional model for BLEVE is in effect a Riemann problem with some known exact solutions, e.g. the Sod's test problems. Following (59), the numerical accuracy of our current

solution algorithm can be verified by comparing the outputs with the exact solution of the Sod test problems. These tests validate the prediction of expansion wave, contact face and shock wave in the absence of phase transition.

For the validation of the conservation equation and models of the interfacial flux, a first type of validation is by comparison of model predictions with measurements of field tests or lab-scale explosion tests. Proceeding in this way only the combined use of all submodels is validated. In case of bad agreement with experiment, it is necessary to analyze in detail which submodel is the weakest link. In the case of good agreement, one must remain aware that there may be a cancelation of errors. Therefore in a more detailed validation study, for each of the different model components the question of experimental validation can be asked. This should only be done for those components where agreement between theory and experiment is still an issue. Because we also consider the need for this detailed validation we also review available experimental data for testing each of the submodels.

An objective of this thesis work is to make an inventory of relevant experimental data for the validation of the overall model and the submodels and to evaluate whether sufficient data are available or additional experiments are needed. After a brief review of the main theoretical model for a BLEVE, the superheat limit theory, and underlying complexity of vapourisation dynamics, we consider availability of experiments on the various aspects of the problem. First we review the fundamental aspects (thermodynamic equation of state, bubble nucleation rate, bubble growth rate, evaporation fronts), then we proceed to experiments on the BLEVE phenomenon. (small scale experiments focusing on pressure evolution in the two-phase mixture, medium scale experiments reporting the far field blast effect.) Next we also consider relevant experiments from related fields (flashing, blowdown). Finally we draw our conclusions.

CHAPTER 2

LITERATURE REVIEW ON BLEVE

In this chapter a brief overview is given of the literature on BLEVE-related phenomena. The emphasis is on experiments but related modeling is mentioned. The presentation is divided in three parts: investigations of fundamental aspects, BLEVE experiments and experiments from related fields.

2.1 Theory and fundamental aspects

2.1.1 The superheat limit theory of BLEVE

The standard theory of BLEVE is the so-called superheat limit theory, originally proposed by Reid (67, 68). The essential idea is illustrated by Fig.(2.1). Under normal conditions the content of the PLG vessel containing a liquid and its vapour is in thermodynamic equilibrium and the pressure and temperature combination lies at the saturation curve (points A or C). In the case of vessel rupture the pressure suddenly decreases resulting in superheated liquid. There is a limit to the degree in which a liquid can get superheated. At constant pressure, the superheat limit temperature is the highest temperature that a liquid can sustain without undergoing phase transition and at constant temperature, the superheat limit pressure is the lowest pressure for a liquid to maintain its liquid state. The superheat limit

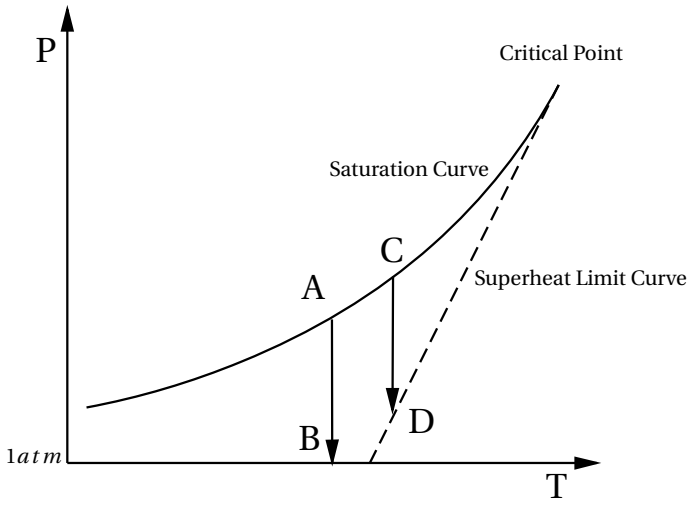

Figure 2.1: Schematic explanation of Reid's superheat limit theory for BLEVE in depressurisation processes

curve is shown as the dashed line in Fig.(2.1). According to Reid's theory, when the pressure of the liquid decreases from point C to D, the liquid reaches the superheat limit curve and a BLEVE will occur while in the process of A to B, the liquid does not reach the superheat limit curve, no BLEVE will occur. Based on our discussion in Chpt.(1), the superheat limit referred in Reid's theory should be the kinetic superheat limit (KSL).

Where does the superheat limit curve in Reid's theory locate? Although he claimed that the thermodynamic superheat limits predicted by the Redlich-Kwong equation of state is reasonably in agreement with the measured superheat limits, he doubted those results because "...no satisfactory correlation now exists to relate p, v and T in the superheated liquid region...". An equation of state is obtained by correlating experimental data outsides the saturation dome. Using an equation of state for metastable states inside the saturation dome is equivalent to extrapolation of those experimental data. For slightly superheated liquid, the extrapolation is still reliable (23), but for highly superheated liquid states, Reid's worry is inevitable. If the validity of an equation of state in predicting the thermodynamic superheat limit has not been proven, the close agreement of its predictions with the measured superheat limit can not be interpreted as matching (1). On the other

hand, Reid also mentioned the need to derive more information on the vapour bubble formation from kinetic theory, as will be done in the following chapters.

Reid's superheat limit theory is widely accepted in the literature on explosions (2), but it has not been directly proven to be true, due to the impossibility to do detailed measurements in the superheated liquid during a realistic BLEVE experiment. Direct measurements of vapourisation at the superheat limit have only been made in droplets of mm size.

2.1.2 Vapourisation dynamics of a BLEVE

In a practical BLEVE, the decrease in pressure is not felt instantaneously all over the liquid but spreads in the form of a wave. Furthermore the local temperature at different locations in the liquid may be different, depending on the features of the accident causing the vessel rupture (e.g. mechanical impact or fire) and the amount of heat used for vapourisation. As a consequence the situation in a real incident will be much more complicated than the simple trajectories from A to B or from C to D in Fig.(2.1). The starting points at different locations in the liquid may be at different locations on the saturation curve. The decrease in pressure due to opening of the vessel will be felt at different locations at different moments in time and once vapourisation starts the decreases in pressure can be stopped by the expansion of the mixture due to vapour generation. The rate of depressurisation is also controlled by the time needed for vessel rupture.

When a liquid is superheated but is still far away from the superheat limit, vapourisation will start first on locations most favorable for the formation of initial small bubbles which is on solid surfaces or on dust or other solid particles in the fluid. Once bubbles are formed they grow according growth laws which have been well-studied in the literature (61, 79).

Approaching to the superheat limit state, the process generating smaller bubbles (nuclei) is different than away from the superheat limit state because the small 'vapour' nuclei originate homogeneously in the fluid and at a much faster rate. The smallest stable bubbles close to the KSL are much smaller than away from the KSL. Classical homogeneous nucleation theory has been developed to describe this case. It turns out that its predictions of nucleation rate are extremely dependent on details. De Sá et al. (22) and Delale et al. (24) give alternative formulations of the theory to improve this situation. The growth of bubbles at the superheat

limit also proceeds in a different manner than away from the superheat limit (78).

The rapid growth of bubbles may create a rise in pressure which counterbalances the initial pressure drop, and keeps the liquid away from the superheat limit. This phenomenon must be taken into account in the evaluation of the effects of rapid depressurisation or rapid heating. In fact, the view that when a vessel ruptures, its contents 'instantaneously' reach atmospheric pressure or the superheat limit curve is not realistic. This has been taken into account in a refinement of the superheat limit theory proposed in (50). As summarized in the review (47), in (50) the homogeneous boiling only occurs at the rupture location where the liquid sucked out of the breach first reaches atmospheric pressure. Their study focuses on the liquid behavior inside the vessel (liquid hammer, pressure recovery etc.), before a possible total disintegration of the vessel.

A vapourisation front can have very complex shape and wildly fluctuating properties. The break up of existing bubbles in smaller bubbles in a wildly fluctuating vapourisation front creates extra area and also new nuclei for heterogeneous vapourisation. This can enhance the vapourisation rate and the front propagation rate enormously. The question arises whether the vapourisation in a propagating front can generate a sufficiently strong volume source for significant blast propagation.

These considerations indicate that apart from experiments and thermodynamic models to determine the superheat limit curve for various substances, also experiments and fluid dynamic models are needed to determine the propagation speed of vapourisation fronts.

2.1.3 The KSL and single vapour-bubble nucleation and growth

The generation of a BLEVE depends on rapid vapourisation. Vapourisation starts by formation of small bubbles (nucleation) and proceeds by the growth of these bubbles. Distinction has to be made between nucleation and bubble growth in the meta-stable state but still far away from the KSL and nucleation and vapourisation close to the KSL. In conditions away from the KSL, homogeneous nucleation is much less probable than heterogeneous nucleation and the question how fast the nucleation is, also involves questions on availability and properties of surfaces for nucleation.

Experiments

The standard experimental set up to determine the kinetic superheat limit of a liquid is nicely described in (67). It consists of a tall slender column filled with liquid in which a small droplet of the test fluid of which the superheat limit is to be determined is rising upwards. The test fluid must be immiscible with the column fluid and have a density which is lower than the column fluid. The droplet must be small enough to assure that it can be homogeneous in temperature. Droplets with diameter of about 1 mm are usually used. The liquid in the column is heated such that the top is significantly warmer than the bottom. When the droplet is injected into the bottom of the column, it will start to rise. If the temperature profile in the column is designed in such a way that the bottom of the column is at lower temperature than the boiling temperature and the top sufficiently larger than the boiling temperature, the droplet will pass the height where the column fluid has the boiling temperature of the test fluid, but because of absence of nucleation sites will not start to boil and enter the meta-stable region. Only when it reaches the height where the column fluid has the superheat limit temperature of the test fluid, evaporation will start. It is observed that this happens from a single nucleation site at which a bubble is formed, which grows until it the complete droplet has evaporated.

Experimental studies on the bubble growth process at the superheat limit are described in (29, 31, 46, 49, 78).

In (78), it is reported that the liquid-vapour interface in a vapour explosion process has a large-amplitude small-scale roughening during most of the evaporative stage in contrast to the smooth bubbles in conventional boiling.

Lesin et al. (46) studied the dynamic behavior of a single liquid butane droplet boiling explosively at its superheat limit and also developed a model for it.

These experiments use high speed camera observations of a single small bubble and do not enter in the question what the nucleation rate is. However it seems possible to derive from the experiments some upper limit on nucleation rate.

Modeling

The equation of state of a fluid describes the relation between the thermodynamic state variables in the equilibrium state. Therefore a priori it does not provide in-

formation on non-equilibrium properties. In particular it is not supposed to predict the superheat limit temperature. Nevertheless it is possible to extrapolate the use of an equation of state to non-equilibrium conditions. This is what usually is done to check whether the superheat limit temperature is predicted in agreement with experiments. Such studies have been made in (22), (24) and (1). In particular the study of Abbasi and Abbasi (1) gives a comprehensive set of results. It can be concluded that for the investigated substances the thermodynamic superheat limit predicted by equation of state is comparably close to the kinetic superheat limit measured from experiments, which gives a convenient method to obtain the kinetic superheat limits from equation of state directly. But it should be emphasized again that the close agreement of thermodynamic superheat limit from equation of state to the kinetic superheat limit does not prove that the real thermodynamic superheat limit or the spinodal has been reached in experiments.

When the kinetic superheat limits are measured, the next problem becomes the bubble nucleation rate at the kinetic superheat limits. Several bubble nucleation theory have been developed to predict the bubble nucleation rate with the measured superheat limit or vice versa, among which the classical nucleation theory is the first one. The classical nucleation theory assumes a macroscopic nucleus size. This theory cannot be applied to the meta-stable states close to the spinodal where the nuclei size is of the order of molecules. Oxtoby (54) discussed and reviewed classical and non-classical approaches in 1992. More recently, Delale et al. (24) systematically modified the formulations of the classical nucleation theory to obtain a formulation giving higher homogeneous bubble nucleation rates and smaller critical bubble sizes.

The nucleation process in highly superheated liquid leads to formation of vapour embryos which contain a relatively small amount of molecules. It is a challenge to extend thermodynamic concepts originally design for macroscopic systems to such small systems. This extension of thermodynamics is an active area of research in several fields of physics and chemistry. We refer to Reguera et al. (66) for developments in this area.

A general review of models for bubble growth rate is given in (79). Fairly accurate models have been developed for the rapid vapourisation of a single droplet of mm size at the superheat limit (46). Recently a new model was presented in (6). Compared to previous modeling approaches, they more accurately take into account that there is a high mass flux through the moving bubble surface. They successfully applied their model to the experiments of Lesin et al. (46) and of Frost and

Sturtevant (31).

The conclusion is that accurate models for growth rate seem to be available. The question remains how relevant a good model for the nucleation rate is. The total vapour fraction after some very short time is more determined by the growth rate than by the nucleation rate (27).

2.1.4 Evaporation fronts

Generation of a BLEVE depends on a high overall rate of vapourisation in a mass of superheat liquid. For a range of conditions vapourisation starts at the liquid air interface. The vapourisation of the bulk then follows after the passage of a rarefaction wave. This leads to the development of an evaporation front. The evolution towards a highly meta-stable state then does not occur simultaneously at all locations but follows from the passage of a rarefaction wave. The properties of the front cannot be determined solely from single vapour-bubble experiments. A thermodynamic description, giving the detailed trajectory of matter from the meta-stable liquid state to the stable liquid and stable vapour state, has to be combined with fluid dynamic description describing the overall conservation of mass, momentum and energy on a larger scale. A recent thorough study on this is (74).

A front can have a complex structure with a bubbly or foamy nature and need not be flat. The rough front has a larger area per unit volume than a flat front which increases the propagation speed of the front compared to a flat front.

Experiments

Das et al. (21) report experiments on boiling propagation in a suddenly depressurised superheated vertical column filled with water. The velocity of boiling front propagation (BFP) is found to depend strongly on liquid superheat, liquid purity and test section size. Using a similar configuration several other authors have succeeded in identifying the key properties of evaporation fronts (35, 71, 80).

These experiments consisted of connecting a vertical tube filled with a liquid in thermodynamic equilibrium at atmospheric pressure (or higher) to a very low-pressure chamber (Figure 2). As soon as the membrane between the liquid and the vacuum is ruptured, rarefaction waves propagate through the liquid producing a superheated liquid. Then a subsonic phase-transition front propagates through

the superheated liquid producing a high-velocity liquid-vapour mixture in thermodynamic equilibrium moving towards the low pressure chamber. The front velocity is much lower than the ejected mixture velocity (e.g. 1 m/s front velocity versus 100 m/s ejected mixture velocity). The experimental observations indicate that both liquid and vapour compressibility have to be considered. They also report the presence of an acoustic wave (expansion wave) preceding the evaporation front, a contact discontinuity and a compression wave. In the context of BLEVE research the properties of the compression wave are of most interest. Is it a shock wave or a continuous wave, and what is its strength?

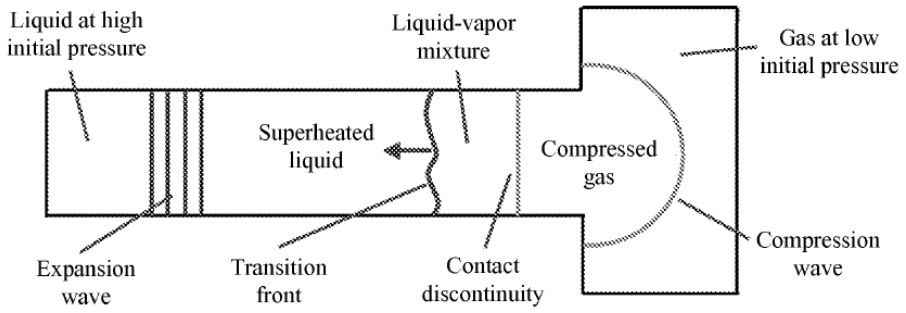

Figure 2.2: Sketch of the experimental setup of (80). Reproduced from (74). The test cell is round Pyrex glass tube, of length 340 mm and diameter 15 mm. A volume of 50 $cm3$ of liquid is evaporated. The piercing time of the diaphragm separating high and low pressure region is a few milliseconds.

Simões-Moreira and Shepherd (80) make the following observation on the range of conditions in which evaporation waves occur: "There were also definite limits of minimum and maximum superheats for which we reliably observed evaporation waves. Outside these limits, nucleation upstream of the wave would disrupt our observations. At low superheats, the evaporation wave was slow and there was a long dwell time before the onset of the wave. This required metastable fluid to be in the test cell for a long period of time, and heterogeneous nucleation would occur. At moderate superheats, the wave would start promptly and move quickly enough that heterogeneous nucleation upstream of the wave would not occur. At high superheats, the nucleation rate became so high that despite high evaporation wave speeds, heterogeneous nucleation occurred upstream of the wave."

The working fluid in their experiments is dodecane and the range of temperatures

for which evaporation waves were observed is $180 - 300°C$. The value of the superheat limit temperature is not given in the tables of (3), but it can be read from Fig.(15) of (80) that it is higher than $350°C$. Their motivation for using dodecane is the objective to generate a 'complete evaporation wave', with all liquid converted to vapour. The experimental result was that at the most extreme superheat tested, a vapour content of over 90% (mass fraction) was estimated from the measured data.

The conclusion is that the vapourisation process is in the form of an evaporation wave only at temperatures significantly lower than the superheat limit temperature.

Modeling

Detailed computational modeling of evaporation fronts has been described in (45) and (74).

Saurel et al. (74) give a review of existing models. They distinguish between two classes: 1) pressure and temperature equilibrium models and 2) temperature non-equilibrium models. In the second class they further distinguish

Six-equation model obtained e.g. by averaging mass, momentum and energy equations for two phases

Seven-equation model which has, in addition to the six equations, an equation for the volume fraction of one of the constituents

Five-equation model which is composed of two mass-balance equations, one mixture momentum equation, one mixture energy equation and a volume fraction equation and assumes equal pressure and equal velocity for both phases

The last model is the starting point of their further analysis. An original thermodynamic closure is used. The model is shown to be able to compute evaporation fronts by solving their internal structure. Metastable states are involved, as well as shock, rarefaction and interface dynamics. However the main focus of their work is on cavitation rather than on flashing.

2.1.5 Vapourisation at high vapour volume fraction

In the case of a rapid depressurisation causing a BLEVE, a multitude of bubbles will be formed and the nucleation rates and growth rates of a single bubble in a homogeneous environment may not be sufficient to describe the total vapour formation rate. E.g., the influence of neighboring bubbles on the nucleation rate has been studied in (26). When the void fraction increases, complex two phase flow patterns are expected, and guidelines for handling these can be looked for in multiphase flow studies. There different flow regimes are distinguished, depending on the volume fraction of the phases, the slip velocity and geometric aspects. The literature on multiphase flow has numerous experiments on these flow regimes, but they usually refer to steady state conditions and not to explosive systems. Risnic and Ishii (72) describe models for nucleation and bubble growth in flashing flow. The study concerns conditions of moderate superheat.

What happens in a rapid vapourisation process once the vapour fraction reaches such high values that it is no longer possible to describe the vapour as a collection of bubbles? This will depend on the ratio of heat stored in the superheat of the liquid and the heat needed for vapourisation. When all superheat has been used the vapourisation will stop, when remaining superheat is available the vapourisation will continue. But the remaining liquid will be entrained with the expanding vapour.

Clearly the flow aspects will start to play a larger and larger role once the explosion develops. We have found little or not literature describing in detail the final stages of the vapourisation process in case of vapourisation starting from homogeneous nucleation. Accordingly, accurate models for the evolution of the total area of the contact face between the phases seem to be missing. Pinhasi et al. (59) have used the concepts of flow regimes (bubbly flow of vapour fraction below 0.3, churn-turbulent flow of vapour fraction between 0.3 and 0.7, droplet flow of vapour fraction above 0.7) and taken representative area estimates, but probably better models are needed. A statistical treatment going beyond the Eulerian-Eulerian approach seems necessary (detailed characterisation of the structure of the two-phase flow, bubble/droplet number density, bubble/droplet size distribution etc.).

2.2 BLEVE research

Recently Birk and others (10) after an analysis of a number of medium scale BLEVE tests have come to the conclusion that in the case of rupture of high pressure vessels only partially filled with liquid propane (fill level in the range 0.13 to 0.61) the shock waves observed in the far field seem rather produced by expansion of the vapour and not by the vapourisation of the liquid, which is said to be a too slow process for generating a strong blast. In (10) it is mentioned however that the rapid vapourisation process can produce significant dynamic pressure effects in a near field. These effects are of particular importance in case of a BLEVE in a confined space such as a tunnel. Their demonstration does not involve superheat limit theory but uses a thermodynamic estimate of the available energy. Such estimates can assume isentropic expansion (62) or, more realistic, adiabatic irreversible expansion (60).The second estimate is about half of the first (2).

At the relatively small scale of 1 mm diameter droplets, the rise in pressure in the surroundings of the exploding droplet has been measured, but this seems to be a too small scale to generate a shock wave[1] while at the large scale (explosion of a partially filled 2000 $liter$ vessel) blast waves have been measured, but it is debated whether those blast waves are generated by a rapid vapourisation process or by expansion of vapour already present in the vessel before rupture.

The question arises whether there is an intermediate scale where the vapourisation dynamics and the pressure wave in the far field both have been measured. So far, we have not found reports on such experiments in the literature. Here we divide the treatment of BLEVE experiments in two parts: the studies on phenomena inside a vessel subject to rapid depressurisation (pre-BLEVE phenomena) and the studies on blast effects of a completely rupture vessel (BLEVE phenomena).

In the first class of experiments vapourisation and pressure were measured inside a vessel in experiments on of volume 100 ml up to a few liters, where the (partial) vessel rupture is simulated by a controlled opening of a valve or by bursting a foil diaphragm. In those experiments the emphasis is on the question how low the pressure can drop before the pressure starts to rise again because of bubble formation (re-pressurisation).

In the second class of experiments pressure waves are measured in a region at

[1] It is noted that when a spherical shock is generated, it can decay during its propagation (48)(85).

some distance of the ruptured container or vessel. Usually also temperature and/or pressure is measured inside the vessel in the time interval before rupture.

2.2.1 De-pressurisation / re-pressurisation

Experiments

Kim-E and Reid experiments In (42) simple experiments are described using both saturated liquid and supercritical carbon dioxide where depressurisation of a $7\,liter$ tank with $1.5\,in.$ diameter burst disc did not lead to an explosion. The reason for these failures is discussed. In this article also some reported industrial accidents are described and analyzed as to whether they did result from the system reaching the superheat limit state. Kim et al. (41) give further comments on the experiments of Kim-E and Reid. Reasons for disagreement between theory and experiments may include factors like growth of vapour bubbles on the wall of the vessel (heterogeneous vapourisation) which prevents adequate pressure-drop to trigger homogeneous nucleation within the bulk liquid.

McDevitt et al. experiments Experiments on BLEVE of refrigerants R-12 and R-22 were reported in (50). They report two types of experiments: in the first, a $1\,liter$ commercially available tank was ruptured with a rifle bullet. In the second, the explosion occurred in a shock tube. High speed photographs during the explosion of the $1\,liter$ tank indicate that the event takes less than $2\,ms$. They conclude that due to the short time frame, along with the fact that pressure travels in waves, points to a shock related event. The experiments in the shock tube were made to obtain direct evidence of the existence of shock waves, and to attempt to measure their destructive capability. But the shock waves referred to are rarefaction waves traveling in the liquid, not blast waves in the surrounding air. They report that the boiling of liquid of the fluid around the hole is homogeneous (as seen in photograph) and report the recorded pressure wave in the liquid.

Frost et al. experiments The rapid boiling that occurs when a pressure-liquefied gas is suddenly vented to the atmosphere was investigated in much more detail at somewhat smaller scale in (30). As a testing fluid they used refrigerant R-22, because it exhibits similar thermodynamic properties to propane, and yet is not flammable. Vessels of different shape and material were used (rectangular steel

vessel pressure, cylindrical glass vessel, spherical glass test vessel). A parametric study was carried out to examine the influence of vent area, liquid fill volume and initial liquid pressure (and corresponding saturation temperature) on the boiling dynamics in the 260 ml steel vessel containing R-22. For each case the evolution of pressure versus time is studied. After opening of the vessel the pressure first drops and then after start of vapourisation starts to rise again.

The goal of the experiments of Frost et al., was to determine the conditions that can lead to the maximum repressurisation within a vessel, considered to be the worst case scenario from the point of view of risk for catastrophic rupture of the vessel. In all cases heterogeneous nucleation and bubble growth at the vessel walls is found to play an important role. Of interest for us here are results reported on whether or not the superheat limit is attained. An intriguing Figure in this respect is the following figure, reproduced from (30).

The discussion of Fig.(2.3), given by Frost et al. (30) is as the following: "The figure shows the saturation and spinodal curves [2] for R-22 which bound the metastable region. Path 1-2 corresponds to an isentropic expansion from a pressure of 2.06 MPa (and a saturation temperature of 53 $°C$) to atmospheric pressure which yields the greatest possible degree of superheat at atmospheric pressure. The state of the liquid following depressurisation for both the 65% and 90% liquid fill volume trials are also shown. Although no homogeneous boiling was observed, the locus of the data points indicates that there is a limit of superheat attained that is determined by heterogeneous boiling. Even though the degree of superheat attained will depend on the geometry of the vessel as well as the surface properties of the vessel walls, it is interesting to note that the maximum degree of superheat is attained at a liquid temperature that is similar to that predicted by homogeneous nucleation theory."

In (30) a series of photographs is shown with a close-up of the test section during the depressurisation of R-22 from initial pressures of 1.03 MPa and 1.43 MPa, showing heterogeneous boiling from the walls of the steel vessel. Photographs of the cases with still higher pressure and coming closer to the spinodal curve however are not shown.

It is hard to believe that in this experiment the spinodal or more precisely, the kinetic superheat limit, has really been reached, because then a homogeneous nucleation would have occurred with possibly catastrophic consequences. The

[2] Note that the spinodal curve is used as the reference threshold of rapid boiling.

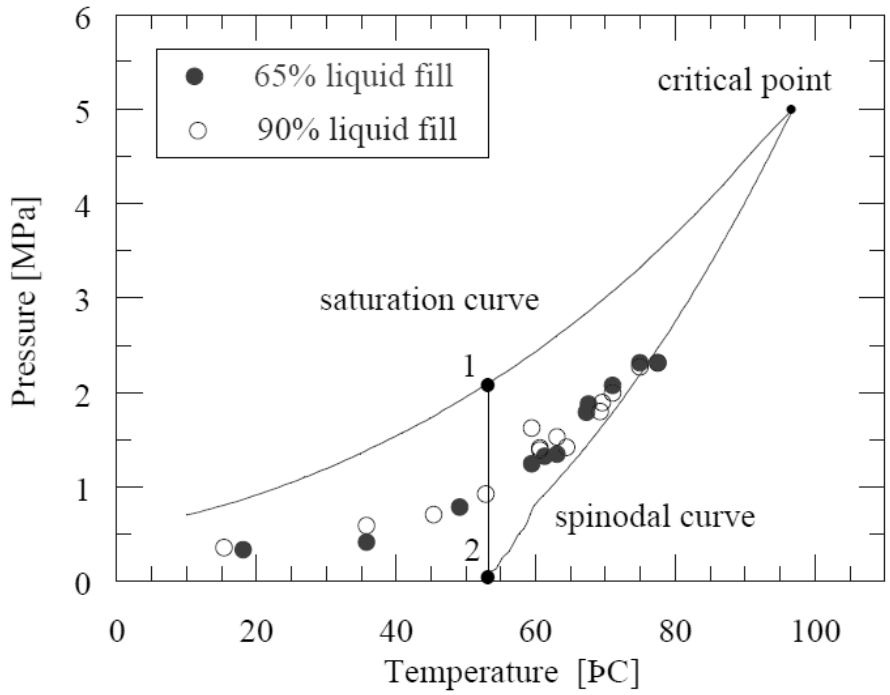

Figure 2.3: Locus of thermodynamic end states following pressure drop showing the degree of superheat attained attained for the steel vessel. Reproduced from Frost et al. 1995.

crossing of the spinodal seen in Fig.(2.3) may be due to a measurement error or due to a error in the value of the spinodal. It is not reported how the spinodal curve of R-22 was obtained.

Nevertheless the experiments shows that :

- Occurrence of heterogeneous nucleation can prevent a liquid from homogeneous nucleation by depressurisation.
- The higher the superheating the smaller the distance in pressure between saturation curve and superheat limit curve and the easier it is to come close to the latter by rapid depressurisation.

- For experiments with R-22, with similar properties as propane, it seems possible to reach the kinetic superheat limit using steel vessel with volume 260 ml if heterogeneous nucleation is well suppressed.

Chen et al. experiments Chen et al. (15, 16) have also reported experiments on rapid depressurisation and consequences for vessel pressure. These experiments are done with water as testing fluid and well below the superheat limit temperature.

Modeling

In the literature correlations have been developed to model the minimal pressure reached after sudden opening of a high pressure vessel, and also the pressure recovery. It is clear that when the role played by heterogeneous nucleation is essential, it seems difficult to handle since it depends on a variety of circumstances, e.g. properties of the walls and purity of the fluid.

Frost et al. (30) refer to (5), who have developed a semi-empirical model to predict the pressure undershoot. Their model is based on the assumption that if the rate of depressurisation is large enough and the size of any physical heterogeneity present is small enough, then nucleation is initiated stochastically and is governed by the nucleation theory. To account for nucleation at the wall, they introduce a heterogeneous correction factor (which is determined by fitting to experimental data) to the Gibbs number, which is a measure of the potential barrier to nucleation. Application of that correlation to the experimental data of (30) is described in (9). Another potentially relevant article proposing a model for the heterogeneous nucleation factor is (25).

2.2.2 BLEVE blast effects

Experiments

Blast effects of a BLEVE have been measured in field experiments where a vessel containing a pressurized gas was made to explode by external heating or by fire. The disadvantage of such experiments is that the vessel rupture does not occur in a well-defined way and that little or no information is available on the physical pro-

cesses inside the vessel before and during rupture. In the best case measurements of pressure and temperature in the vessel or made until the moment of rupture.

Giesbrecht et al. experiments A series of bursting propylene vessel experiments have been reported in (33). They studied the effects of fast vapourisation, cloud spreading and chemical explosion. In relation to the first effect, they found that when propylene, preheated up to approximately $70°C$, is expanded from about $60\,bar$ to atmospheric pressure, flash evaporation already produces a blast wave with considerable peak pressure in the vicinity of the vessel. It was possible to establish a relationship between the peak pressure and distance, valid for vessels of different sizes and initial temperatures. The amounts of propylene considered ranged from $0.125\,kg$ to $452\,kg$ (corresponding to vessel volumes from $226\,cm^3$ to $10^6\,cm^3$). They point out that the vapour pressure at $80°C$ is only $37\,bar$. Therefore these experiments concern a case where the initial state is not a liquid/vapour mixture in phase equilibrium, but rather a pressured subcooled liquid. The amount of energy released in the whole process is possibly larger than in the case of liquid at saturation temperature because higher initial PLG pressure can result in faster disintegration of the vessel and larger pressure drop before the re-pressurisation, which may have contributed to the strength of the blast effect.

Johnson and Pritchard experiments The paper (37) presents the results from five large-scale BLEVE experiments in which the released gas was ignited. Fuel was butane or propane. Release pressure was 7.5 or 15 bar, vessel capacity either 5.659 m^3 or 10.796 m^3 with filling ratio's from 39% to 80%. The pressure of the blast wave was recorded. Vessel pressurisation was achieved by heating the liquid within the vessel with electric immersion heaters. The temperature and the pressure in the liquid were monitored. They say that "The maximum overpressure measured following vessel failure was substantially lower than values predicted by existing methods for the overpressure generated by the rapid flashing of the released liquid in a BLEVE. This may be due to the liquid temperature at the time of the release being below that required to achieve homogeneous nucleation of the liquid."

Gelfand et al. experiments Blast effects in a very small scale BLEVE experiment have been measured by Gelfand et al. (32) at the Institute for Chemical Physics in Moscow. They report on experiments in a shock tube, $3\,m$ long and $50\,mm$ in

diameter. Initially, the shock tube has a low pressure chamber (LPC) filled with air at normal conditions and a high pressure volume containing an electric heating element and a small aluminum container immersed into hot water. The container is partially filled with the 'liquid under investigation' (LI) and is covered with a rupture disk. During the heating process the pressure and the temperature of the contents of the high pressure volume rise in agreement with the LI saturation curve. When the pressure reaches a chosen value p4 the diaphragm bursts and the liquid becomes superheated relative to the LPC conditions. Outflow of liquid and vapour leads to shock wave formation. In the experiments the pressure of diaphragm rupture, the high pressure volume (HPV), the mass and the properties of the liquid were varied. The investigated liquids are water Freon-113 and ethanol. The volume ranges from 26 to 76 cm^3. The mass varies from 5 g to 22 g. The rupture pressure varies from 0.5 MPa to 3.1 MPa. The parameters of the shock are measured by piezo-electric pressure gauges.

The shock tube is positioned vertically. When the LPC is at the top the vapour containing part of the container is closest to the diaphragm. When the LPC is at the bottom, the liquid containing part of the container is closest to the diaphragm. In this way the experiments can represent both a rupture of the vapour space and the liquid space of a vessel.

Interesting conclusions of this work are:

- In case of vapour space closest to the rupture disk, the pressure profile consists of a leading shock of a triangular shape and a pressure wave without shock front. The leading shock is attributed to the expansion of the saturated vapour. Subsequently the expansion of the vapour-liquid cloud leads to a slow increase of pressure.
- In case of liquid closest to the rupture disk, the expansion of the superheated liquid causes the formation of a pressure wave without sharp shock front.
- With an increase of the liquid mass, the duration (impulse) of the total shock wave rises significantly, while the amplitude of the shock wave remains constant.
- The contribution of a mass addition process from evaporated liquid in the shock wave impulse formation become dominant with low values of the liquid mass m. With initial liquid volume fraction about 50%, the shock wave impulse exceeds the value of the case with vapour only by $7-10$ times. The

peak value of the pressure however is practically independent of the mass of liquid.

- The peak value of pressure and the shock wave impulse increase with pressure ratio between high pressure and low pressure chamber.
- A liquid with lower molecular weight gives a long shock wave duration.

A qualitative description the transient boiling liquid expansion process is proposed and a simple predictive model for the strength of the shock waves is formulated.

Stawczyk experiments The paper (83) describes experiments with explosions of small LPG tanks. The tests enabled a determination of temperature and pressure at which tanks containing LPG disrupt. The experiments were carried out in standard cylindrical tanks of capacity $5\,kg$ and $11\,kg$ filled with propane or propane-butane mixture. For the needs of the experiment, the tank was modified. Instead of a shutting valve, a specially designed head was mounted. It allows sensors to be inserted in the tank. The bottom of the tank was heated from the outside using standard gas burners. The disruption of the tank was found to take place at temperature and pressure above the critical point. In that region of thermodynamic state space the distinction between liquid and vapour can not longer be made. When such system is depressurised it is expected to reach states beyond the superheat limit. Blast wave pressure was reported at the distance $10\,m$ from the tank in open area and at the distance $2\,m$ from the tank in closed area. Since the explosion of the vessel occurred in an uncontrolled way and the pressure measurements are rather crude, the value of this experiment for model validation is limited.

Birk et al. experiments Birk et al. (10) present an analysis of the blast overpressures created by nearly 20 catastrophic failures and BLEVE's of propane tanks, reported in earlier publications by Birk et al. They claim that the results suggest that the liquid energy content did not contribute to the shock overpressures in the near or far field. "The liquid flashing and expansion does produce a local overpressure by dynamic pressure effects but it does not appear to produce a shock wave. The shock overpressures could be estimated from the vapour energy alone for all the tests considered. This was true for liquid temperatures at failure that were below, at and above the atmospheric superheat limit for propane." The possible explan-

ation of this observation is that in the considered cases the vessels were only partially filled with liquid.

Birk et al. (10) point out that the expansion of the flashing liquid contributes to other hazards such as projectiles, and close in dynamic pressure effects and conclude "Of course BLEVE releases in enclosed spaces such as tunnels or buildings have different hazards."

Birk et al. (10) also make the remark that the occurrence of a double pressure peak should not be interpreted as a proof of a liquid vapourisation generated second blast wave (after the first one generated by the expansion of the vapour space), but is a well-known effect in explosions by gas expansion.

Because the rupture of the vessel in the reported experiments did not occur in a controlled way the value of the experiments for model validation are limited.

Van der Voort et al. (TNO) experiments In (95) and (96) results are described of the BLEVE of a bottle filled with liquid CO_2. The cylindrical bottles have a volume of $40\,liter$ and are filled with $30\,kg$ liquid CO_2 at a pressure of $57\,bar$, the saturation pressure at $290\,K$.

The rupture of the bottle is caused by an explosive charge. The pressure has been measured at four locations, at distances of 2, 3, or $4\,m$ from the bottle. The measured signals show a clear peak caused by the explosive charge, and also positive and negative phases of a blast wave caused by the explosion of the liquid.

Since the homogeneous nucleation temperature or the kinetic superheat limit temperature of CO_2 is about $271\,K$ at pressure of $35\,bar$, a depressurisation at $290\,K$ from $57\,bar$ to $1\,bar$ is expected to bring the liquid at the homogeneous nucleation temperature. Heterogeneous nucleation is not expected to play a large role since the bottle is completely opened and the liquid is not longer confined by walls. For these reasons this experiment is highly interesting for model validation.

Bjerketvedt et al. experiments Recently another set of experiments on small scale CO_2-BLEVE was reported (11). The cylindrical vessels containing CO_2 are $60\,mm$ or $100\,mm$ in length and the outer diameter is $40\,mm$. Solid CO_2 is first put in the vessel and after heating and pressurisation, CO_2 reaches the saturation state at the pressure of 30 to $45\,bar$. The pressure in the vessel keeps increasing until it ruptures. One pressure transducer inside the vessel records the CO_2 pres-

sure while three other pressure transducers located 1, 1.5 and 2 m from the vessel respectively record the blast wave. A high speed video camera with a frame rate of 10000 frames/sec is used to record the rupture of the vessel, the projection of fragments and the formation of CO_2 cloud around the ruptured vessel.

Bjerketvedt et al. compare the measured shock waves with the modeled shock waves generated by the expansion of the compressed vapour CO_2 only (without the boiling of the liquid CO_2) and find the agreement is quite well. Therefore they conclude that "the shock front is governed by the expansion of the gas phase (vapour) in the vessel prior to explosion" in their experiments. However, they also admit that this observation can not rule out the importance of the liquid vapourisation on the blast effect in large scale or "boiling also will contribute to shock strength".

In their final conclusions, Bjerketvedt et al. point out the importance of understanding the boiling mechanisms, validating the EOS models and developing CFD codes for risk analysis.

Modeling

Given the complexity of the explosive vapourisation process and the vessel rupture, it is a difficult task to predict the blast effect. Traditionally the blast strength is obtained from an energy estimate (2, 14). A loss factor representing how much of the energy is used for acceleration of projectiles rather than creation of blast wave can be taken into account. Such estimates represent idealized situations, with spherical symmetry, or hemi-spherical symmetry.

To be more general and flexible, the blast wave has to be calculated using CFD. In order to make a more accurate calculation, the strength of the volume source term generating the blast wave has to be known. And for this, the rate of vapourisation and the nature of the release of material from the broken vessel has to be determined (vapour and liquid fragments, eventually also solid fragments).

Van der Voort et al. (TNO) model Van der Voort et al. (TNO) model is based on the assumption that the explosive vapourisation process is as fast as the inertia of the expanding mix of vapour and liquid in the surrounding air allows. The overpressure from a BLEVE is numerically computed using a single phase model by

imposing the vapour pressure of a flashing liquid as the boundary condition. This was done without any modeling of the flashing process.

Here single phase does not imply that complete vapourisation is assumed. The fact that the vapourisation in general is incomplete (see above) can be taken into account in the form of an effective density of the liquid/vapour mixture represented as a single phase.

This method gives a conservative estimate of the overpressure (91, 92, 93) in the sense that in reality the rate of vapourisation could be smaller than assumed in this model, leading to a weaker blast.

Van den Berg et al. (92, 93) have applied the expansion controlled evaporation model to the experiments of Giesbrecht et al. (33). The expansion controlled evaporation model has also been applied to the TNO experiments (95) reported above and the results are presented in (96).

In addition to Van der Voort et al. (TNO) model for predicting the overpressure, Al-Khoury et al. from TNO has also developed a time integration scheme to evaluate the blast loading caused by a BLEVE on the porous media (64).

Pinhasi et al. model Pinhasi et al. (57, 59) developed a model which is capable of describing both the volume generation in the vapourising liquid and the blast effect in the surrounding air. A schematic diagram of the process is shown in Fig.(2.4). Their research work has special meanings to us because our work is developed based on their model, therefore we would like to elaborate more on it here.

For the reason of simplification, they assume the computational domain to be one-dimensional and separate it into two regions, the PLG region and the air region. The single-phase air region is described by a set of single-phase conservative equations similar to van der Voort et al. (TNO) model while the region occupied by the PLG (two-phase mixture) is described by a set of two-phase conservative equations. The single-phase equations and the two-phase equations are coupled at the contact face between the PLG region and the air region where continuities in pressure and velocity must hold. Those conservative equations will be introduced in Chpt.(4).

Pinhasi et al. use the particle-path algorithm of the method of characteristics to solve the conservative equations and get the properties of the PLG and the air. The

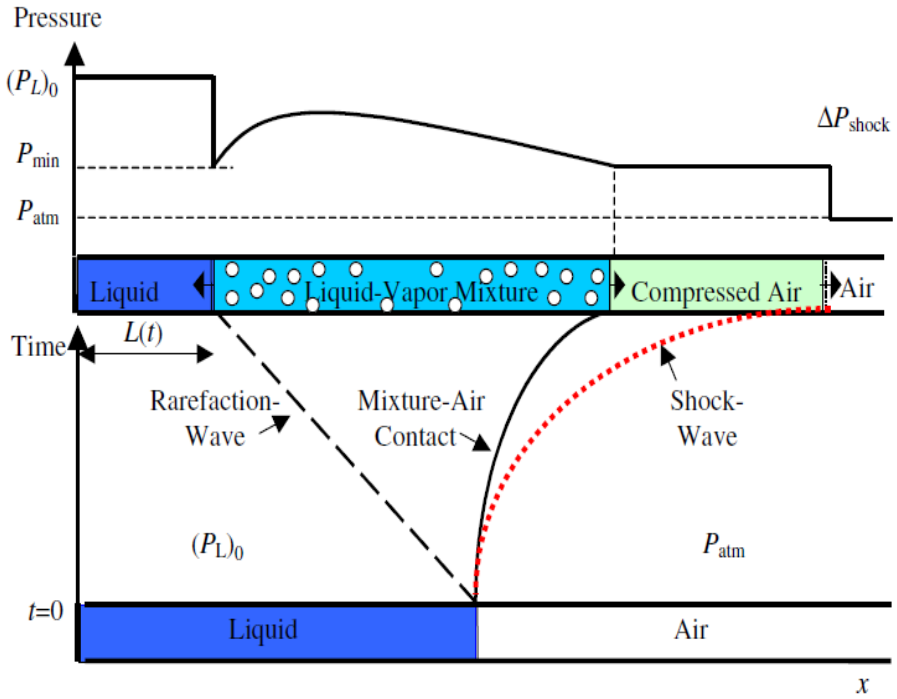

Figure 2.4: Typical wave action in the x-t plane and the pressure profile following BLEVE. Reproduced from Pinhasi et al. 2007.

particle-path algorithm of the method of characteristics will be discussed and verified in Chpt.(5).

The EOS is not specified in Pinhasi et al. model and we will talk about our choice of the EOS in Chpt.(3).

Back to the volume generation of the vapourising PLG, this phenomenon is due to the vapour generation in the PLG liquid which consists of two parts, the generation and development of the liquid-vapour interface (hereinafter called the interface) and the heat/mass fluxes of the PLG via the interface. In Pinhasi et al. model, those two parts have been considered separately: i) Pinhasi et al. take the flow regime into consideration in developing their interfacial area density (interfacial area per unit volume) model. Distinctions have been made between the

bubbly flow, churn-flow and droplet flow when the dependence of the interfacial area density on the vapour volume fraction is considered. ii) for the interfacial heat/mass flux (the interfacial heat/mass transfer per square meter of the interface per second) models, the vapourisation of the PLG is generally assumed to be thermal-controlled while for highly superheat conditions, the interfacial heat/mass fluxes are derived from the kinetic theory.

Therefore the advantage of Pinhasi et al. model is the introduction of the two-phase model which allows the vapourisation of the PLG to gradually occur from the surface of the bulk liquid to the interior, accompanied by the depressurisation process of the involved PLG. As one remarkable feature, Pinhasi et al. model does not consist of the bubble nucleation model and the PLG is initially two-phase mixture containing a very small amount of vapour (e.g. the volume fraction of 10^{-6}). This simplification puts limitations on Pinhasi et al. model and also leaves spaces for us to improve it.

As the result of their computation, Pinhasi et al. report that the predictions of the model are in agreement with the calculation of blast effects using an energy estimate assuming adiabatic and irreversible expansion. But the model has not been directly validated with experiments.

2.3 Research from related fields

Vapourisation is a widely used process, occurring in controlled conditions in boilers, heat exchangers, steam generators, refrigerators, etc. Extremely rapid vapourisation has also attracted a lot of attention in the nuclear industry in relation to so-called 'loss of coolant accidents' (LOCA). Therefore it is of potentially very interesting to look at experiments in those related fields, other than containment of liquefied gases.

2.3.1 Flash evaporation

On a small scale and for conditions of relatively small superheat experiments have been done with flashing of a liquid layer. See (56) and (75, 76). The relatively low superheat and the film shape of the liquid in those experiments result in vapourisation occurring on the liquid surface rather than in the bulk liquid and the process is less violent that that no shock will be generated in the ambient air.

2.3.2 Steam explosions / rapid phase transitions

Explosions arising from the contact of molten metal and water can occur in a number of metallurgical processes. Explosions caused by LNG (Liquefied Natural Gas) contacting sea water are also possible. In either case, the contact face between two layers acts as the site of heterogeneous bubble nucleation and heat is also supplied from below layer to the upper one via the contact face. Two essential parts of rapid phase transition, the nuclei and the heat, are ready at the contact face, therefore shock waves are possible in those scenarios.

Experiments

Cleaver et al. (18) provide a summary of the experimental information that Advantica Ltd. has collected on LNG behavior over the course of the last 30 years. This includes experimental data on rapid phase transitions obtained in a collaborative project with Gaz de France and Statoil. During the collaborative projects, liquid nitrogen was jetted into water to mimic a spill of LNG. And also experiments with LNG released from a pressurized container vertically downwards to impact on the water surface were made. It was shown that the RPT tended to occur in the spreading pool rather than in within the jet-mixing region. The severity of the RPT was found to be variable.

Modeling

In (77), some aspects of the steam explosions are considered. They draw attention to the importance of the superheat limit and to the fact that only a part of the explosive energy enters a shock wave. They give references to other articles analyzing real explosions from molten materials and water from energetic point of view.

In the review (18) also modeling issues of rapid phase transitions are discussed.

2.3.3 Medium scale blow down tests

The rapid depressurisation of hot saturated water in a pipe has been studied extensively due to its relevance for nuclear reactor safety. It is known as 'Standard

problem number 1'.

At ambient pressure, the superheat limit temperature for water is 553.2 K, approximately 280°C. This limit most often is not reached in blowdown experiments. And blast wave effects apparently have not been reported in the literature on blowdown experiments.

Nevertheless, among the list of BLEVE events compiled in (2) is a case of steam pipe depressurisation in a nuclear reactor in Mihama, Japan.

Experiments

Experimental results are described in (4, 63, 99). The experiments of Edwards and O'Brien (63) consisted essentially of heating a water-filled pipe to the required temperature with the pressure maintained above saturation conditions, then adjusting the required pressure before rupture a glass disc at the end of the pipe and recording the transient pressure, temperature and density changes at several locations along the pipe during the blowdown phase. To density measurement using X-ray tomography provides information on the void fraction.

Alamgir et al. (4) refer to experiments at temperatures above the superheat limit. However, these experiments are at the smallest pipe diameter, with probably the largest effects of heterogeneous nucleation.

Modeling

Although the experimental results are already quite old, they remain a standard database for model testing.

The numerical solution method (method of characteristics) we are using for the model presented in this thesis has been first applied to the blow down problem by Ferch (28).

More recent modeling results are described in (17, 36, 53, 86, 90).

The fact that the experiments have been simulated with different models makes them an interesting addition to a database for BLEVE model validation. It allows to compare the performance of a new model for the vapourisation during rapid

depressurisation not only with experiment but also with predictions of other models.

CHAPTER 3

EQUATION OF STATE

A first ingredient needed in a model for a BLEVE is a thermodynamic equation of state (EOS). The main function of an EOS is to give the relation between the state variables like pressure, temperature and specific volume in states of thermodynamic equilibrium. In the context of BLEVE, it is necessary to use an EOS adequate for describing the two-phase mixture of a liquid and its vapour. And moreover the EOS should also be adequate to describe the relation between state variables in a metastable state, out of equilibrium. Using the properties of the metastable state and using information from the vapourisation model, the EOS will, for example, predict the change in pressure due to changes in temperature and density of the mixture. Clearly this is an important part of a model to predict blast wave generation.

In this chapter we discuss the selection of an EOS, the calculation of the properties in the metastable states from the EOS and the validation of the selected EOS for prediction of the superheat limit.

3.1 Equations of state

In equilibrium thermodynamics, the state of matter is described by state variables, such as temperature, pressure and specific volume. Different states correspond to

different values of state variables. An equation describing the relation between state variables in a wide range of states is called equation of state. Equations of state have been widely used in describing the properties of pure fluids, mixture of fluids and solids.

The research on equation of state started on gases. Based on Boyle's law in 1662 and Charles's law in 1787, the ideal gas law was first derived by Émile Clapeyron in 1834 and further developed to be

$$p\,v_M = \mathbb{R}\,T \tag{3.1}$$

where v_M is the molar volume and $\mathbb{R}$ is the universal gas constant. The ideal gas law ignores the molecular interactions in regarding the molecules as material points with zero volume (equivalent to ignoring the molecular repulsion) and neglecting the attracting force of the molecules. Those simplifications are acceptable for gaseous states because the specific volume is relatively large, therefore the interactions between molecules are negligible.

In liquid states the molecular attraction and repulsion are not negligible and in order to describe liquid states, the EOS has to be different from the ideal gas law. This work was initiated by Johannes Diderik van der Waals in 1873 and he proposed the equation, now called the van der Waals equation of state (vdW-EOS), as

$$\begin{aligned} \left(p + \frac{\mathfrak{a}}{v_M^2}\right)(v_M - \mathfrak{b}) &= \mathbb{R}\,T \\ \mathfrak{a} &= \frac{27\mathbb{R}^2 T_c^2}{64 p_c} \\ \mathfrak{b} &= \frac{\mathbb{R}\,T_c}{8 p_c} \end{aligned} \tag{3.2}$$

in which $\mathfrak{a}$ and $\mathfrak{b}$ are substance-specific constants and the term $\mathfrak{a}/v_M^2$ is the correction on the pressure considering the molecular attraction and the term $\mathfrak{b}$ is the correction on the specific volume considering the molecular repulsion. T_c and p_c respectively are the critical temperature and critical pressure of the material.

The vdW-EOS can be written as a third order polynomial equation for the specific volume and therefore is called a cubic equation of state. The vdW-EOS is of historical importance but not sufficiently accurate for many substances. Keeping the

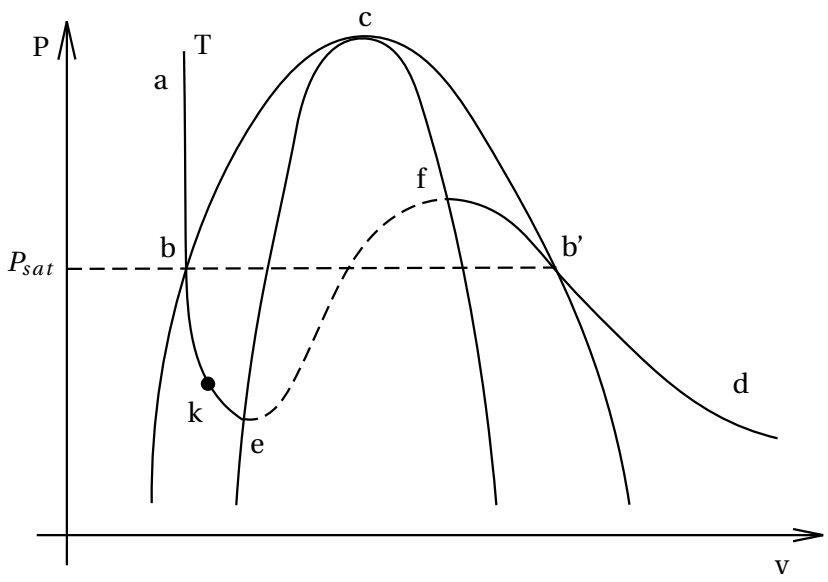

Figure 3.1: $p-v$ diagram for a cubic EOS. Saturation curve (bcb'), isotherm at equilibrium ($abb'd$), liquid spinodal (ce) and vapour spinodal (cf).

form of a cubic equation of state, other researchers either made direct modifications on it or introduced more constants to characterize the molecular forces and proposed equations of state with higher accuracy. Those equations are normally capable of describing $p-v-T$ relations for both gaseous and liquid states of a substance. Figure 3.1 shows the characteristic features of the $p-v$ diagram given by a cubic EOS: the isotherm ($abefb'd$), the isotherm at equilibrium ($abb'd$), the saturation curve (bcb'), the liquid spinodal (ce), the vapour spinodal (cf). As introduced in Chpt.(1), the thermodynamic superheat limit (e) is at the intersection of metastable branch of the isotherm and the liquid spinodal. The kinetic superheat limit (k) is expected close to but away from the thermodynamic superheat limit.

Widely used cubic equations of state are the Redlich-Kwong equation of state (RK-EOS) (65) as in Eqn.(3.3)

$$
\begin{aligned}
p &= \frac{\mathbb{R}T}{v_M - \mathfrak{b}} - \frac{\mathfrak{a}/T^{0.5}}{v_M(v_M+\mathfrak{b})} \\
\mathfrak{a} &= \frac{0.42748\mathbb{R}^2 T_c^2}{p_c} \\
\mathfrak{b} &= \frac{0.08662\mathbb{R}T_c}{p_c}
\end{aligned}
\tag{3.3}
$$

and the Peng-Robinson equation of state (PR-EOS) (55) as in Eqn.(3.4)

$$
\begin{aligned}
p &= \frac{\mathbb{R}T}{v_M - \mathfrak{b}} - \frac{af}{v_M^2 + 2bv_M - \mathfrak{b}^2} \\
\mathfrak{a} &= \frac{0.457235\mathbb{R}^2 T_c^2}{p_c} \\
\mathfrak{b} &= \frac{0.077796\mathbb{R}T_c}{p_c} \\
\mathfrak{f} &= \left[1 + \kappa\left(1 - T_r^{0.5}\right)\right]^2 \\
\kappa &= 0.37464 + 1.54226\omega - 0.26992\omega^2
\end{aligned}
\tag{3.4}
$$

where $T_r = T/T_c$ is the reduced temperature; ω is the acentric factor, a characteristic parameter, different for every substance; κ is the polynomial fit of the acentric factor ω; $\mathfrak{f}$ is an intermediate factor.

The RK-EOS and the PR-EOS have been further developed (81) (84) (88) (89) ever since they are proposed. In this work we shall use the modified Peng-Robinson equation of state proposed by Stryjek and Vera, called the Peng-Robinson-Stryjek-Vera equation of state (PRSV-EOS) (84). It has the following form:

$$
\begin{aligned}
p &= \frac{\mathbb{R}T}{v_M - \mathfrak{b}} - \frac{af}{v_M^2 + 2bv_M - \mathfrak{b}^2} \\
\mathfrak{a} &= \frac{0.457235\mathbb{R}^2 T_c^2}{p_c} \\
\mathfrak{b} &= \frac{0.077796\mathbb{R}T_c}{p_c} \\
\mathfrak{f} &= \left[1 + \kappa\left(1 - T_r^{0.5}\right)\right]^2 \\
\kappa &= \kappa_0 + \kappa_1\left(1 - T_r^{0.5}\right)\left(0.7 - T_r\right) \\
\kappa_0 &= 0.378893 + 1.4897153\omega - 0.17131848\omega^2 + 0.0196554\omega^3
\end{aligned}
\tag{3.5}
$$

where κ_0 is the polynomial fit of the acentric factor ω; κ_1, an adjustable pure component parameter, is introduced to prompt the accuracy of the model. In (84), the substance-specific constants of T_c, p_c, ω and κ_1 can be found for over ninety industrial compounds.

The reason for choosing the PRSV-EOS in the current research is very practical: it is quite generally applicable and available in a thermodynamic software package named FluidProp developed by Colonna and co-workers (19), that can easily be coupled to flow simulations. The package FluidProp has five sub-programs, namely IF97, TPSI, GasMix, RefProp and StanMix, for different purpose of calculations, e.g. IF97 is for the calculation of water and steam; GasMix is for ideal gases and mixtures of ideal gasses. StanMix allows to calculate the properties of more than sixty industrial fluids and mixtures using PRSV-EOS. However, before it could be applied in BLEVE simulation, an extension of StanMix is needed as described next.

3.2 Extension of StanMix for metastable states

StanMix as available from its creators (19) is meant to be used as an equilibrium thermodynamic code. It gives as output the properties of the equilibrium state, either of a single phase or of a two-phase mixture. In the vapour-liquid-equilibrium

(VLE) region (the region under bcb' in Fig.(3.1)) the output consists of the properties of the equilibrium vapour-liquid mixture, which are mass-fraction-weighted averaged values of the corresponding properties of the saturated liquid at point b and the saturated vapour at point b'. In our BLEVE simulation, the equation of state must be capable of predicting the properties of the metastable states i.e. the superheated liquid and the supercooled vapour. The calculation for the single-phase properties must be extended into the VLE region. Therefore StanMix needs modifications.

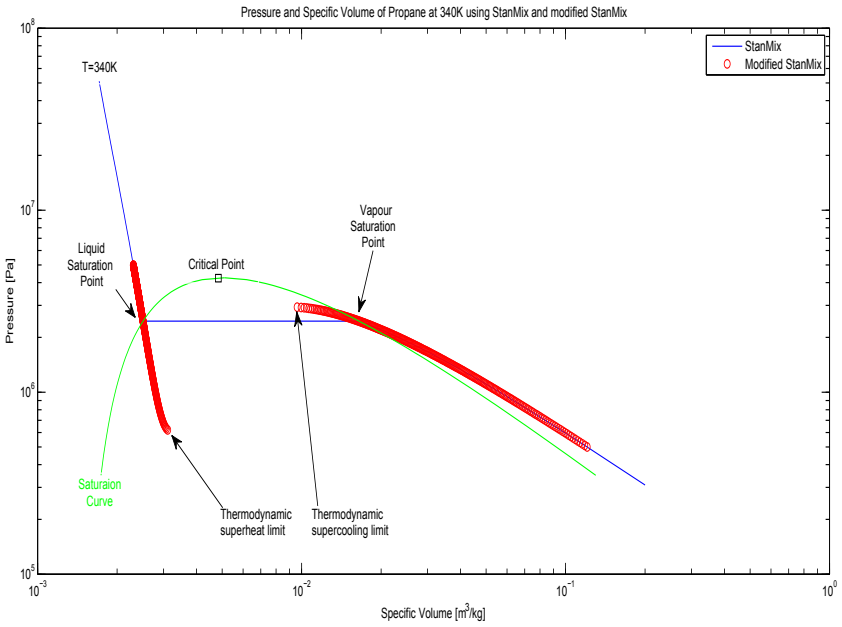

Figure 3.2: Illustration of the extension of StanMix to calculate the metastable states. Blue line is the isotherm at 340 K of equilibrium states. Green curve is the saturation curve. Red symbols are the isotherm including metastable states of either liquid or vapour. The metastable branches of the liquid and vapour isotherm respectively end in the thermodynamic superheat limit and the thermodynamic supercooling limit.

We use the $p-v$ diagram of propane at 340K to demonstrate this problem. In Fig.(3.2), the blue line is the locus of the $p-v$ outputs from StanMix showing that under the saturation curve (the green line), the specific volume of liquid-vapour

mixture is gradually increasing from the saturated liquid specific volume to the saturated vapour specific volume. The red circles are the outputs from the modified StanMix. It can be observed that above the saturation curve, the outputs from the modified StanMix match the ones from StanMix. However, under the saturation curve, the liquid specific volume can be computed down to the liquid thermodynamic superheat limit pressure as well as the vapour specific volume up to the vapour thermodynamic supercooling limit pressure predicted by PRSV-EOS for a given temperature. Therefore, the properties of the metastable states can be computed using PRSV-EOS in the modified StanMix.

3.3 Quality test of PRSV for the superheat limit prediction

In the previous chapter distinction has been made between the thermodynamic superheat limit (TSL) and the kinetic superheat limit (KSL). The value of the TSL follows from a chosen thermodynamic equation of state whereas the KSL is in the first place determined experimentally. The difference between the KSL and the TSL is also indicated in Fig. 3.1.

In (1), Abbasi et al. compared the TSL predicted by seven cubic EOS with the measured KSL at the atmospheric pressure in a way to evaluate the qualities of those EOS in predicting metastable states. They conclude that for ten alkanes they computed, the RK-EOS gives the minimum average absolute deviation of 1.64% from the experimental value; The Twu-Redlich-Kwong equation of state (TRK-EOS), a modified RK-EOS, gives 2.02%; The PR-EOS and its modified version, the Peng-Robinson-Mathias-Copeman equation of state (PRMC-EOS) give the deviations of 3.46% and 3.49% respectively; The Berthelot equation of state (Berthelot-EOS) gives 3.74%; The vdW-EOS gives 4.47% and the Soave-Redlich-Kwong equation of state (SRK-EOS) gives 5.02%.

We here carry out the same comparison for the PRSV-EOS simply to show the quality of the PRSV-EOS compared with the other seven EOS. The work has been reported previously in a BSc thesis by R. Glas (34) prepared under supervision of the author of this thesis. For this comparison only the TSL has to be calculated, rather than the full metastable branch of the isotherm. The results in Table (3.1) and Table (3.2) indicate that for the same ten alkanes used in (1), the average absolute deviation is 3.50% which is comparable to the PR-EOS and the PRMC-EOS.

Table 3.1: Superheat limit temperatures (SLT) at 1 atm pressure of ten alkanes calculated using three equations of state, data obtained from (34).

Alkanes	Experimental SLT (K)	SLT predicted at 1 atm pressure (K)		
		vdW-EOS	RK-EOS	PRSV-EOS
Butane	378.00	360.40	381.60	388.70
Decane	558.10	525.30	555.40	575.10
Ethane	269.00	258.60	273.90	276.80
Heptane	487.00	458.70	485.30	499.00
Hexane	457.00	430.70	455.80	463.00
Methane	165.00	161.80	171.20	171.70
Nonane	538.30	504.50	533.60	551.50
Octane	512.80	483.20	511.20	527.00
Pentane	420.80	421.30	445.90	455.90
Propane	353.00	312.80	331.20	336.10

Table 3.2: Deviation of the predicted superheat limit temperature (SLT) using three equations of state for ten alkanes

Alkanes	Deviation from experimental values (%)		
	vdW-EOS	RK-EOS	PRSV-EOS
Butane	4.66	0.95	2.83
Decane	5.88	0.48	3.05
Ethane	3.87	1.82	2.90
Heptane	5.81	0.35	2.46
Hexane	5.75	0.26	1.31
Methane	1.94	3.76	4.06
Nonane	6.28	0.87	2.45
Octane	5.77	0.31	2.77
Pentane	0.12	5.96	8.34
Propane	11.39	6.18	4.79
Avg. abs. deviation (%)	5.15	2.10	3.50

CHAPTER 4

GOVERNING EQUATIONS

When a BLEVE occurs, the vapourisation of PLG will result in a region containing a two-phase mixture of liquid and vapour. The expansion of the two-phase region will push the surrounding air aside and this possibly will result in the appearance of a shock in the air. In order to describe these phenomena transport equations are needed expressing conservation of mass, momentum and energy, both in the two-phase region and in the single phase region. In the limit of high Reynolds number viscous and diffusive effects can be neglected and the governing equations take the form of the Euler equations. In this high Reynolds number limit the diffusive mixing between two-phase mixture and air at the interface of the two regions can be neglected. In the case of expansion predominantly in one direction (e.g. along a tunnel), a one-dimensional form of the Euler equations can be used, with the effect of the dimensions transverse to the expansion direction taken into account by an effective area (see below). In what follows we restrict ourselves to this 1D form of the Euler equations.

4.1 For the two-phase flow

According to (28), the conservation-law equations for one-dimensional two-phase flow, neglecting viscosity and axial heat flux terms, are given as

$$A\frac{\partial}{\partial t}(\alpha_k\rho_k)+\frac{\partial}{\partial x}(A\alpha_k\rho_k u_k)=m_{i,k} \tag{4.1}$$

$$\begin{aligned}A\frac{\partial}{\partial t}(\alpha_k\rho_k u_k)+\frac{\partial}{\partial x}(A\alpha_k\rho_k u_k^2)+A\alpha_k\frac{\partial p_k}{\partial x}\\ =m_{i,k}u_k-\tau_{i,k}-\tau_{w,k}-A\alpha_k\rho_k g\frac{dZ}{dx}\end{aligned} \tag{4.2}$$

$$\begin{aligned}A\frac{\partial}{\partial t}\left[\alpha_k\rho_k\left(h_k+\frac{1}{2}u_k^2\right)\right]+\frac{\partial}{\partial x}\left[A\alpha_k\rho_k u_k\left(h_k+\frac{1}{2}u_k^2\right)\right]-A\alpha_k\frac{\partial p_k}{\partial t}\\ =q_{i,k}+q_{w,k}+\tau_{i,k}u_k+m_{i,k}\left(h_k+\frac{1}{2}u_k^2\right)-A\alpha_k\rho_k u_k g\frac{dZ}{dx}\end{aligned} \tag{4.3}$$

In these equations, the subscript $k(=l$ or $g)$ denotes the phase (liquid or vapour). t and x are the independent variables of time and space respectively. g is the gravitational acceleration. The flow quantities α_k, ρ_k, u_k, p_k and h_k are the volume fraction, density, axial velocity, pressure and specific enthalpy of phase k respectively. The source terms $m_{i,k}$, $\tau_{i,k}$, $\tau_{w,k}$, $q_{i,k}$ and $q_{w,k}$ are the interfacial mass flux, interfacial friction, wall friction, interfacial heat flux and wall heat flux into phase k, respectively. Models for the source terms will be presented in Chpt.(6).

Those one-dimensional equations are derived by integrating the three-dimensional equations over the cross-sectional area of the flow, which gives a simplified description of the two-phase flow through a tube or a tunnel. A and Z are the cross-sectional area and the altitude above a horizontal place in three-dimensional space of the tube respectively. In general cases, A and Z can be written as functions of axial distance x.

As introduced in Chpt.(1), the phase volume fractions for two-phase flow satisfy

$$\alpha_l+\alpha_g=1 \tag{4.4}$$

or in terms of the void fraction α,

$$\alpha_g = \alpha \tag{4.5}$$

$$\alpha_l = 1-\alpha \tag{4.6}$$

In order that mass, momentum and energy are conserved at the interface between two phases, the following relations must hold

$$m_{i,l} = -m_{i,g} \tag{4.7}$$

$$m_{i,g}u_g + m_{i,l}u_l = \tau_{i,g} + \tau_{i,l} \tag{4.8}$$

$$q_{i,g} + \tau_{i,g}u_g + m_{i,g}\left(h_g + \frac{1}{2}u_g^2\right) = -\left[q_{i,l} + \tau_{i,l}u_l + m_{i,l}\left(h_l + \frac{1}{2}u_l^2\right)\right] \tag{4.9}$$

4.1.1 1D conservative EVUT Euler equations

1D Conservative Euler equations mentioned in the previous section form a six-equation model with ten unknowns. With Eqn.(4.4) and a certain EOS, we can decrease the number of the independent unknowns to be seven, i.e. α_g, ρ_g, ρ_l, u_g, u_l, p_g and p_l, but still the equations are not closed. It can be made closed by providing an extra equation e.g. an evolution equation for the volume fraction of one phase (8). Alternatively, additional assumptions can be made to decrease the number of the unknowns. Commonly used assumptions are that the velocity and pressure of both phases is the same (Equal-Velocity-assumption) or that the temperature of the two phases is the same (Equal-Temperature-assumption).

Making both assumptions the EVET (Equal-Velocity-Equal-Temperature) model is obtained, where the pressures, velocities and temperatures of two phases become identical. Then the system can be simplified into a three-equation system with three independent unknowns. But as R.L. Ferch discussed in (28), the EVET model is not applicable for the flows with thermal non-equilibrium and unequal velocity effects. Making only the EV-assumption the EVUT (Equal-Velocity-Unequal-Temperature) model is obtained in which the pressure difference and the velocity difference between the two phases are neglected while the temperature difference remains. This is an interesting model for two-phase flow with rapid vapourisation processes, i.e. one has

$$p_l = p_g = p_m \tag{4.10}$$

$$u_l = u_g = u_m \tag{4.11}$$

$$T_l \neq T_g \tag{4.12}$$

As the result of this simplification, the Euler equations for two-phase flow have two continuity equations, one momentum equation and two energy equations and form a five-equation model for two-phase flow with five unknowns : α_g, ρ_g, ρ_l, u_m, p_m. The enthalpy of each phase is related to pressure and density via the chosen EOS. Taken into account that friction force arises from velocity difference in fluid flow, a direct result of EVUT simplification is that the interfacial friction forces between the two phases are zero.

$$\tau_{i,l} = \tau_{i,g} = 0 \tag{4.13}$$

The 1D conservative Euler Equations with the EVUT simplification applied are

$$A\frac{\partial}{\partial t}(\alpha_k\rho_k) + \frac{\partial}{\partial x}(A\alpha_k\rho_k u_m) = m_{i,k} \tag{4.14}$$

$$\begin{aligned} A\frac{\partial}{\partial t}(\alpha_k\rho_k u_m) + \frac{\partial}{\partial x}(A\alpha_k\rho_k u_m^2) + A\alpha_k\frac{\partial p_m}{\partial x} \\ = m_{i,k}u_m - \tau_{w,k} - A\alpha_k\rho_k g\frac{dZ}{dx} \end{aligned} \tag{4.15}$$

$$\begin{aligned} A\frac{\partial}{\partial t}\left[\alpha_k\rho_k\left(h_k + \frac{1}{2}u_m^2\right)\right] + \frac{\partial}{\partial x}\left[A\alpha_k\rho_k u_m\left(h_k + \frac{1}{2}u_m^2\right)\right] - A\alpha_k\frac{\partial p_m}{\partial t} \\ = q_{i,k} + q_{w,k} + m_{i,k}\left(h_k + \frac{1}{2}u_m^2\right) - A\alpha_k\rho_k u_m g\frac{dZ}{dx} \end{aligned} \tag{4.16}$$

in which p_m and u_m as the flow quantities of the two-phase mixture replace p_k and u_k respectively, and $\tau_{i,k}$ has been cancelled.

4.1.2 1D non-conservative EVUT Euler equations

The 1D conservative EVUT Euler equations can be transformed into the following non-conservative form:

$$\frac{\partial}{\partial t}(\alpha_k\rho_k)+\frac{\partial}{\partial x}(\alpha_k\rho_k u_m)=\frac{m_{i,k}}{A}-\alpha_k\rho_k u_m\frac{1}{A}\frac{dA}{dx} \quad (4.17)$$

$$\rho_m\frac{\partial u_m}{\partial t}+\rho_m u_m\frac{\partial u_m}{\partial x}+\frac{\partial p_m}{\partial x}=-\frac{\tau_{w,l}+\tau_{w,g}}{A}-\rho_m g\frac{dZ}{dx} \quad (4.18)$$

$$\alpha_k\rho_k\frac{\partial h_k}{\partial t}+\alpha_k\rho_k u_m\frac{\partial h_k}{\partial x}-\alpha_k\frac{\partial p_m}{\partial t}-\alpha_k u_m\frac{\partial p_m}{\partial x}=\frac{q_{i,k}+q_{w,k}+\tau_{w,k}u_m}{A} \quad (4.19)$$

where $\rho_m=\alpha_g\rho_g+\alpha_l\rho_l$, is the density of the two-phase mixture.

This transformation also makes the left hand side of Eqn.(4.17-4.19) independent of the cross-sectional area A. The steps of the transformation are described below.

Transformation of the continuity equation

Eqn.(4.14) can be rewritten as Eqn.(4.17) by the following steps:

$$A\frac{\partial}{\partial t}(\alpha_k\rho_k)+\frac{\partial}{\partial x}(A\alpha_k\rho_k u_m) = m_{i,k} \quad (4.20)$$

$$A\frac{\partial}{\partial t}(\alpha_k\rho_k)+A\frac{\partial}{\partial x}(\alpha_k\rho_k u_m)+\alpha_k\rho_k u_m\frac{dA}{dx} = m_{i,k} \quad (4.21)$$

$$A\frac{\partial}{\partial t}(\alpha_k\rho_k)+A\frac{\partial}{\partial x}(\alpha_k\rho_k u_m)=m_{i,k} - \alpha_k\rho_k u_m\frac{dA}{dx} \quad (4.22)$$

$$\frac{\partial}{\partial t}(\alpha_k\rho_k)+\frac{\partial}{\partial x}(\alpha_k\rho_k u_m)=\frac{m_{i,k}}{A} - \alpha_k\rho_k u_m\frac{1}{A}\frac{dA}{dx} \quad (4.23)$$

Transformation of the momentum equation

Eqn.(4.15) leads to Eqn.(4.18) by the following steps:

(1) Use the differentiation product rule on the first two partial derivatives in Eqn.(4.15).

$$\left[Au_m\frac{\partial}{\partial t}(\alpha_k\rho_k)+A\alpha_k\rho_k\frac{\partial u_m}{\partial t}\right]+\left[A\alpha_k\rho_k u_m\frac{\partial u_m}{\partial x}+u_m\frac{\partial}{\partial x}(A\alpha_k\rho_k u_m)\right]$$
$$\Rightarrow u_m\underbrace{\left[A\frac{\partial}{\partial t}(\alpha_k\rho_k)+\frac{\partial}{\partial x}(A\alpha_k\rho_k u_m)\right]}+\left[A\alpha_k\rho_k\frac{\partial u_m}{\partial t}+A\alpha_k\rho_k u_m\frac{\partial u_m}{\partial x}\right]$$

(2) The underlined part is equal to $m_{i,k}$ in Eqn.(4.14), therefore Eqn.(4.15) becomes

$$m_{i,k}u_m+\left[A\alpha_k\rho_k\frac{\partial u_m}{\partial t}+A\alpha_k\rho_k u_m\frac{\partial u_m}{\partial x}\right]+A\alpha_k\frac{\partial p_m}{\partial x}$$
$$=m_{i,k}u_m-\tau_{w,k}-A\alpha_k\rho_k g\frac{dZ}{dx} \tag{4.24}$$

(3) Delete $m_{i,k}u_m$ from both sides,

$$A\alpha_k\rho_k\frac{\partial u_m}{\partial t}+A\alpha_k\rho_k u_m\frac{\partial u_m}{\partial x}+A\alpha_k\frac{\partial p_m}{\partial x}=-\tau_{w,k}-A\alpha_k\rho_k g\frac{dZ}{dx} \tag{4.25}$$

(4) The momentum equations can be integrated into one equation as the two phases have the same velocity. Write the momentum equations for liquid and vapour phase respectively

$$A\alpha_l\rho_l\frac{\partial u_m}{\partial t}+A\alpha_l\rho_l u_m\frac{\partial u_m}{\partial x}+A\alpha_l\frac{\partial p_m}{\partial x}=-\tau_{w,l}-A\alpha_l\rho_l g\frac{dZ}{dx} \tag{4.26}$$
$$A\alpha_g\rho_g\frac{\partial u_m}{\partial t}+A\alpha_g\rho_g u_m\frac{\partial u_m}{\partial x}+A\alpha_g\frac{\partial p_m}{\partial x}=-\tau_{w,g}-A\alpha_g\rho_g g\frac{dZ}{dx} \tag{4.27}$$

(5) Add up the two equations

$$A(\alpha_l\rho_l+\alpha_g\rho_g)\frac{\partial u_m}{\partial t}+A(\alpha_l\rho_l+\alpha_g\rho_g)u_m\frac{\partial u_m}{\partial x}+A(\alpha_g+\alpha_g)\frac{\partial p_m}{\partial x}$$
$$=-\tau_{w,l}-\tau_{w,g}-A(\alpha_l\rho_l+\alpha_g\rho_g)g\frac{dZ}{dx} \tag{4.28}$$

Because of $\rho_m = \alpha_g \rho_g + \alpha_l \rho_l$ and $\alpha_l + \alpha_g = 1$,

$$A\rho_m \frac{\partial u_m}{\partial t} + A\rho_m u_m \frac{\partial u_m}{\partial x} + A\frac{\partial p_m}{\partial x} = -\tau_{w,l} - \tau_{w,g} - A\rho_m g \frac{dZ}{dx} \tag{4.29}$$

(6) Moving A to the right hand side of the equation, we finally get Eqn.(4.18) as

$$\rho_m \frac{\partial u_m}{\partial t} + \rho_m u_m \frac{\partial u_m}{\partial x} + \frac{\partial p_m}{\partial x} = -\frac{\tau_{w,l} + \tau_{w,g}}{A} - \rho_m g \frac{dZ}{dx}$$

Transformation of the energy equation

The transformation of Eqn.(4.16) into Eqn.(4.19) is taking similar steps.

(1) Use the differentiation product rule on the first two partial derivatives in Eqn.(4.16)

$$A\frac{\partial}{\partial t}\left[\alpha_k \rho_k \left(h_k + \frac{1}{2}u_m^2\right)\right] + \frac{\partial}{\partial x}\left[A\alpha_k \rho_k u_m \left(h_k + \frac{1}{2}u_m^2\right)\right]$$

$$\Rightarrow \left[\left(h_k + \frac{1}{2}u_m^2\right)A\frac{\partial(\alpha_k \rho_k)}{\partial t} + A\alpha_k \rho_k \frac{\partial}{\partial t}\left(h_k + \frac{1}{2}u_m^2\right)\right]$$

$$+\left[\left(h_k + \frac{1}{2}u_m^2\right)\frac{\partial}{\partial x}\left(A\alpha_k \rho_k u_m\right) + A\alpha_k \rho_k u_m \frac{\partial}{\partial x}\left(h_k + \frac{1}{2}u_m^2\right)\right]$$

(2) Rewrite the underlined part as

$$\left(h_k + \frac{1}{2}u_m^2\right)A\frac{\partial(\alpha_k \rho_k)}{\partial t} + \left(h_k + \frac{1}{2}u_m^2\right)\frac{\partial}{\partial x}\left(A\alpha_k \rho_k u_m\right)$$

$$\Rightarrow \left(h_k + \frac{1}{2}u_m^2\right)\left[A\frac{\partial(\alpha_k \rho_k)}{\partial t} + \frac{\partial}{\partial x}\left(A\alpha_k \rho_k u_m\right)\right]$$

Insert Eqn.(4.14) and the underlined part finally cancels out the same term on the right hand side of Eqn.(4.16) as

$$(h_k+\frac{1}{2}u_m^2)\Big[A\frac{\partial(\alpha_k\rho_k)}{\partial t}+\frac{\partial}{\partial x}\Big(A\alpha_k\rho_k u_m\Big)\Big]\Rightarrow\Big(h_k+\frac{1}{2}u_m^2\Big)m_{i,k}$$

(3) Now the energy equation becomes

$$\begin{aligned}A\alpha_k\rho_k\frac{\partial}{\partial t}\Big(h_k+\frac{1}{2}u_m^2\Big)+A\alpha_k\rho_k u_m\frac{\partial}{\partial x}\Big(h_k+\frac{1}{2}u_m^2\Big)\\ -A\alpha_k\frac{\partial p_m}{\partial t}=q_{i,k}+q_{w,k}-A\alpha_k\rho_k u_m g\frac{dZ}{dx}\end{aligned}\tag{4.30}$$

$$\begin{aligned}\Big[A\alpha_k\rho_k\frac{\partial h_k}{\partial t}+A\alpha_k\rho_k\frac{\partial}{\partial t}\Big(\frac{1}{2}u_m^2\Big)\Big]+\Big[A\alpha_k\rho_k u_m\frac{\partial h_k}{\partial x}\\ +A\alpha_k\rho_k u_m\frac{\partial}{\partial x}\Big(\frac{1}{2}u_m^2\Big)\Big]-A\alpha_k\frac{\partial p_m}{\partial t}=q_{i,k}+q_{w,k}-A\alpha_k\rho_k u_m g\frac{dZ}{dx}\end{aligned}\tag{4.31}$$

(4) Use u_m times Eqn.(4.25)

$$\begin{aligned}u_m\Big[A\alpha_k\rho_k\frac{\partial u_m}{\partial t}+A\alpha_k\rho_k u_m\frac{\partial u_m}{\partial x}+A\alpha_k\frac{\partial p_m}{\partial x}\Big]\\ =u_m\Big[-\tau_{w,k}-A\alpha_k\rho_k g\frac{dZ}{dx}\Big]\end{aligned}\tag{4.32}$$

$$\begin{aligned}A\alpha_k\rho_k\frac{\partial}{\partial t}\Big(\frac{1}{2}u_m^2\Big)+A\alpha_k\rho_k u_m\frac{\partial}{\partial x}\Big(\frac{1}{2}u_m^2\Big)+A\alpha_k u_m\frac{\partial p_m}{\partial x}\\ =-\tau_{w,k}u_m-A\alpha_k\rho_k u_m g\frac{dZ}{dx}\end{aligned}\tag{4.33}$$

(5) Subtract Eqn.(4.33) from Eqn.(4.31)

$$\begin{aligned}A\alpha_k\rho_k\frac{\partial h_k}{\partial t}+A\alpha_k\rho_k u_m\frac{\partial h_k}{\partial x}-A\alpha_k\frac{\partial p_m}{\partial t}-A\alpha_k u_m\frac{\partial p_m}{\partial x}\\ =q_{i,k}+q_{w,k}+\tau_{w,k}u_m\end{aligned}\tag{4.34}$$

(6) Move A to the right hand side of the equation, we finally get Eqn.(4.19) as

$$\alpha_k \rho_k \frac{\partial h_k}{\partial t} + \alpha_k \rho_k u_m \frac{\partial h_k}{\partial x} - \alpha_k \frac{\partial p_m}{\partial t} - \alpha_k u_m \frac{\partial p_m}{\partial x} = \frac{q_{i,k} + q_{w,k} + \tau_{w,k} u_m}{A}$$

Apparently, there are eight unknowns in the left hand side of the 1D non-conservative EVUT Euler equations for two-phase flow, namely p_m, u_m, α_k, ρ_k and h_k. With Eqn.(4.4), two unknowns of α_k could be replaced by one unknown α, the void fraction. Moreover, the densities will be given as $\rho_k = \rho_k(p_m, h_k)$ by EOS. Finally, we have five unknowns, p_m, u_m, α, h_g and h_l and five equations. This set of one-dimensional equations can be solved using the method of characteristics. In order to do so the equations need to be first brought in characteristic form.

4.1.3 Characteristic form

Here we explain in detail how the equations are brought in characteristic form. We successively consider the equation for enthalpy of the two phases, the equation for the void fraction and the equations for mixture pressure and mixture velocity.

Equations for the enthalpies

Dividing Eqn.(4.19) by $\alpha_k \rho_k$, we get the two enthalpy equations for the liquid and vapour respectively as

$$\frac{\partial h_g}{\partial t} + u_m \frac{\partial h_g}{\partial x} - \frac{1}{\rho_g}\left(\frac{\partial p_m}{\partial t} + u_m \frac{\partial p_m}{\partial x}\right) = C_4 \tag{4.35}$$

$$\frac{\partial h_l}{\partial t} + u_m \frac{\partial h_l}{\partial x} - \frac{1}{\rho_l}\left(\frac{\partial p_m}{\partial t} + u_m \frac{\partial p_m}{\partial x}\right) = C_5 \tag{4.36}$$

in which

$$C_4 \equiv \frac{q_{i,g} + q_{w,g} + \tau_{w,g} u_m}{\alpha \rho_g A} \tag{4.37}$$

$$C_5 \equiv \frac{q_{i,l} + q_{w,l} + \tau_{w,l} u_m}{(1-\alpha)\rho_l A} \tag{4.38}$$

Note that it is assumed here that $0 < \alpha < 1$ since the flow is two-phase.

Equation for the void fraction

The phase densities are given by equation of state as

$$\rho_k = \rho_k(p_m, h_k) \tag{4.39}$$

therefore we have

$$\frac{\partial \rho_k}{\partial t} = \frac{\partial \rho_k}{\partial h_k}\frac{\partial h_k}{\partial t} + \frac{\partial \rho_k}{\partial p_m}\frac{\partial p_m}{\partial t} \tag{4.40}$$

$$\frac{\partial \rho_k}{\partial x} = \frac{\partial \rho_k}{\partial h_k}\frac{\partial h_k}{\partial x} + \frac{\partial \rho_k}{\partial p_m}\frac{\partial p_m}{\partial x} \tag{4.41}$$

or

$$\frac{\partial \rho_k}{\partial h_k}\frac{\partial h_k}{\partial t} = \frac{\partial \rho_k}{\partial t} - \frac{\partial \rho_k}{\partial p_m}\frac{\partial p_m}{\partial t} \tag{4.42}$$

$$\frac{\partial \rho_k}{\partial h_k}\frac{\partial h_k}{\partial x} = \frac{\partial \rho_k}{\partial x} - \frac{\partial \rho_k}{\partial p_m}\frac{\partial p_m}{\partial x} \tag{4.43}$$

We take following steps to derive the equation for the void fraction α:

(1) Use $\alpha_g \partial \rho_g / \partial h_g$ times Eqn.(4.35)

$$\alpha_g \frac{\partial \rho_g}{\partial h_g}\Big[\frac{\partial h_g}{\partial t} + u_m \frac{\partial h_g}{\partial x} - \frac{1}{\rho_g}\Big(\frac{\partial p_m}{\partial t} + u_m \frac{\partial p_m}{\partial x}\Big)\Big] = C_4 \alpha_g \frac{\partial \rho_g}{\partial h_g} \tag{4.44}$$

$$\alpha_g \frac{\partial \rho_g}{\partial h_g}\Big(\frac{\partial h_g}{\partial t} + u_m \frac{\partial h_g}{\partial x}\Big) - \frac{\alpha_g}{\rho_g}\frac{\partial \rho_g}{\partial h_g}\Big(\frac{\partial p_m}{\partial t} + u_m \frac{\partial p_m}{\partial x}\Big) = C_4 \alpha_g \frac{\partial \rho_g}{\partial h_g} \tag{4.45}$$

$$\begin{aligned} &\alpha_g\Big[\frac{\partial \rho_g}{\partial t} - \frac{\partial \rho_g}{\partial p_m}\frac{\partial p_m}{\partial t} + u_m\Big(\frac{\partial \rho_g}{\partial x} - \frac{\partial \rho_g}{\partial p_m}\frac{\partial p_m}{\partial x}\Big)\Big] \\ &-\frac{\alpha_g}{\rho_g}\frac{\partial \rho_g}{\partial h_g}\Big[\frac{\partial p_m}{\partial t} + u_m \frac{\partial p_m}{\partial x}\Big] = C_4 \alpha_g \frac{\partial \rho_g}{\partial h_g} \end{aligned} \tag{4.46}$$

$$\begin{aligned} &\alpha_g\Big[\frac{\partial \rho_g}{\partial t} + u_m \frac{\partial \rho_g}{\partial x}\Big] - \alpha_g\Big[\frac{\partial \rho_g}{\partial p_m}\frac{\partial p_m}{\partial t} + u_m \frac{\partial \rho_g}{\partial p_m}\frac{\partial p_m}{\partial x}\Big] \\ &-\frac{\alpha_g}{\rho_g}\frac{\partial \rho_g}{\partial h_g}\Big[\frac{\partial p_m}{\partial t} + u_m \frac{\partial p_m}{\partial x}\Big] = C_4 \alpha_g \frac{\partial \rho_g}{\partial h_g} \end{aligned} \tag{4.47}$$

$$\begin{aligned} &\underline{\alpha_g\Big[\frac{\partial \rho_g}{\partial t} + u_m \frac{\partial \rho_g}{\partial x}\Big]} - \alpha_g\Big(\frac{\partial \rho_g}{\partial p_m} + \frac{1}{\rho_g}\frac{\partial \rho_g}{\partial h_g}\Big)\Big[\frac{\partial p_m}{\partial t} + u_m \frac{\partial p_m}{\partial x}\Big] \\ &= C_4 \alpha_g \frac{\partial \rho_g}{\partial h_g} \end{aligned} \tag{4.48}$$

(2) The underlined part can be found from Eqn.(4.17)

$$\frac{\partial}{\partial t}(\alpha_g \rho_g) + \frac{\partial}{\partial x}(\alpha_g \rho_g u_m) = \frac{m_{i,g}}{A} - \alpha_g \rho_g u_m \frac{1}{A}\frac{dA}{dx} \tag{4.49}$$

$$\begin{aligned} &\Big[\alpha_g \frac{\partial \rho_g}{\partial t} + \rho_g \frac{\partial \alpha_g}{\partial t}\Big] + \Big[\alpha_g u_m \frac{\partial \rho_g}{\partial x} + \alpha_g \rho_g \frac{\partial u_m}{\partial x} + \rho_g u_m \frac{\partial \alpha_g}{\partial x}\Big] \\ &= \frac{m_{i,g}}{A} - \alpha_g \rho_g u_m \frac{1}{A}\frac{dA}{dx} \end{aligned} \tag{4.50}$$

$$\begin{aligned} &\underline{\alpha_g\Big[\frac{\partial \rho_g}{\partial t} + u_m \frac{\partial \rho_g}{\partial x}\Big]} + \Big[\rho_g \frac{\partial \alpha_g}{\partial t} + \alpha_g \rho_g \frac{\partial u_m}{\partial x} + \rho_g u_m \frac{\partial \alpha_g}{\partial x}\Big] \\ &= \frac{m_{i,g}}{A} - \alpha_g \rho_g u_m \frac{1}{A}\frac{dA}{dx} \end{aligned} \tag{4.51}$$

(3) Eqn.(4.51) minus Eqn.(4.48) gives

$$\Big[\rho_g \frac{\partial \alpha_g}{\partial t} + \rho_g u_m \frac{\partial \alpha_g}{\partial x}\Big] + \alpha_g \Big(\frac{\partial \rho_g}{\partial p_m} + \frac{1}{\rho_g}\frac{\partial \rho_g}{\partial h_g}\Big)\Big[\frac{\partial p_m}{\partial t} + u_m \frac{\partial p_m}{\partial x}\Big] + \alpha_g \rho_g \frac{\partial u_m}{\partial x} = \frac{m_{i,g}}{A} - \alpha_g \rho_g u_m \frac{1}{A}\frac{dA}{dx} - C_4 \alpha_g \frac{\partial \rho_g}{\partial h_g} \tag{4.52}$$

(4) If Eqn.(4.52) is divided by ρ_g, it results in

$$\Big[\frac{\partial \alpha_g}{\partial t} + u_m \frac{\partial \alpha_g}{\partial x}\Big] + \frac{\alpha_g}{\rho_g}\Big(\frac{\partial \rho_g}{\partial p_m} + \frac{1}{\rho_g}\frac{\partial \rho_g}{\partial h_g}\Big)\Big[\frac{\partial p_m}{\partial t} + u_m \frac{\partial p_m}{\partial x}\Big] + \alpha_g \frac{\partial u_m}{\partial x} = \frac{m_{i,g}}{\rho_g A} - \alpha_g u_m \frac{1}{A}\frac{dA}{dx} - C_4 \frac{\alpha_g}{\rho_g}\frac{\partial \rho_g}{\partial h_g} \tag{4.53}$$

(5) We can get the corresponding equation for the liquid phase as

$$\Big[\frac{\partial \alpha_l}{\partial t} + u_m \frac{\partial \alpha_l}{\partial x}\Big] + \frac{\alpha_l}{\rho_l}\Big(\frac{\partial \rho_l}{\partial p_m} + \frac{1}{\rho_l}\frac{\partial \rho_l}{\partial h_l}\Big)\Big[\frac{\partial p_m}{\partial t} + u_m \frac{\partial p_m}{\partial x}\Big] + \alpha_l \frac{\partial u_m}{\partial x} = \frac{m_{i,l}}{\rho_l A} - \alpha_l u_m \frac{1}{A}\frac{dA}{dx} - C_5 \frac{\alpha_l}{\rho_l}\frac{\partial \rho_l}{\partial h_l} \tag{4.54}$$

(6) Eqn.(4.53) times α_l minus Eqn.(4.60) times α_g gives

$$\begin{aligned}
&\alpha_l\Big[\frac{\partial \alpha_g}{\partial t} + u_m \frac{\partial \alpha_g}{\partial x}\Big] + \alpha_l \frac{\alpha_g}{\rho_g}\Big(\frac{\partial \rho_g}{\partial p_m} + \frac{1}{\rho_g}\frac{\partial \rho_g}{\partial h_g}\Big)\Big[\frac{\partial p_m}{\partial t} + u_m \frac{\partial p_m}{\partial x}\Big] \\
&-\alpha_g\Big[\frac{\partial \alpha_l}{\partial t} + u_m \frac{\partial \alpha_l}{\partial x}\Big] - \alpha_g \frac{\alpha_l}{\rho_l}\Big(\frac{\partial \rho_l}{\partial p_m} + \frac{1}{\rho_l}\frac{\partial \rho_l}{\partial h_l}\Big)\Big[\frac{\partial p_m}{\partial t} + u_m \frac{\partial p_m}{\partial x}\Big] \\
&+\alpha_l \alpha_g \frac{\partial u_m}{\partial x} - \alpha_g \alpha_l \frac{\partial u_m}{\partial x} = \alpha_l\Big[\frac{m_{i,g}}{\rho_g A} - \alpha_g u_m \frac{1}{A}\frac{dA}{dx} - C_4 \frac{\alpha_g}{\rho_g}\frac{\partial \rho_g}{\partial h_g}\Big] \\
&\qquad -\alpha_g\Big[\frac{m_{i,l}}{\rho_l A} - \alpha_l u_m \frac{1}{A}\frac{dA}{dx} - C_5 \frac{\alpha_l}{\rho_l}\frac{\partial \rho_l}{\partial h_l}\Big]
\end{aligned} \tag{4.55}$$

(7) The underlined parts are canceled out, giving

$$\begin{aligned}
&\alpha_l\Big[\frac{\partial\alpha_g}{\partial t}+u_m\frac{\partial\alpha_g}{\partial x}\Big]+\alpha_l\frac{\alpha_g}{\rho_g}\Big(\frac{\partial\rho_g}{\partial p_m}+\frac{1}{\rho_g}\frac{\partial\rho_g}{\partial h_g}\Big)\Big[\frac{\partial p_m}{\partial t}+u_m\frac{\partial p_m}{\partial x}\Big]\\
&-\alpha_g\Big[\frac{\partial\alpha_l}{\partial t}+u_m\frac{\partial\alpha_l}{\partial x}\Big]-\alpha_g\frac{\alpha_l}{\rho_l}\Big(\frac{\partial\rho_l}{\partial p_m}+\frac{1}{\rho_l}\frac{\partial\rho_l}{\partial h_l}\Big)\Big[\frac{\partial p_m}{\partial t}+u_m\frac{\partial p_m}{\partial x}\Big]\\
&\qquad=\alpha_l\Big[\frac{m_{i,g}}{\rho_g A}-C_4\frac{\alpha_g}{\rho_g}\frac{\partial\rho_g}{\partial h_g}\Big]-\alpha_g\Big[\frac{m_{i,l}}{\rho_l A}-C_5\frac{\alpha_l}{\rho_l}\frac{\partial\rho_l}{\partial h_l}\Big] \qquad (4.56)
\end{aligned}$$

(8) Rearranging terms leads to

$$\begin{aligned}
&\underline{\Big[\alpha_l\frac{\partial\alpha_g}{\partial t}-\alpha_g\frac{\partial\alpha_l}{\partial t}\Big]}+u_m\underline{\Big[\alpha_l\frac{\partial\alpha_g}{\partial x}-\alpha_g\frac{\partial\alpha_l}{\partial x}\Big]}\\
&+\alpha_l\alpha_g\Big[\frac{1}{\rho_g}\Big(\frac{\partial\rho_g}{\partial p_m}+\frac{1}{\rho_g}\frac{\partial\rho_g}{\partial h_g}\Big)-\frac{1}{\rho_l}\Big(\frac{\partial\rho_l}{\partial p_m}+\frac{1}{\rho_l}\frac{\partial\rho_l}{\partial h_l}\Big)\Big]\Big[\frac{\partial p_m}{\partial t}+u_m\frac{\partial p_m}{\partial x}\Big]\\
&\qquad=\underline{\Big[\frac{\alpha_l m_{i,g}}{\rho_g A}-\frac{\alpha_g m_{i,l}}{\rho_l A}\Big]}-\alpha_l\alpha_g\Big[\frac{1}{\rho_g}\frac{\partial\rho_g}{\partial h_g}C_4-\frac{1}{\rho_l}\frac{\partial\rho_l}{\partial h_l}C_5\Big] \qquad (4.57)
\end{aligned}$$

(9) Since $\alpha_g=\alpha$, $\alpha_l=1-\alpha$, $\rho_m=\alpha_g\rho_g+\alpha_l\rho_l$ and $m_{i,g}=-m_{i,l}$, we can simplify the underlined parts in Eqn.(4.57) as

$$\begin{aligned}
\Big[\alpha_l\frac{\partial\alpha_g}{\partial t}-\alpha_g\frac{\partial\alpha_l}{\partial t}\Big] &= (1-\alpha)\frac{\partial\alpha}{\partial t}-\alpha\frac{\partial(1-\alpha)}{\partial t}=\frac{\partial\alpha}{\partial t}\\
\Big[\alpha_l\frac{\partial\alpha_g}{\partial x}-\alpha_g\frac{\partial\alpha_l}{\partial x}\Big] &= (1-\alpha)\frac{\partial\alpha}{\partial x}-\alpha\frac{\partial(1-\alpha)}{\partial x}=\frac{\partial\alpha}{\partial x}\\
\frac{\alpha_l m_{i,g}}{\rho_g A}-\frac{\alpha_g m_{i,l}}{\rho_l A} &= \frac{\alpha_l\rho_l m_{i,g}-\alpha_g\rho_g m_{i,l}}{\rho_g\rho_l A}=\frac{\alpha_l\rho_l m_{i,g}+\alpha_g\rho_g m_{i,g}}{\rho_g\rho_l A}\\
&= \frac{(\alpha_l\rho_l+\alpha_g\rho_g)m_{i,g}}{\rho_g\rho_l A}=\frac{\rho_m}{\rho_g\rho_l}\frac{m_{i,g}}{A}
\end{aligned}$$

(10) Finally after α_l, α_g and $m_{i,g}$ are eliminated, the equation for the void fraction α is found to be

$$\Big[\frac{\partial \alpha}{\partial t}+u_m\frac{\partial \alpha}{\partial x}\Big]+\alpha(1-\alpha)\Big[\frac{1}{\rho_g}\Big(\frac{\partial \rho_g}{\partial p_m}+\frac{1}{\rho_g}\frac{\partial \rho_g}{\partial h_g}\Big)$$
$$-\frac{1}{\rho_l}\Big(\frac{\partial \rho_l}{\partial p_m}+\frac{1}{\rho_l}\frac{\partial \rho_l}{\partial h_l}\Big)\Big]\Big[\frac{\partial p_m}{\partial t}+u_m\frac{\partial p_m}{\partial x}\Big]=C_3$$

in which

$$C_3\equiv\frac{\rho_m}{\rho_g\rho_l}\frac{m_{i,g}}{A}-\alpha(1-\alpha)\Big[\frac{1}{\rho_g}\frac{\partial \rho_g}{\partial h_g}C_4-\frac{1}{\rho_l}\frac{\partial \rho_l}{\partial h_l}C_5\Big] \tag{4.58}$$

We define the sonic speed for each phase a_k as

$$a_k^{-2}=\frac{\partial \rho_k}{\partial p}+\frac{1}{\rho_k}\frac{\partial \rho_k}{\partial h_k} \tag{4.59}$$

The equation for the void fraction α can be rewritten as

$$\Big[\frac{\partial \alpha}{\partial t}+u_m\frac{\partial \alpha}{\partial x}\Big]+\alpha(1-\alpha)\Big(\frac{1}{\rho_g a_g^2}-\frac{1}{\rho_l a_l^2}\Big)\Big[\frac{\partial p_m}{\partial t}+u_m\frac{\partial p_m}{\partial x}\Big]=C_3 \tag{4.60}$$

Equations for the mixture pressure and mixture velocity

Under the assumption of EVUT, the two phases have the same pressure and the same velocity. Therefore it is possible to directly solve for the equations for the mixture pressure and the mixture velocity. These equations are obtained through following steps:

(1) Use differentiation chain-rule on Eqn.(4.17) as

$$\frac{\partial}{\partial t}(\alpha_k\rho_k)+\frac{\partial}{\partial x}(\alpha_k\rho_k u_m)=\frac{m_{i,k}}{A}-\alpha_k\rho_k u_m\frac{1}{A}\frac{dA}{dx} \tag{4.61}$$

$$\begin{aligned}\alpha_k\frac{\partial\rho_k}{\partial t}+\rho_k\frac{\partial\alpha_k}{\partial t}+u_m\alpha_k\frac{\partial\rho_k}{\partial x}+u_m\rho_k\frac{\partial\alpha_k}{\partial x}+\alpha_k\rho_k\frac{\partial u_m}{\partial x}\\ =\frac{m_{i,k}}{A}-\alpha_k\rho_k u_m\frac{1}{A}\frac{dA}{dx}\end{aligned} \tag{4.62}$$

(2) Divided by ρ_k

$$\frac{\alpha_k}{\rho_k}\frac{\partial\rho_k}{\partial t}+\frac{\partial\alpha_k}{\partial t}+u_m\frac{\alpha_k}{\rho_k}\frac{\partial\rho_k}{\partial x}+u_m\frac{\partial\alpha_k}{\partial x}+\alpha_k\frac{\partial u_m}{\partial x}=\frac{m_{i,k}}{\rho_k A}-\alpha_k u_m\frac{1}{A}\frac{dA}{dx} \tag{4.63}$$

(3)Add up the equations for the two-phases and use Eqn.(4.4) and (4.7)

$$\begin{aligned}\frac{\alpha_g}{\rho_g}\frac{\partial\rho_g}{\partial t}+\frac{\alpha_l}{\rho_l}\frac{\partial\rho_l}{\partial t}+\frac{\partial\alpha_g}{\partial t}+\frac{\partial\alpha_l}{\partial t}+u_m\frac{\alpha_g}{\rho_g}\frac{\partial\rho_g}{\partial x}+u_m\frac{\alpha_l}{\rho_l}\frac{\partial\rho_l}{\partial x}\\ +u_m\frac{\partial\alpha_g}{\partial x}+u_m\frac{\partial\alpha_l}{\partial x}+\alpha_g\frac{\partial u_m}{\partial x}+\alpha_l\frac{\partial u_m}{\partial x}\\ =\frac{m_{i,g}}{\rho_g A}+\frac{m_{i,l}}{\rho_l A}-\alpha_g u_m\frac{1}{A}\frac{dA}{dx}-\alpha_l u_m\frac{1}{A}\frac{dA}{dx}\end{aligned} \tag{4.64}$$

$$\begin{aligned}\underline{\left(\frac{\alpha_g}{\rho_g}\frac{\partial\rho_g}{\partial t}+u_m\frac{\alpha_g}{\rho_g}\frac{\partial\rho_g}{\partial x}\right)}+\left(\frac{\alpha_l}{\rho_l}\frac{\partial\rho_l}{\partial t}+u_m\frac{\alpha_l}{\rho_l}\frac{\partial\rho_l}{\partial x}\right)+\frac{\partial u_m}{\partial x}\\ =\frac{m_{i,g}}{A}\left(\frac{1}{\rho_g}-\frac{1}{\rho_l}\right)-u_m\frac{1}{A}\frac{dA}{dx}\end{aligned} \tag{4.65}$$

(4) Insert Eqn.(4.40) and (4.41) into the underlined parts, we get

$$
\begin{aligned}
& \frac{\alpha_g}{\rho_g}\frac{\partial \rho_g}{\partial t} + u_m \frac{\alpha_g}{\rho_g}\frac{\partial \rho_g}{\partial x} \\
= \; & \frac{\alpha_g}{\rho_g}\Big(\frac{\partial \rho_g}{\partial h_g}\frac{\partial h_g}{\partial t} + \frac{\partial \rho_g}{\partial p_m}\frac{\partial p_m}{\partial t}\Big) + u_m \frac{\alpha_g}{\rho_g}\Big(\frac{\partial \rho_g}{\partial h_g}\frac{\partial h_g}{\partial x} + \frac{\partial \rho_g}{\partial p_m}\frac{\partial p_m}{\partial x}\Big) \\
= \; & \frac{\alpha_g}{\rho_g}\frac{\partial \rho_g}{\partial h_g}\Big(\frac{\partial h_g}{\partial t} + u_m \frac{\partial h_g}{\partial x}\Big) + \frac{\alpha_g}{\rho_g}\frac{\partial \rho_g}{\partial p_m}\Big(\frac{\partial p_m}{\partial t} + u_m \frac{\partial p_m}{\partial x}\Big) \\
= \; & \frac{\alpha_g}{\rho_g}\frac{\partial \rho_g}{\partial h_g}\Big[C_4 + \frac{1}{\rho_g}\Big(\frac{\partial p_m}{\partial t} + u_m \frac{\partial p_m}{\partial x}\Big)\Big] + \frac{\alpha_g}{\rho_g}\frac{\partial \rho_g}{\partial p_m}\Big(\frac{\partial p_m}{\partial t} + u_m \frac{\partial p_m}{\partial x}\Big); \\
& \frac{\alpha_l}{\rho_l}\frac{\partial \rho_l}{\partial t} + u_m \frac{\alpha_l}{\rho_l}\frac{\partial \rho_l}{\partial x} \\
= \; & \frac{\alpha_l}{\rho_l}\frac{\partial \rho_l}{\partial h_l}\Big[C_5 + \frac{1}{\rho_l}\Big(\frac{\partial p_m}{\partial t} + u_m \frac{\partial p_m}{\partial x}\Big)\Big] + \frac{\alpha_l}{\rho_l}\frac{\partial \rho_l}{\partial p_m}\Big(\frac{\partial p_m}{\partial t} + u_m \frac{\partial p_m}{\partial x}\Big)
\end{aligned}
$$

(5) Put it back, we get

$$
\begin{aligned}
& \frac{\alpha_g}{\rho_g}\frac{\partial \rho_g}{\partial h_g}\Big[C_4 + \frac{1}{\rho_g}\Big(\frac{\partial p_m}{\partial t} + u_m \frac{\partial p_m}{\partial x}\Big)\Big] + \frac{\alpha_g}{\rho_g}\frac{\partial \rho_g}{\partial p_m}\Big(\frac{\partial p_m}{\partial t} + u_m \frac{\partial p_m}{\partial x}\Big) \\
+ & \frac{\alpha_l}{\rho_l}\frac{\partial \rho_l}{\partial h_l}\Big[C_5 + \frac{1}{\rho_l}\Big(\frac{\partial p_m}{\partial t} + u_m \frac{\partial p_m}{\partial x}\Big)\Big] + \frac{\alpha_l}{\rho_l}\frac{\partial \rho_l}{\partial p_m}\Big(\frac{\partial p_m}{\partial t} + u_m \frac{\partial p_m}{\partial x}\Big) \\
& + \frac{\partial u_m}{\partial x} = \frac{m_{i,g}}{A}\Big(\frac{1}{\rho_g} - \frac{1}{\rho_l}\Big) - u_m \frac{1}{A}\frac{dA}{dx}
\end{aligned} \tag{4.66}
$$

(6) Move the terms containing C_4 and C_5 to the right-hand side of the equation and define C_1 as

$$
C_1 \equiv \frac{m_{i,g}}{A}\Big(\frac{1}{\rho_g} - \frac{1}{\rho_l}\Big) - u_m \frac{1}{A}\frac{dA}{dx} - \frac{\alpha}{\rho_g}\frac{\partial \rho_g}{\partial h_g}C_4 - \frac{(1-\alpha)}{\rho_l}\frac{\partial \rho_l}{\partial h_l}C_5 \tag{4.67}
$$

$$\Big(\frac{\partial p_m}{\partial t}+u_m\frac{\partial p_m}{\partial x}\Big)\Big[\frac{\alpha_g}{\rho_g}\Big(\frac{\partial \rho_g}{\partial h_g}\frac{1}{\rho_g}+\frac{\partial \rho_g}{\partial p_m}\Big) +\frac{\alpha_g}{\rho_g}\Big(\frac{\partial \rho_g}{\partial h_g}\frac{1}{\rho_g}+\frac{\partial \rho_g}{\partial p_m}\Big)\Big]+\frac{\partial u_m}{\partial x}=C_1 \tag{4.68}$$

(7) Because the sonic speed of phase k has been given as a_k in Eqn.(4.59) and the sonic speed of the mixture, denoted a_m, is defined by

$$a_m^{-2}=\rho_m\Big(\frac{\alpha_g}{\rho_g a_g^2}+\frac{\alpha_l}{\rho_l a_l^2}\Big) \tag{4.69}$$

finally we have an equation with two unknowns p_m and u_m as

$$\begin{aligned}\Big(\frac{\partial p_m}{\partial t}+u_m\frac{\partial p_m}{\partial x}\Big)\Big(\frac{\alpha_g}{\rho_g}\frac{1}{a_g^2}+\frac{\alpha_l}{\rho_l}\frac{1}{a_l^2}\Big)+\frac{\partial u_m}{\partial x}&=C_1\\ \Big(\frac{\partial p_m}{\partial t}+u_m\frac{\partial p_m}{\partial x}\Big)\frac{1}{\rho_m a_m^2}+\frac{\partial u_m}{\partial x}&=C_1\\ \frac{\partial p_m}{\partial t}+u_m\frac{\partial p_m}{\partial x}+\rho_m a_m^2\frac{\partial u_m}{\partial x}&=\rho_m a_m^2 C_1\end{aligned} \tag{4.70}$$

(8) Usin Eqn.(4.70) and subtracting the momentum equation Eqn.(4.18) multiplied with a_m, we can derive below two equations exactly the same as in (28) for solving the mixture pressure and the mixture velocity

$$\begin{aligned}\frac{\partial p_m}{\partial t}+(u_m+a_m)\frac{\partial p_m}{\partial x}+\rho_m a_m\Big[\frac{\partial u_m}{\partial t}+(u_m+a_m)\frac{\partial u_m}{\partial x}\Big]&\\ =\rho_m a_m^2 C_1+a_m C_2&\end{aligned} \tag{4.71}$$

$$\begin{aligned}\frac{\partial p_m}{\partial t}+(u_m-a_m)\frac{\partial p_m}{\partial x}-\rho_m a_m\Big[\frac{\partial u_m}{\partial t}+(u_m-a_m)\frac{\partial u_m}{\partial x}\Big]&\\ =\rho_m a_m^2 C_1-a_m C_2&\end{aligned} \tag{4.72}$$

where

$$C_2 \equiv -\frac{\tau_{w,l}+\tau_{w,g}}{A} - \rho_m g \frac{dZ}{dx} \tag{4.73}$$

4.1.4 The characteristics and the compatibility relations

Eqn.(4.35,4.36,4.60,4.71,4.72) are the characteristic form of 1D EVUT Euler equations as below

$$\begin{aligned}
\frac{\partial p_m}{\partial t} + (u_m + a_m)\frac{\partial p_m}{\partial x} + \rho_m a_m \Big[\frac{\partial u_m}{\partial t} + (u_m + a_m)\frac{\partial u_m}{\partial x}\Big] \\
= \rho_m a_m^2 C_1 + a_m C_2 \\
\frac{\partial p_m}{\partial t} + (u_m - a_m)\frac{\partial p_m}{\partial x} - \rho_m a_m \Big[\frac{\partial u_m}{\partial t} + (u_m - a_m)\frac{\partial u_m}{\partial x}\Big] \\
= \rho_m a_m^2 C_1 - a_m C_2 \\
\Big[\frac{\partial \alpha}{\partial t} + u_m \frac{\partial \alpha}{\partial x}\Big] + \alpha(1-\alpha)\Big(\frac{1}{\rho_g a_g^2} - \frac{1}{\rho_l a_l^2}\Big)\Big[\frac{\partial p_m}{\partial t} + u_m \frac{\partial p_m}{\partial x}\Big] = C_3 \\
\frac{\partial h_g}{\partial t} + u_m \frac{\partial h_g}{\partial x} - \frac{1}{\rho_g}\Big(\frac{\partial p_m}{\partial t} + u_m \frac{\partial p_m}{\partial x}\Big) = C_4 \\
\frac{\partial h_l}{\partial t} + u_m \frac{\partial h_l}{\partial x} - \frac{1}{\rho_l}\Big(\frac{\partial p_m}{\partial t} + u_m \frac{\partial p_m}{\partial x}\Big) = C_5
\end{aligned} \tag{4.74}$$

where the C-coefficients C_i are given by

$$
\begin{aligned}
C_1 = &\quad \frac{m_{i,g}}{A}\Big(\frac{1}{\rho_g}-\frac{1}{\rho_l}\Big) - u_m\frac{1}{A}\frac{dA}{dx} - \frac{\alpha}{\rho_g}\frac{\partial\rho_g}{\partial h_g}C_4 - \frac{(1-\alpha)}{\rho_l}\frac{\partial\rho_l}{\partial h_l}C_5\\
C_2 = &\quad -\frac{\tau_{w,l}+\tau_{w,g}}{A} - \rho_m g\frac{dZ}{dx}\\
C_3 = &\quad \frac{\rho_m}{\rho_g\rho_l}\frac{m_{i,g}}{A} - \alpha(1-\alpha)\Big[\frac{1}{\rho_g}\frac{\partial\rho_g}{\partial h_g}C_4 - \frac{1}{\rho_l}\frac{\partial\rho_l}{\partial h_l}C_5\Big]\\
C_4 = &\quad \frac{q_{i,g}+q_{w,g}+\tau_{w,g}u_m}{\alpha\rho_g A}\\
C_5 = &\quad \frac{q_{i,l}+q_{w,l}+\tau_{w,l}u_m}{(1-\alpha)\rho_l A}
\end{aligned}
\tag{4.75}
$$

The reason for deriving the characteristic form of the EVUT Euler equations is that along the characteristics, the partial differential equations can be transformed into ordinary differential equations. According to (28), Eqn.(4.35,4.36,4.60,4.71,4.72) can be rewritten in the form of paired characteristics and compatibility relations, as

$$
\begin{aligned}
&C+: && dx=(u_m+a_m)dt;\ dp_m+\rho_m a_m du_m=(\rho_m a_m^2 C_1+a_m C_2)dt\\
&C-: && dx=(u_m-a_m)dt;\ dp_m-\rho_m a_m du_m=(\rho_m a_m^2 C_1-a_m C_2)dt\\
&PP: && dx=u_m dt; \qquad d\alpha-\alpha(1-\alpha)\Big[\frac{1}{\rho_l a_l^2}-\frac{1}{\rho_g a_g^2}\Big]dp_m=C_3 dt\\
&PP: && dx=u_m dt; \qquad dh_g-\frac{1}{\rho_g}dp_m=C_4 dt\\
&PP: && dx=u_m dt; \qquad dh_l-\frac{1}{\rho_l}dp_m=C_5 dt
\end{aligned}
\tag{4.76}
$$

in which the characteristics described by $u_m \pm a_m$ are called waves ($C+$ for $u_m + a_m$ and $C-$ for $u_m - a_m$) meaning the paths along which small-amplitude sound waves propagate and the characteristic described by u_m is called particle-path (PP) meaning the path along which a fluid particle (fluid particle here means a small control volume of fluid) moves.

The characteristics and the compatibility relations along them could be used to solve for the flow and fluid particle properties. We briefly introduce the basic idea of the method of characteristics as follows:

(i) Two different-type waves from two particles (one $C+$ from one; one $C-$ from the other) respectively will intersect at a point in $x-t$ plane. Along each wave, a certain compatibility relation between the pressure and the velocity must be satisfied, therefore at the intersection point, the pressure and the velocity must satisfy two compatibility relations simultaneously, which means a paired solution of (p_m, u_m) can be obtained from these two compatibility relations.

(ii) Along the particle-path, the ordinary differential equations can be integrated. Therefore given the initial and boundary conditions, the fluid particle properties could be solved for the upcoming moments.

Depending on the different way of dealing with the characteristics, different algorithms of the method of characteristics have been developed, i.e. the wave-tracing algorithm in (28) and the particle-path algorithm in (57) and (59). More detailed information will be given in the following chapters.

4.2 For single-phase flow

In the part of the domain occupied by air, the flow can be described as single-phase flow. Assuming the air flow is in isentropic condition, 1D conservative Euler equations for single-phase flow were given in (59) [1]

$$A\frac{\partial \rho_a}{\partial t}+\frac{\partial(A\rho_a u_a)}{\partial x} = 0 \tag{4.77}$$

$$A\frac{\partial}{\partial t}\left(\rho_a u_a\right)+\frac{\partial(A\rho_a u_a^2)}{\partial x}+A\frac{\partial p_a}{\partial x} = -\tau_{w,a} \tag{4.78}$$

$$\frac{\partial s_a}{\partial t}+u_a\frac{\partial s_a}{\partial x} = 0 \tag{4.79}$$

in which s is the entropy, given by $ds = dQ/T$. Using the differential chain rule and the definition of sonic speed as

[1] We rewrite those equations so that the wall friction force $\tau_{w,a}$ will have the same unit as in (28).

$$\begin{aligned}\frac{\partial p}{\partial t} &= \left(\frac{\partial \rho}{\partial p}\right)_s \frac{\partial p}{\partial t} + \left(\frac{\partial \rho}{\partial s}\right)_p \frac{\partial s}{\partial t} \\ a^{-2} &= \left(\frac{\partial \rho}{\partial p}\right)_s\end{aligned}$$

the corresponding characteristic forms can be derived as

$$\begin{aligned}\left[\frac{\partial p_a}{\partial t} + (u_a + a_a)\frac{\partial p_a}{\partial x}\right] + \rho_a a_a \left[\frac{\partial u_a}{\partial t} + (u_a + a_a)\frac{\partial u_a}{\partial x}\right] &= \rho_a a_a^2 C_6 + a_a C_7 \\ \left[\frac{\partial p_a}{\partial t} + (u_a - a_a)\frac{\partial p_a}{\partial x}\right] - \rho_a a_a \left[\frac{\partial u_a}{\partial t} + (u_a - a_a)\frac{\partial u_a}{\partial x}\right] &= \rho_a a_a^2 C_6 - a_a C_7 \quad (4.80) \\ \left[\frac{\partial \rho_a}{\partial t} + u_a \frac{\partial \rho_a}{\partial x}\right] - \frac{1}{a_a^2}\left[\frac{\partial p_a}{\partial t} + u_a \frac{\partial p_a}{\partial x}\right] &= 0\end{aligned}$$

where

$$\begin{aligned}C_6 &= -u_a \frac{1}{A}\frac{dA}{dx} \\ C_7 &= \frac{-\tau_{w,a}}{A}\end{aligned}$$

and the compatibility relations are

$$\begin{aligned}C+: \quad dx &= (u_a + a_a)dt;\ dp_a + \rho_a a_a du_a = (\rho_a a_a^2 C_6 + a_a C_6)dt \\ C-: \quad dx &= (u_a - a_a)dt;\ dp_a - \rho_a a_a du_a = (\rho_a a_a^2 C_7 - a_a C_7)dt \quad (4.81) \\ PP: \quad dx &= u_a dt;\ dp_a - a_a^2 d\rho_a = 0\end{aligned}$$

CHAPTER 5

THE PARTICLE-PATH ALGORITHM OF THE METHOD OF CHARACTERISTICS

In this chapter solution algorithms of the method of characteristics for solving the Euler equations are presented. In the previous chapter it has been shown that along the characteristics the partial differential equations are transformed into ordinary differential equations. Different solution algorithms exist for solving this set of ordinary differential equations. In the previous chapter we have already mentioned the particle-path algorithm of the method of characteristics (the PP-MOC algorithm), or briefly the particle-path algorithm. Here more details will be given and we also briefly discuss the fixed-mesh algorithm and the wave-tracing algorithm. In discussing the particle-path algorithm, we first present the generic case handling what happens in the bulk of the single phase region or the bulk of the two-phase region and next present the special cases needed to handle at the interface[1] between the single- and two-phase region, or at boundaries of the computational domain. Then we discuss the algorithm determining the discrete time step and finally present a small verification study.

[1]The exact name for this interface is 'the contact face', which will be further explained in this chapter.

5.1 The particle-path algorithm: the normal case

Consider a location in the bulk of either the single-phase or the two-phase region. Figure 5.1 shows the one-dimensional domain at two successive time steps t_0 and t_1. The figure also illustrates the particle-path algorithm to obtain the new pressure and velocity of a given particle. It exploits that certain compatibility relations must hold along the characteristics (wave or particle-path).

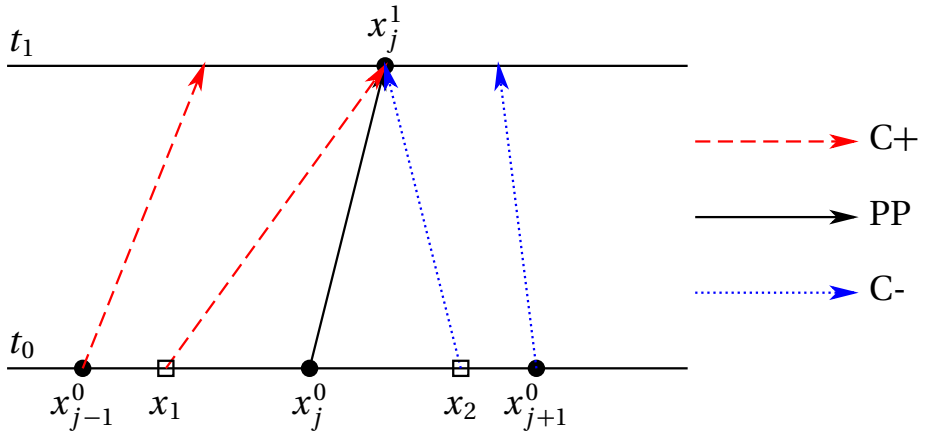

Figure 5.1: The particle-path algorithm: the normal case

With the known location, velocity of the particle x_j^0 (the subscript j denotes the $j-th$ particle in space and the superscripts 0 and 1 denote two successive moments in time, respectively) at the moment of t_0 and the time step Δt, its particle-path (PP) has been illustrated as the solid line as well as its new location x_j^1. Therefore once we find the corresponding C+ (illustrated as the dashed red line) and C- waves (illustrated as the dotted blue line) which reach x_j^1 at the moment of t_1, we will have two compatibility relations from the two characteristic waves respectively which could be used to solve for the new pressure and the new velocity at x_j^1.

According to (57) and (59), the particle-path algorithm of the method of characteristics is taking following steps.

1. Find the new location x_j^1 of the particle initially locates at x_j^0;

2. Use linear interpolation between the C+ waves from the particles at x_{j-1}^0 and x_j^0 to find the intersection point x_1 whose C+ wave will reach x_j^1 at the new moment t_1;

3. Use linear interpolation between the C- waves from the particles at x_j^0 and x_{j+1}^0 to find the other intersection point x_2 whose C- wave will reach x_j^1 at the new moment t_1;

4. Use the compatibility relations along those two characteristic waves to solve for the new pressure and velocity of the particle at x_j^1;

5. Use the known new pressure and velocity at x_j^1 to compute other properties along the particle-path from x_j^0 to x_j^1:

   - For the two-phase particle: the void fraction, the vapour enthalpy and the liquid enthalpy;
   - For the single-phase particle: the density.

6. Compute other auxiliary properties i.e. the sonic speeds, the interfacial heat and mass fluxes, the wall friction forces..., and finally obtain the new C-coefficients on the right hand side of the characteristic form of Euler equations at the new moment t_1;

7. Move on to the next time step.

5.2 The particle-path algorithm: the contact face

The interface between the mixture region and the air region is named the contact face in order to be distinguished from the interface between the liquid phase and the vapour phase in the two-phase mixture region. The particle-path algorithm for the pressure- and velocity-continuity conditions at the contact face will be explained. We further assume that no heat and mass exchange across the contact face is allowed just to simplify our problem.

Different from the normal case, the contact face in the particle-path algorithm is traced by two particles at one location in space, one at the mixture side of the contact face and the other at the air side of the contact face. For the contact face particles, the continuity conditions for pressure and velocity must be fully fulfilled.

Normally both the pressure and the velocity continuities must be satisfied at the contact face or mathematically

$$\begin{aligned} x_{CM} &= x_{CA} \\ u_{CM} &= u_{CA} \\ p_{CM} &= p_{CA} \end{aligned}$$

in which the subscript CM stands for the contact face/mixture side and the subscript CA stands for the contact face/air side.

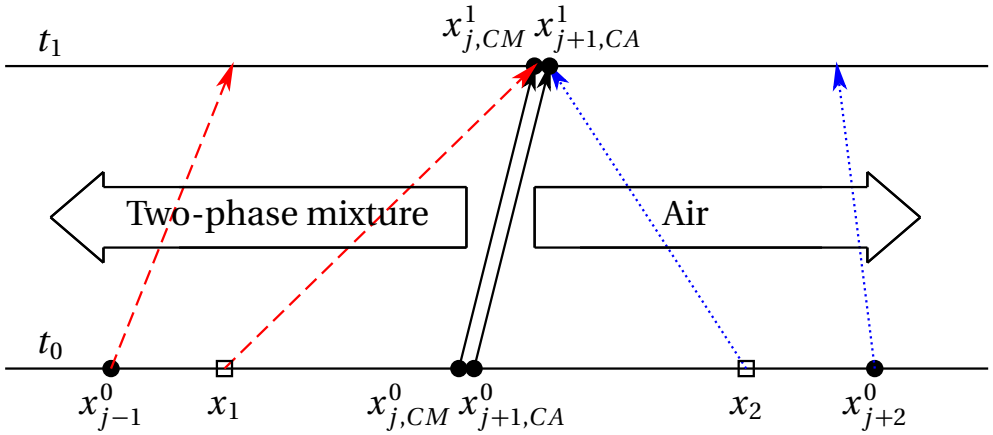

Figure 5.2: The particle-path algorithm: the contact face

For the two contact face particles $x^0_{j,CM}$ and $x^0_{j+1,CA}$, the C+ waves are both obtained from $(x^0_{j-1}, x^0_{j,CM})$ in the mixture region and the C- waves are both obtained from $(x^0_{j+1,CA}, x^0_{j+2})$ in the air region. See Fig.(5.2). In this way, the pressure and the velocity of the two contact face particles will be guaranteed to be identical all the time.

5.3 The particle-path algorithm: the inlet/outlet boundaries

In this section, the particle-path algorithm for the particles on the boundaries of the 1D computational domain or the inlet/outlet particles will be introduced. For these particles, the flow-dependent boundary conditions must be embedded into the particle-path algorithm, therefore the algorithm for these particles is different from the normal one. For convenience, we always assume the inlet is at the left end of the computational domain and the outlet is at the right end. The formulation of inlet and outlet boundary conditions is an example of the more general topic of boundary conditions for hyperbolic equations which will be discussed first.

5.3.1 The boundary value problem for hyperbolic equations

According to the nature of hyperbolic equations, the number of initial or boundary conditions must be equal to the number of characteristics which point into the computational domain. We will use the 1D unsteady single phase Euler equations to explain it.

The 1D unsteady Euler equations have three characteristics which are

$$\begin{aligned} C-: \frac{dx}{dt} &= u-a \\ PP: \frac{dx}{dt} &= u \\ C+: \frac{dx}{dt} &= u+a \end{aligned}$$

Now we will discuss the initial and boundary conditions in domain Ω in x,t-space which is a rectangular region given by $0 \leq x \leq L$ and $0 \leq t \leq t_0$, as indicated in Fig.(5.3). For convenient discussion, we suppose the velocity $u \geq 0$ on the boundaries of the domain Ω.

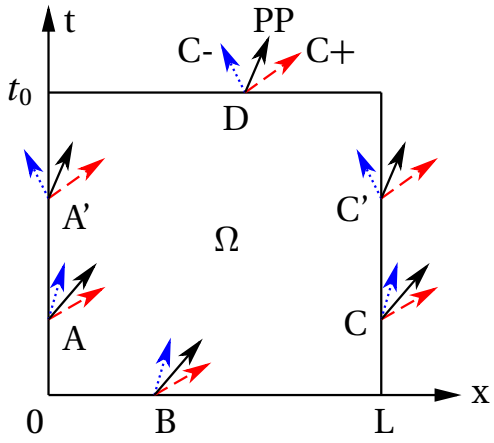

Figure 5.3: The initial boundary value problem for 1D unsteady Euler equations

1. If the flow on the boundary of $x = 0$ is supersonic ($u > a$) as point A indicates, all three characteristics at A are pointing into Ω, hence three boundary conditions are requested at $x = 0$. If the flow is subsonic ($u < a$) as point A' indicates and only C+ and PP are pointing into Ω, only two boundary conditions should be given.

2. For an arbitrary point B on $t = 0$, no matter the flow is supersonic or subsonic, all three characteristics are pointing into Ω, therefore three initial conditions are requested.

3. If the flow on the boundary of $x = L$ is again supersonic as point C indicates, all three characteristics are pointing outwards, hence no boundary conditions should be given at $x = L$. If the flow is subsonic as point C' indicates and only C- is pointing into Ω, only one boundary conditions should be given.

4. For an arbitrary point D on $t = t_0$, no matter the flow is supersonic or subsonic, all three characteristics are pointing outwards, therefore neither initial nor boundary conditions should be given at $t = t_0$.

5.3.2 The particle-path algorithm: the inlet

The particle-path algorithm for the inlet is illustrated in Fig.(5.4).

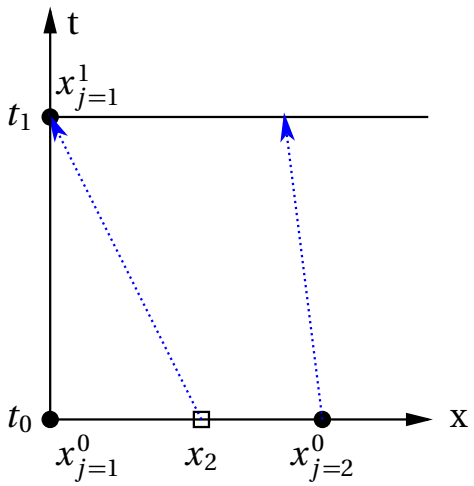

Figure 5.4: The particle-path algorithm: the inlet

If the inlet is closed, the boundary condition of zero velocity ($u = 0$) is given (one boundary condition since only one characteristic points into the computational domain from the boundary); if the inlet is open, depending on the local Mach number, two boundary conditions for the subsonic/sonic flow and three for the supersonic flow are needed respectively.

5.3.3 The particle-path algorithm: the outlet

The particle-path algorithm for the outlet is illustrated in Fig.(5.5).

If the flow at the outlet is subsonic ($u < a$) which means only C- wave ($u - a$) is pointing into the domain, the ambient pressure outside the tunnel will be used as the only boundary condition; if the flow at the outlet is sonic ($u = a$) or supersonic ($u > a$), no characteristics are pointing into the domain, therefore no boundary conditions are needed.

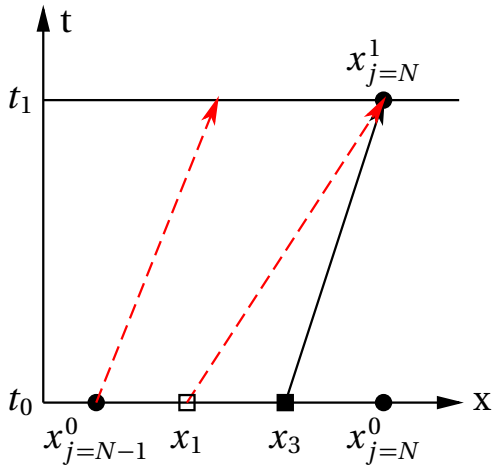

Figure 5.5: The particle-path algorithm: the outlet

5.4 The particle-path algorithm: mesh size and time step

Before we discuss the relation between the mesh size and the time step, we introduce two other algorithms of the method of characteristics, different from the particle-path algorithm discussed above. Those two algorithms have different mesh structures and differ in the way the time step is determined.

5.4.1 The fixed-mesh algorithm

In the fixed-mesh algorithm, the mesh points are fixed in space and time. Besides the two points x_1 and x_2, origin of the $C+$ and $C-$ waves, also the origin of the PP x_3 is found by linear interpolation. See Fig.(5.6).

The advantage of the fixed-mesh algorithm is the simplicity of the mesh; the disadvantage of the fixed-mesh algorithm is that for unsteady flow three interpolations are requested per mesh point per time step, therefore it is time-consuming and relatively inaccurate. The fixed-mesh algorithm is suitable for steady flows in which the mesh points are not necessarily moving.

In the fixed-mesh algorithm, the necessary relation between the mesh size and the time step, or so-called stability criterion is given as

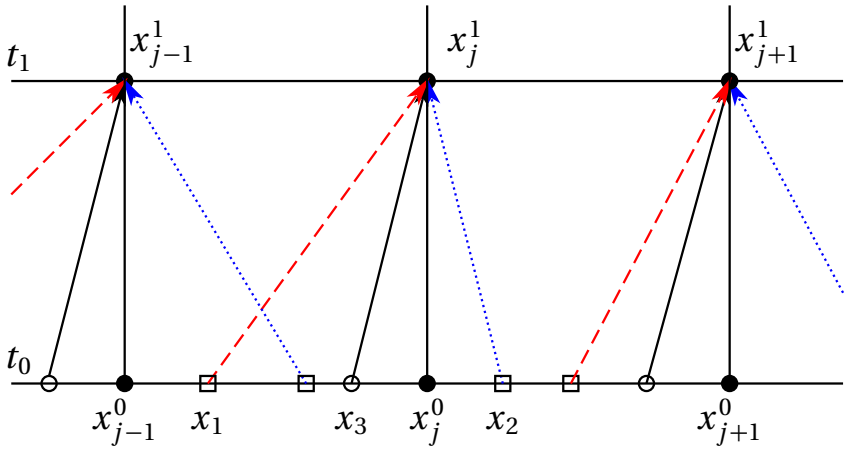

Figure 5.6: The fixed-mesh algorithm

$$\frac{\Delta x}{\Delta t} \geq max|u+a| \qquad \text{or} \qquad \Delta t \leq \frac{\Delta x}{max|u+a|}$$

5.4.2 The wave-tracing algorithm

In the wave-tracing algorithm the local time step is chosen that the two C+ and C- waves from two 'neighboring' mesh points intersect with each other exactly after that time step. The interpolation for obtaining x_1 and x_2, the origins of C+ and C- wave respectively, is skipped. But now the interpolation is applied to obtain x_3, the origin of the new mesh point. See Fig.(5.7).

The advantages of the wave-tracing algorithm include i) relatively higher accuracy in computation; ii) implicit mechanism for determining time-step. The disadvantages of it include i) difficult for coding, especially at the boundaries; ii) interpolation error generated in demonstrating computational results at one moment. The reader could find more detailed information about the wave-tracing algorithm of the method of characteristics in (28).

In the wave-tracing algorithm, local time step is calculated as part of the algorithm itself. In other words, the algorithm always chooses the maximum possible time step for one mesh point, hence it is most efficient in time marching. Since the local

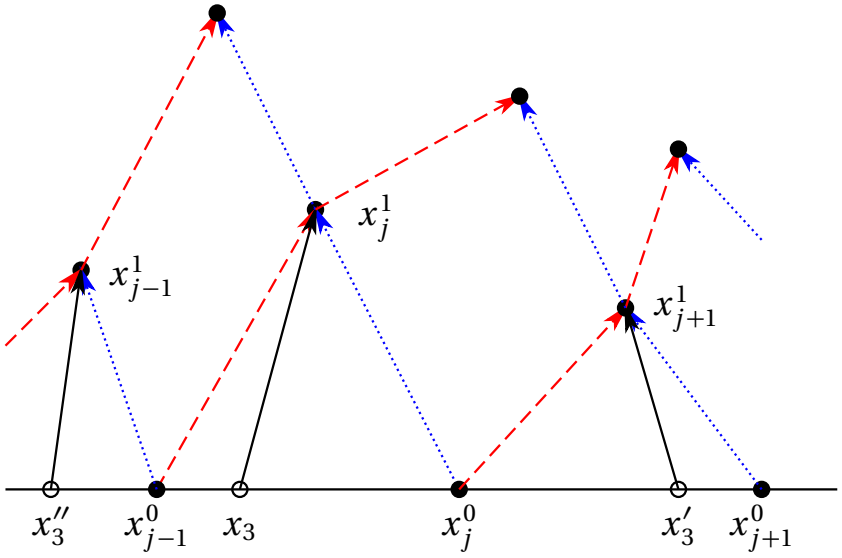

Figure 5.7: The wave-tracing algorithm

maximum time step is in general not a constant throughout the domain, the interpolation is used to obtain the property distribution at certain moments, however the error in interpolation will not influence the solution.

5.4.3 Global maximum time step

The particle-path algorithm can start with uniform or non-uniform mesh as long as the time step is properly chosen to ensure the intersection points x_1 and x_2 for the particle at x_j are located in the two intervals constituted by the three particles at x_{j-1}, x_j and x_{j+1} respectively as

$$x_{j-1} \leq \quad x_1 \quad \leq x_j$$

$$x_j \leq \quad x_2 \quad \leq x_{j+1}$$

The distance between two neighboring particles in the particle-path algorithm, in general, is varying in time, so for each time step, we have to compare the charac-

teristics of every particle with the ones of its neighbors to find the local maximum time step and further choose the minimum out of all the local maximum time steps as the global maximum time step. The applicable time step for the computation must not exceed the global maximum time step.

$\Delta t_{j,+}^{max}$, the local maximum time step for $j-th$ particle from $C+$ wave intersection that ensures x_1, the intersection point as the origin of the C+ wave, locates between x_{j-1} and x_j, is given as

$$\begin{aligned} \Delta t_{j,+}^{max} &\rightarrow +\infty \quad \text{if } (C+)_{j-1} \leq u_j \\ \Delta t_{j,+}^{max} &= \frac{x_j - x_{j-1}}{(C+)_{j-1} - u_j} \quad \text{if } (C+)_{j-1} > u_j \end{aligned}$$

Similarly $\Delta t_{j,-}^{max}$, the local maximum time step for $j-th$ particle from $C-$ wave intersection that ensures x_2, the intersection point as the origin of the C- wave, locates between x_j and x_{j+1}, is given as

$$\begin{aligned} \Delta t_{j,-}^{max} &\rightarrow +\infty \quad \text{if } (C-)_{j+1} \geq u_j \\ \Delta t_{j,-}^{max} &= \frac{x_{j+1} - x_j}{u_j - (C-)_{j+1}} \quad \text{if } (C-)_{j+1} < u_j \end{aligned}$$

The applicable time step Δt and the global maximum time step are given as

$$\Delta t \leq \Delta t^{max} = min\left[min(\Delta t_{1,+}^{max}, \ldots, \Delta t_{N,+}^{max}), min(\Delta t_{1,-}^{max}, \ldots, \Delta t_{N,-}^{max})\right]$$

in which N is the total number of the particles in the computational domain.

It is possible to determine whether the local maximum time steps are finite or infinite. If taking $\Delta t_{j,+}^{max}$ for example, we have

$$a_j > 0 \Rightarrow (C+)_j > u_j$$

If $(C+)_{j-1} \leq u_j$, below inequality holds

$$(C+)_{j-1} \leq u_j < (C+)_j$$

Linear interpolation between $(C+)_{j-1}$ and $(C+)_j$ can always provide an intersection point x_1 to the left of x_j^0 whose $C+$ can catch up with the particle at x_j^0 for arbitrary time step, or in other words, the algorithm is unconditional stable. See Fig.(5.8).

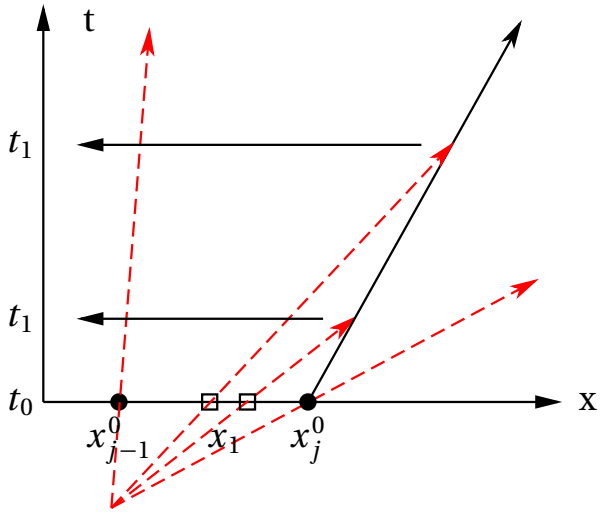

Figure 5.8: Infinite local maximum time step

If $(C+)_{j-1} > u_j$, no matter whether $(C+)_{j-1} > (C+)_{j-1}$ or $(C+)_{j-1} \leq (C+)_{j-1}$, a finite local maximum time step is given.

1. Case 1: $(C+)_{j-1} > (C+)_j > u_j$, see Fig.(5.9);

2. Case 2: $(C+)_j \geq (C+)_{j-1} > u_j$, see Fig.(5.10).

For $\Delta t_{j,-}^{max}$ obtained from the intersection of the $C-_{j+1}$ and u_j, similar conclusions can be drawn as well.

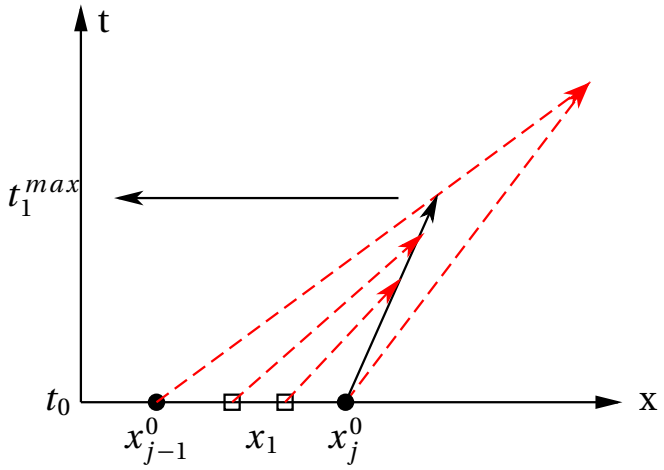

Figure 5.9: Finite local maximum time step: Case 1

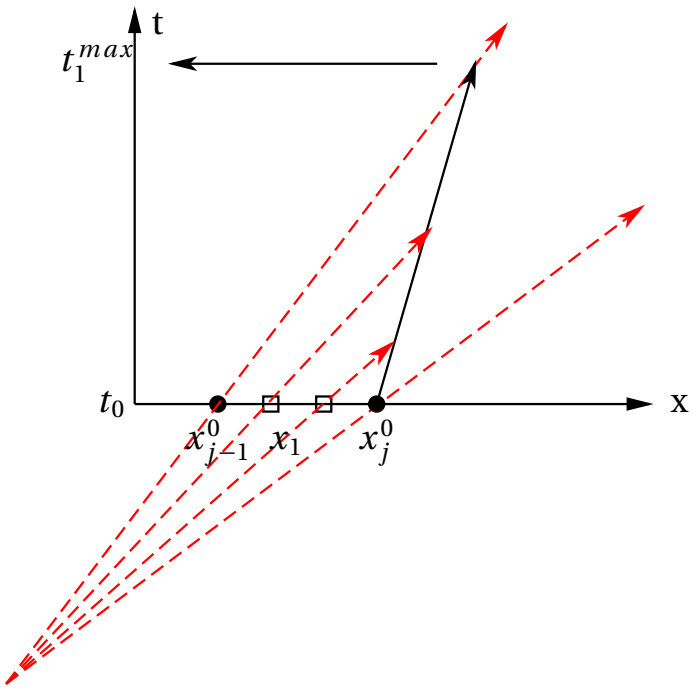

Figure 5.10: Finite local maximum time step: Case 2

5.5 Explicit shock tracing method in the particle-path algorithm

In (57) and (59), Pinhasi et al. proposed a shock tracing method based on the particle-path algorithm to explicitly generate and capture shocks. See Fig.(5.11 5.12 and 5.13). When the C+ waves from two neighboring particles intersect, a shock will be generated. Similarly to the particle-path algorithm for the contact face, two particles have been placed at the shock location, one with the properties of the fluid ahead of the shock, namely the shock head particle and one with the properties of the fluid just behind the shock, namely the shock tail particle. Their properties are related by the shock relation. Like the pressure-velocity-continuity must hold for the contact face particles, the shock relation must hold for the shock particles, therefore in Fig.(5.13), the particle marked by 3 has a new velocity (see the bending of its particle-path) after the shock particles pass by. Detailed information can be found in (57) and (59).

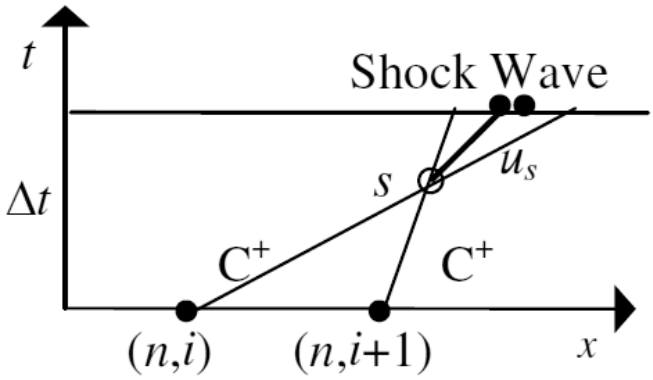

Figure 5.11: Wave diagrams of formation of the shock. Reproduced from (57).

The explicit shock tracing method proposed by Pinhasi et al. has been applied in our initial studies. However, this method has been criticized for being valid for weak shocks only. It suffers from a deficiency. Namely, the shock propagation needs a known shock speed u_s, and once this speed is given by the shock generation method, it does not change in the following computations, and therefore can not handle an accelerating shock.

Therefore in subsequent work we did not use an explicit shock tracing method,

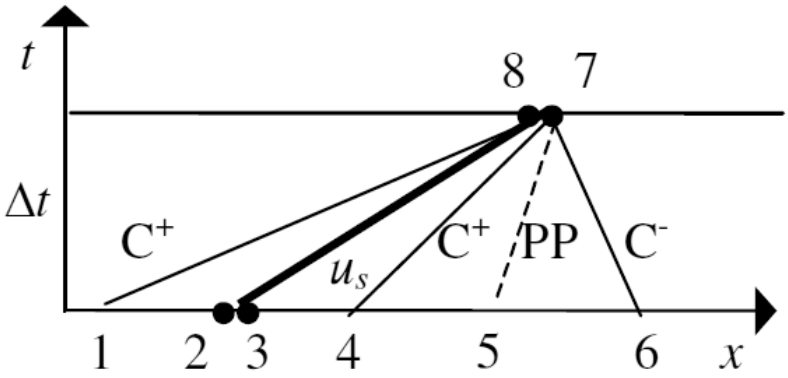

Figure 5.12: Wave diagram for problem involving shock-wave. Reproduced from (57).

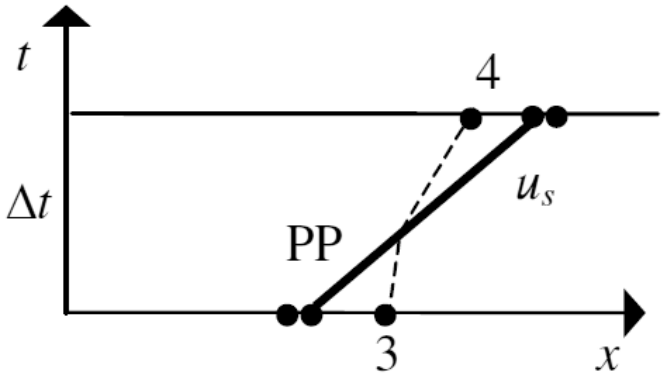

Figure 5.13: Wave diagrams of particle passing the shock. Reproduced from (57).

but just allow the particle-path algorithm to represent the shock as sharp increase in a spacial interval rather than a jump in pressure, velocity and density profiles at one location. We made several observations from our computations without explicit shock tracing method:

1. In the model simulation of the BLEVE development a spacial interval with steep slope gradually develops in the air region;

2. This steep slope feature, as traced by several particles, could propagate at a speed higher than the local sonic speed of the undisturbed air ahead;

3. The shape of the slope, once fully developed, maintains its shape quite well during its propagation.

In fact, as confirmed by Pinhasi (private communication), the explicit shock tracing method is only developed for replacing the numerically diffused shock (a slope over a spacial interval) with a neat jump (a discontinuity at one specific location). The difference between using only the particle-path algorithm and adding the explicit shock tracing method is that the particle-path algorithm only gives a space interval in which the fluid properties change rapidly and a shock is expected and the explicit shock tracing method proposed by Pinhasi et al. gives an exact location where the fluid properties jump.

As a conclusion, in all results to be presented below, explicit shock tracing has not been used. All the particles, except the particles on the contact face and the inlet/outlet, are treated equally no matter whether they are on a sharp slope representing a shock or at rest.

5.6 Verification of the particle-path algorithm

In this section, we will carry out the verification of the particle-path algorithm with a standard numerical test. Although the author of (58) has already carried out the verification of the particle-path algorithm, it is still very important and valuable for us to do it by ourselves, not only as the verification for the algorithm but also as a double-check of our Fortran code.

5.6.1 The Riemann problem and the Sod's test case

The standard test case used in this section as the benchmark for our code is based on the exact solution of the Riemann problem. We first introduce the Riemann problem and the Sod's test case.

According to (87), the Riemann problem is a special Initial Value Problem as illustrated by Fig.(5.14). The initial profile has a discontinuity at $x = 0$ between two piecewise constant states $\mathbf{u}_L$ and $\mathbf{u}_R$.

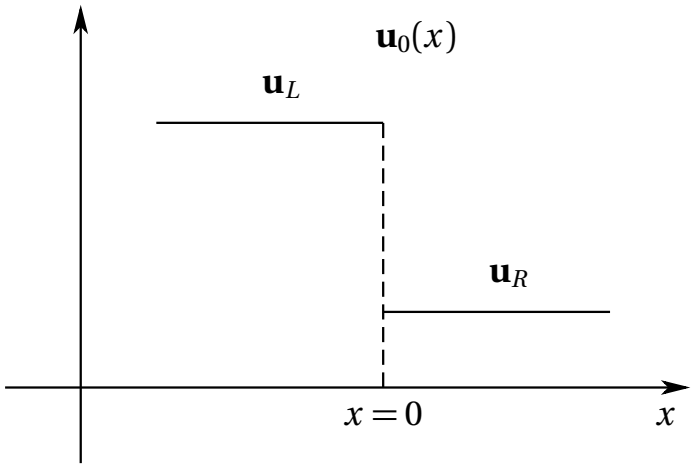

Figure 5.14: Illustration of the initial data for the Riemann problem. At the initial time the data consists of two constant states separated by a discontinuity at x = 0

$$\mathbf{u}(x,0)=\mathbf{u}_0(x)\begin{cases}\mathbf{u}_L & \text{if } x<0,\\ \mathbf{u}_R & \text{if } x>0.\end{cases}$$

More detailed information on the Riemann problem can be found in Chpt.(2,4) of (87).

In the review work (82), Sod used one Riemann problem as the test case for several numerical algorithms and compared the outputs. Later on, this particular Riemann problem was named as Sod's test case bearing the author's name and widely used as a standard test case for the solution algorithms for hyperbolic equations. The exact non-dimensional values of the Sod's test case are given as

	d	p	u	γ
Left	1	1	0	1.4
Right	0.125	0.1	0	1.4

The Riemann problem can have different solutions for different hyperbolic equations as well as different equations of state. In Chpt.(4) of (87), the exact solution of the Riemann problem for the standard Euler equations (no source terms)

with ideal gas equation of state has been provided by a Fortran code namely HE-ElRPEXACT. Therefore we need to use the same equation of state and eliminate all the source terms in our TUDelft code accordingly in order to use the output of HE-ElRPEXACT as the benchmark.

5.6.2 Verification on the coarse mesh

100 uniformly distributed nodes/particles have been used in the computations by HE-ElRPEXACT and by our code leading to an initial uniform mesh size (particle distance) of $0.01m$. The profile after $0.5ms$ has been computed and the pressure, velocity and density spatial profiles from two different codes have been compared in Fig.(5.15, 5.16, 5.17).

Despite of some error in capturing the two ends of the rarefaction wave propagating to the left, the matching of the results are satisfactory even compared with the results given in (82).

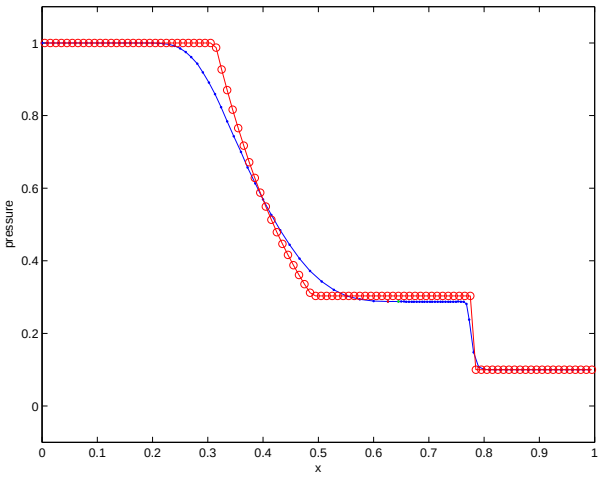

Figure 5.15: Pressure profile at 0.5ms, coarse mesh, red circled line: exact solution; blue dotted line: the particle-path algorithm

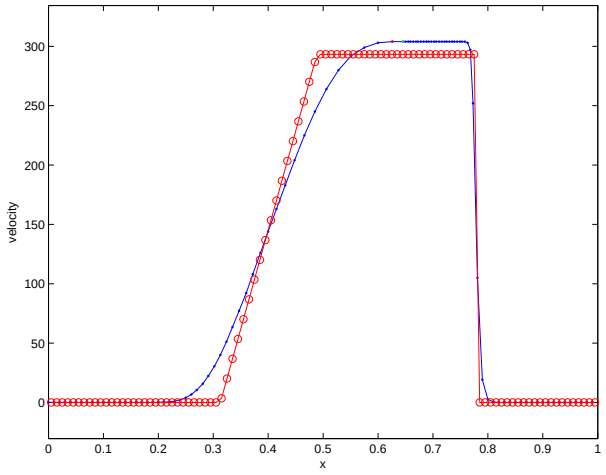

Figure 5.16: Velocity profile at 0.5ms, coarse mesh, red circled line: exact solution; blue dotted line: the particle-path algorithm

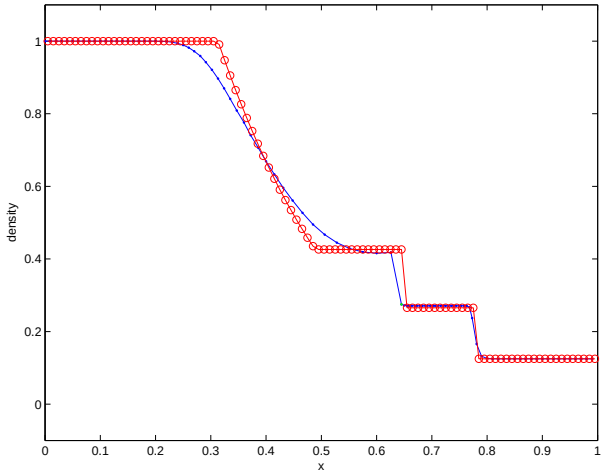

Figure 5.17: Density profile at 0.5ms, coarse mesh, red circled line: exact solution; blue dotted line: the particle-path algorithm

5.6.3 Verification on a finer mesh

Subsequently we tested whether better accuracy is obtained on a finer mesh. By increasing the total number of nodes/particles by a factor ten an initial uniform mesh size (particle distance) of $0.001\,m$ was used. The results are shown in Fig.(5.18) and Fig.(5.19).

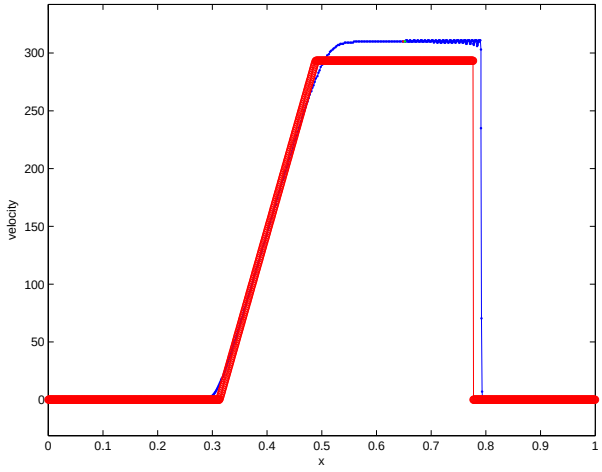

Figure 5.18: Velocity profile at 0.5ms, finer mesh, red circled line: exact solution; blue dotted line: the particle-path algorithm

It is clearly observed that the two ends of the rarefaction wave are better captured due to the lower numerical diffusion on the finer mesh. However, the wiggles near the shock front have increased indicating numerical instability has increased.

5.6.4 Conclusions on the particle-path algorithm verification

The following conclusions can be drawn from the verification of the particle-path algorithm:

1. The generation and propagation of the rarefaction wave and the shock wave can be clearly observed in the solutions, therefore the particle-path algorithm is applicable for our BLEVE simulation;

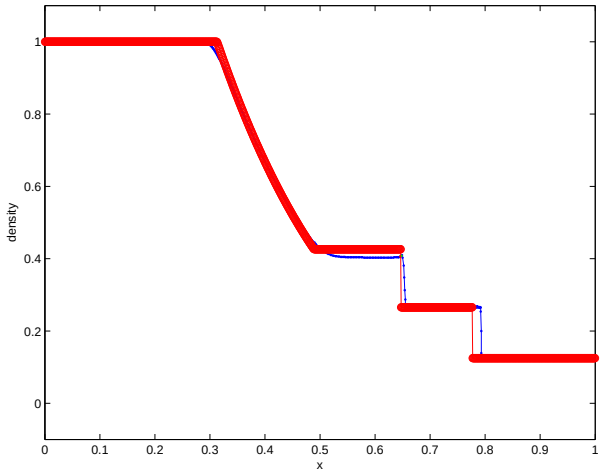

Figure 5.19: Density profile at 0.5ms, finer mesh, red circled line: exact solution; blue dotted line: the particle-path algorithm

2. The predictions of the magnitudes of profile jumps by the particle-path algorithm is acceptable in accuracy;

3. The errors in the prediction of the locations of the profile jumps is clearly visible but still acceptable because the prediction of the magnitudes is more important than the prediction of the locations for the problem of BLEVE simulation;

4. It has been demonstrated that there is a trade-off between the numerical diffusion and the numerical instability;

The particle-path algorithm for a problem with a contact face between a two-phase region and a single phase region is not essentially different from the particle-path algorithm used in the solution of Sod's test case. Therefore the verification in the case of Sod's test case can be considered sufficient to conclude that the particle-path algorithm is adequate for solving the 1D BLEVE problem. Indeed, the main uncertainty in the overall quality of model predictions from the EVUT model will come not only from the numerical algorithm, but also from the physical models of phase transition.

CHAPTER 6

SOURCE TERM MODELING

The source terms in two-phase EVUT Euler equations and single-phase Euler equations can be categorized into three groups

1. Interfacial fluxes[1], including the interfacial heat flux terms $q_{i,k}$ and the interfacial mass flux terms $m_{i,k}$.

2. Wall source terms, including the wall friction terms $\tau_{w,k}, \tau_{w,a}$ and the wall heat flux terms $q_{w,k}, q_{w,a}$;

3. Tunnel geometry source terms, including the cross-sectional area variation term $\frac{1}{A}\frac{dA}{dx}$ and the inclination term $\frac{dZ}{dx}$;

In this chapter, most emphasis has been put on the interfacial fluxes. Both a qualitative model and a quantitative model for these source terms are presented. The qualitative model is relative simple and robust while the quantitative models is rather complex. In order to present it in a systematic way the explanation is bottom-up from basic process to overall features, from the generation of the interface, via the evolution of the interface, and the closed model for interfacial fluxes.

[1]The interface here represents the interface between liquid PLG and vapour PLG in the two-phase region when a BLEVE occurs.

On the other hand, in the present application to 1D BLEVE development, the wall and tunnel geometry terms can be kept very simple. This is explained in the final section of this chapter. In the case of the single phase Euler equations the interfacial source terms vanish but the wall source terms and tunnel geometry source terms could remain.

6.1 Qualitative interfacial fluxes model: the relaxation time model

The relaxation time model is a qualitatively correct, robust and compact model for the interfacial fluxes. The basic underlying assumption of the relaxation time model is that the process of return-to-equilibrium has a constant relaxation time. R.L. Ferch proposed this model in (28). However as the researcher mentioned, the assumption of constant relaxation time is not made because of the correctness of the model, but because of its simplicity in application. The formulas of the relaxation time model are

$$q_{i,k} = \alpha_k(1-\alpha_k)A\rho_k(h_{k,sat}-h_k)/t_{i,k} \tag{6.1}$$

$$m_{i,g} = -m_{i,l} = -(q_{i,g}+q_{i,l})/(h_g-h_l) \tag{6.2}$$

in which $t_{i,k}$ is the relaxation time for phase k and A is the cross-sectional area of the tunnel.

It is clear that, in Eqn.(6.1), $\alpha_k(1-\alpha_k)A$ is an estimate of the interfacial area density A_i[2] and $\rho_k(h_{k,sat}-h_k)/t_{i,k}$ is the interfacial heat transfer term in which $(h_{k,sat}-h_k)$ describes the potential that drives the phase k back to its saturated state. Furthermore, Eqn.(6.2) describes that both the energy and the mass are conserved at the interface between phases since it can be derived into

$$\begin{aligned} m_{i,g}+m_{i,l} &= 0 \\ (m_{i,g}h_g+q_{i,g})+(m_{i,l}h_l+q_{i,l}) &= 0 \end{aligned}$$

[2]It is unnecessary to include a proportionality factor in the formula because the relaxation time is an parameter that can be set to any assumed value.

and those two relations must hold for any interfacial flux models developed under the equal-velocity assumption between phases.

As the computations in Chpt.(8) will demonstrate, the relaxation time model is capable of demonstrating all the relevant phenomena involved in a BLEVE of PLG:

- the rapid pressure drop that triggers a BLEVE;
- the propagation of the rarefaction wave into the undisturbed PLG liquid;
- the pressure recovery due to the phase transition from the liquid to the vapour;
- the expansion of the two-phase mixture;
- the formation and the propagation of a shock in the air.

However, our objective is to give predictions on the hazard caused by a BLEVE, and for that purpose quantitative models are needed as discussed next.

6.2 Quantitative interfacial fluxes model

The uncertainties in the relaxation time model mainly come from

1. the lack of information on the relaxation time $t_{i,k}$;
2. the lack of information on the initial void fraction α_g^0;
3. the inaccuracy in the estimation of the interfacial area $A_i \propto \alpha_k(1-\alpha_k)A$.

Correspondingly, for the quantitative interfacial fluxes model, we prefer to

1. avoid using free parameters e.g. $t_{i,k}$ in the interfacial fluxes and if the model is not closed, use reasonable assumptions;
2. establish a bubble nucleation model which can use the local instantaneous flow variables to estimate the initial void fraction when the criteria for the bubble nucleation are fulfilled. This part of work belongs to the category of interface generation;

3. build up an interfacial area evolution model which, with reasonable assumptions, uses the void fraction evolution and the bubble status to estimate the interfacial area.

Considering that during a BLEVE the liquid state will probably approach the region in phase space close to the kinecit superheat limit, which is far away from the equilibrium state, we cannot only rely on equilibrium thermodynamics but have to refer to non-equilibrium thermodynamics, a theoretical framework in which both the deviation from and the return to the equilibrium state can be described.

This section is arranged in a bottom-up manner, starting from the bubble nucleation model, then the interfacial area evolution model and finally the interfacial fluxes model.

6.2.1 Interfacial area generation: bubble nucleation

To mathematically describe the bubble nucleation, we must know

1. at which thermodynamic states, bubbles will start to form in PLG liquid;
2. when the bubble are formed, what are the states of the liquid surrounding and the vapour inside the bubbles.

Therefore the target of this section is to find the relationship between (i) the KSL i.e. T^{KSL} or p^{KSL} at which critical bubbles form; (ii) the critical bubble nucleation rate J_{cbn}, the critical bubble radius r^* and (iii) the thermodynamic properties of the vapour insides the critical bubbles and the liquid states surrounding the critical bubbles during or after the nucleation process. This is the subject of homogeneous nucleation theory.

Homogeneous nucleation theory

Homogeneous nucleation is still an active topic of research. The homogeneous nucleation theory, developed to describe all three phase transitions (condensation: vapour-to-liquid; cavitation: liquid-to-vapour and crystallisation: liquid-to-solid) involving single-component fluids (54), has already been extended to multi-

component systems (38). In our research on BLEVE, the application of homogeneous nucleation theory only concerns homogeneous bubble nucleation in a superheated liquid due to rapid depressurisation, which means we limit the discussion to the case of cavitation. It will become clear that this limitation will help us to choose the most useful form of homogeneous nucleation theory, instead of the most advanced one.

According to (23), the first homogeneous nucleation theory, namely the classical nucleation theory (CNT), was originally developed by Volmer and Weber in (97) and in the late 1970s, Katz and his colleagues started to challenge CNT on its assumption of equilibrium distribution of vapour embryo's in their works (40) (39) and (98). As a result, they proposed a new theory, kinetic nucleation theory (KNT). Later on, with the help of computers, non-classical methods, e.g. the density functional method and the molecular dynamics simulation, have been applied and more and more non-classical phenomena have been found seriously challenging the classical nucleation theory (24).

The homogeneous nucleation theory for cavitation aims to answer two questions:

1. At what threshold, vapour embryos will appear and grow spontaneously?

2. What will be the rate of generation of the vapour embryo's once the homogeneous nucleation starts?

The first question refers to the kinetic superheat limit and the second question refers to the critical bubble nucleation rate. To give a proper estimation of the bubble nucleation rate, the liquid state surrounding the embryo and the vapour inside the embryo must be estimated in advance.

In (7), Avedisian summarised various experimental techniques for the research on homogeneous nucleation of liquids, including pulse heating method, capillary tube method, bulb method, isobaric droplet heating and isothermal decompression methods, which can be categorized into isobaric heating technique and isothermal decompression technique altogether. More importantly, Avedisian discussed the nucleation rates obtained with different techniques and gave the conclusion that different techniques will result in different ranges of the nucleation rate. For floating droplet and capillary tube methods, the following equations were proposed to estimate the nucleation rates

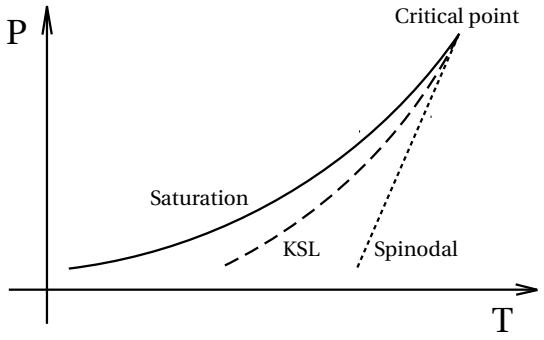

Figure 6.1: p-T diagram showing the critical point, the saturation curve, the kinetic superheat limit and the spinodal curve

$$J_{cbn} \simeq \frac{G_T \dot{T}}{V} \quad \text{for isobaric heating} \tag{6.3}$$

$$J_{cbn} \simeq \frac{G_T \dot{p}}{V} \frac{dT}{dp_0} \quad \text{for isothermal decompression} \tag{6.4}$$

in which G_T is the derivative of the Gibbs free energy to the temperature, which is approximately constant over the experimental temperature interval; $\dot{T}$ is the temperature increase rate and $\dot{p}$ is the decompression rate. p_0 is the initial pressure of the test liquid and V is the volume of the test liquid.

When isobaric heating is applied to the capillary tube method, the nucleation rate in the mentioned range of temperature change rate and volume is given by

$$\begin{aligned} 0.01 < \dot{T} &< 3\,[K/s] \\ 0.01 < V &< 0.1\,[cm^3] \\ 1 < J_{cbn} &< 10^3\,[1/(cm^3\,s)] \end{aligned}$$

When isothermal decompression is applied to the capillary tube method, the nuc-

leation rate in the mentioned range of depressurisation and volume is given by

$$\begin{aligned} \dot{p} &\simeq 1.01\,[MPa/s] \\ dT/dp_0 &\simeq 0.5\,[K/MPa] \\ 0.005 < V &< 0.15\,[cm^3] \\ 10 < J_{cbn} &< 10^3\,[1/(cm^3\,s)] \end{aligned}$$

When isobaric heating is applied to floating droplet methods, the nucleation rate in the mentioned range of temperature change rate and volume is given by

$$\begin{aligned} 0.03 < \dot{T} &< 50\,[K/s] \\ 10^{-7} < V &< 10^{-4}\,[cm^3] \\ 100 < J_{cbn} &< 10^8\,[1/(cm^3\,s)] \end{aligned}$$

Pulse heating method gives a range of nucleation rate as $10^{15} < J_{cbn} < 10^{22}\,[1/(cm^3\,s)]$.

Above discussions reveal one thing, the capabilities of different techniques that bring the liquid into superheated state are different. The technique that can bring the liquid to the highest superheat state is always excellent in i) depressing the heterogeneous nucleation; ii) maintaining the stability of the liquid during the heating or the decompressing. For the same technique, the smaller the volume of the experimental liquid is, the higher the liquid can be superheated either by isobaric heating or by isothermal decompression, the higher the superheat limit temperature (or the lower the superheat limit pressure) will be.

From this point of view, the target of the research on homogeneous nucleation of the liquid becomes different from the one of our BLEVE research. The former aims at bring the liquid to a higher superheated level resulting a larger bubble nucleation rate, therefore breaking the record of the superheat limit, with the aim of proposing a new homogeneous nucleation theory or modifying an old one. The latter aims at the probable superheat limit and the probable bubble nucleation rate that can happen during a BLEVE. If all the non-classical phenomena can only be observed under a circumstance that will not occur in a real BLEVE, the nucleation theory that can explain those non-classical phenomena means nothing to our research and maybe CNT, the origin of the nucleation theory proposed far before the scientists put great efforts to increase the superheat limit or more obviously increase the bubble nucleation rate by manipulating a small-volume liquid, will be

the most suitable nucleation theory for our BLEVE research. Detailed quantitative discussions will be given in the following sections.

The classical nucleation theory

The classical nucleation theory was based on determination of the minimum work required to form a vapour bubble in the bulk of homogeneous liquid at constant temperature from the capillarity approximation[3] as in (24)

$$W_{min} = \sigma A_b - (p_g - p_l)V_b + i(\mu_g - \mu_l) \tag{6.5}$$

where σ is the surface tension; A_b is the surface area of the bubble; p_g is the pressure within the bubble; p_l is the surrounding liquid pressure; V_b is the volume of the bubble; i is the number of molecules inside the bubble and μ_g and μ_l are the chemical potentials of the vapour and liquid phases, respectively. As shown in Fig.(6.2), the minimum work of formation W_{min} has a maximum, W^*_{min}, which naturally forms an energy barrier for the bubble clusters or nuclei to grow up because

- for a bubble nucleus with radius less than the critical bubble radius r^*, further growth requests more and more work of formation which it has to take in from the surrounding liquid. Hence the possibility of shrinking for that nucleus is higher than the possibility of expansion, and it will probably disappear;
- for a bubble nucleus with radius larger than the critical bubble radius r^*, further growth requests less and less work of formation which it has to take in from the surrounding liquid. Hence the possibility of expansion for that bubble is higher than the possibility of shrinking, and it will probably grow.

It was assumed that the number of bubbles per unit volume, namely the bubble number density, is related exponentially to the minimum work W_{min} required to form the bubbles (12)

[3]The capillarity approximation is the assumption that the critical nucleus surface tension equals the surface tension of a flat interface„ which means the influence of the surface curvature on the surface tension has bee neglected.

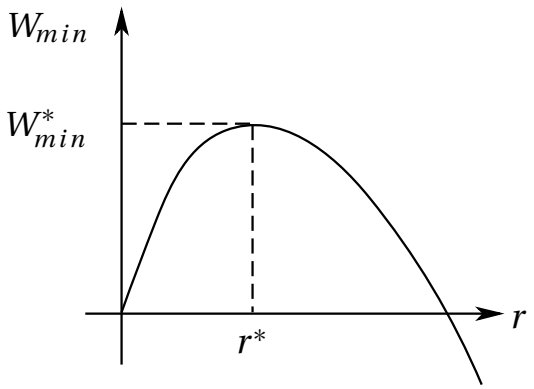

Figure 6.2: The minimum work of formation of bubble clusters W_{min}, the radius of the critical bubbles r^* and the nucleation barrier W^*_{min}.

$$n_b = \mathbb{N}\exp\Big(-\frac{W_{min}}{\mathbb{K}T_l}\Big) \tag{6.6}$$

where $\mathbb{K}$ is the Boltzmann constant; n_b is the number density of bubbles; the prefactor $\mathbb{N}$ is the number density of liquid molecules. If the critical bubbles in the nucleation process are considered, their steady-state nucleation rate J_{cbn} is given by (24)

$$J_{cbn} = J_0\exp\Big(-\frac{W^*_{min}}{\mathbb{K}T_l}\Big) \tag{6.7}$$

The presence of the exponential factor in Eqn.(6.6,6.7) is most important, and the influence of errors in the prefactors is not crucial. Therefore the classical nucleation theory is capable of predicting the kinetic superheat limit successfully by properly choosing the bubble nucleation rate. When Blander and Katz published their work in 1975, they reported that the measured superheat limits for a large amount of pure components agree with predictions from the classical nucleation theory (12).

However as the research proceeds, the classical nucleation theory has been widely criticized for underestimating the critical bubble nucleation rate compared with the results by other approaches. In 2003, Delale et al. introduced a new phe-

nomenological model to decrease the nucleation barrier W^*_{min} (24). As a result, the nucleation rate was predicted to be higher, namely of order $10^{26} \sim 10^{32} m^{-3} s^{-1}$, or equivalently $10^{20} \sim 10^{26} cm^{-3} s^{-1}$, which is much higher than the prediction of $10^4 \sim 10^6 cm^{-3} s^{-1}$ in (12). On the other hand, the classical nucleation theory has not been criticized for underestimating the superheat limit, or in other words, ever since 1975, the predicted superheat limit has not been increased so much compared to the bubble nucleation rate. The reason is that at the experimental level of the 1970s, heterogeneous nucleation has been sufficiently suppressed in the superheat limit research by using purified liquids and smooth vessels, in order for the superheat limits measured in those experiments to be quite close the the stability limit of the liquid where a small increase in the liquid temperature δT will result in exponentially increase in the bubble nucleation rate. Another reason is that, compared to the measurement of the bubble nucleation rate, the time window to observe or measure δT is too small for the temperature measuring instruments.

Hence, the prediction of the superheat limit by the classical nucleation theory is as reliable as the ones from other state-of-art theories. As found in our computations, the underestimation of the bubble nucleation rate by the classical nucleation theory will result in overestimation on the shock strength possibly generated by a BLEVE. Before reaching that conclusion, we have to introduce the classical nucleation theory in detail.

Bubble nucleation: the Delale et al. 2003 model

The classical theory of homogeneous bubble nucleation has been criticized in predicting low nucleation rate. Therefore Delale et al. (24) improved it by proposing a phenomenological term to decrease the nucleation barrier in the capillarity approximation. They derive the following relation between the temperature and the pressure at the kinetic superheat limit

$$p^{KSL}_{l,r} = p_{g,sat,r}(T_l)\Big[1 - \frac{\kappa_D}{\delta}\frac{(1-T_{l,r})^{\tau_D}}{T_{l,r}}\Big(\frac{\Delta H_{vap}}{\mathbb{R}T_c\Delta\mathbb{Z}}\Big)\Big(1 - \frac{\mathbb{Z}_{l,sat}}{\mathbb{Z}_{g,sat}}\Big)\Big] \tag{6.8}$$

Here κ_D is a substance dependent constant; and the constant $\tau_D \sim 2.2$.

*

According to (24), $p_{g,sat,r}(T_l)$ and the normalised latent heat $\Delta H_{vap}/(\mathbb{R}T_c\Delta\mathbb{Z})$ are given by the Wagner equation (70) as

$$p_{g,sat,r}(T_l) = exp\Big[\frac{a\chi+b\chi^{1.5}+c\chi^3+d\chi^6}{1-x}\Big] \tag{6.9}$$

$$\Delta H_{vap}/(\mathbb{R}T_c\Delta\mathbb{Z}) = -a+b\chi^{0.5}(0.5\chi-1.5)+c\chi^2(2\chi-3)+d\chi^5(5\chi-6) \tag{6.10}$$

in which $\chi = 1-T_{l,r}$. The substance dependent coefficients a, b, c, and d are given in (51) for 250 fluids.

* *

$\mathbb{Z}_{g,sat}$ and $\mathbb{Z}_{l,sat}$ are the saturated compressibility factors of the liquid and the vapour at T_l respectively, which can be solved from the SRK-EOS as

$$\mathbb{Z}^3-\mathbb{Z}^2+(A^*-B^*+B^{*2})\mathbb{Z}-A^*B^*=0 \tag{6.11}$$

in which[4]

$$A^* = \frac{0.42748p_r}{(T_{l,r})^2}\Big[1+\mathbf{f}\omega(1-\sqrt{T_{l,r}})\Big]^2$$

$$B^* = \frac{0.08664p_r}{T_{l,r}}$$

$$\mathbf{f}\omega = 0.48+1.574\omega-0.176\omega^2\sim 0.48$$

when $p_r = p_{g,sat}(T_l)/p_c$ and $T_{l,r} = T_l/T_c$ is the reduced liquid temperature.

According to (69), the p-T diagram of the SRK-EOS can be separated in two regions depending on the number of real roots: the single-real-root region and the three-real-root region. See Fig.(6.3). Solving Eqn.(6.11) for the saturated compressibilities of a given temperature will guarantee the solution containing three real roots including $\mathbb{Z}_{g,sat}$ and $\mathbb{Z}_{l,sat}$. It should be noted that in the three-root-region, the largest real root corresponds to the vapour and the smallest one corresponds to the liquid.

[4]The terms containing the acentric factor ω were neglected in (24).

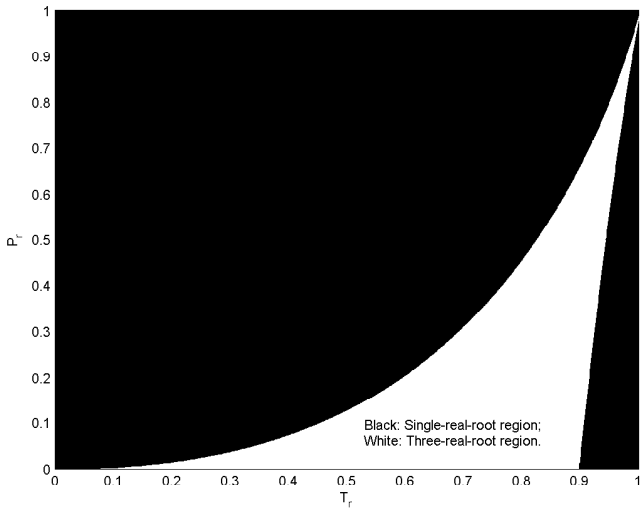

Figure 6.3: Number of real roots of the Soave-Redlich-Kwong EOS as function of reduced temperature and pressure

* * *

The equilibrium vapour pressure p_e, also called the saturated pressure $p_{g,sat}$, refers to the pressure when the liquid and the vapour are saturated and the interface between them is hydrostatic and of zero-curvature. At $[p_e(T_l), T_l]$, the liquid and the vapour have the same chemical potential, which is normally used to solve for p_e when a temperature is given. However the metastable liquid of temperature T_l is at a pressure less than $p_e(T_l)$, which means the chemical potential of the metastable liquid is less than the saturated liquid at the same temperature ($d\mu = VdP$), the vapour pressure p_g of the metastable fluid must be less than p_e to assure that the liquid and the vapour have the same chemical potential. The Poynting correction factor

$$\delta = 1 - \frac{\rho_{g,sat}(T_l)}{\rho_l} + \frac{1}{2}\Big(\frac{\rho_{g,sat}(T_l)}{\rho_l}\Big)^2 \tag{6.12}$$

is introduced so that the actual pressure difference across the interface between

the liquid and the vapour $(p_g - p_l)$ can be estimated from the liquid temperature T_l and its equilibrium vapour pressure, p_e or $p_{g,sat}(T_l)$ as

$$p_g - p_l = \delta \Big[p_{g,sat}(T_l) - p_l \Big] \tag{6.13}$$

As a result, with the help of an EOS (e.g. SRK-EOS in (24)), Eqn.(6.8) for the kinetic superheat limit is closed. For a given liquid temperature T_l, a kinetic superheat limit pressure p_l^{KSL} can be solved and vice versa:

$$\begin{aligned} p_l^{KSL} &= f(T_l) \\ T_l^{KSL} &= f(p_l) \end{aligned}$$

The radius of the critical bubble is given as

$$r^* = \frac{2\sigma}{p_g - p_l} = \frac{2\sigma}{\delta[p_{g,sat}(T_l) - p_l]} \tag{6.14}$$

in which $p_l = p_l^{KSL}(T_l)$ and the surface tension σ of nonpolar liquids is given in (69) as

$$\sigma = p_c^{2/3} T_c^{1/3} \mathbb{Q}[1 - T_{l,r}]^{11/9} \tag{6.15}$$

where

$$\mathbb{Q} = 0.1196 \Big[1 + \frac{T_{sat,r}(p_{1atm}) \ln(p_c/p_{1atm})}{1 - T_{sat,r}(p_{1atm})} \Big] - 0.279 \tag{6.16}$$

in which p_{1atm} is one standard atmosphere. It should be noted that the prefactor 0.196 in the same equation in (24) is a misprint. The critical nucleation rate J_{cbn} is given as

$$J_{cbn} = \mathbb{Z}_{g,sat} \Big(\frac{3\sigma\rho_l^2}{\pi m_1^3} \Big)^{1/2} \exp \Big[- \frac{4\pi r^{*2}\sigma}{3\mathbb{K}T_l} (1 - 2\alpha_s) \Big] \tag{6.17}$$

in which α_s is equal to 1/3 for most substances and 7/16 for water and m_1 is the mass of one single molecule.

Modifications of the Delale et al. 2003 model

The Delale et al. 2003 model is clear and closed, but the equation of state they used is different from the one selected for our BLEVE investigation. In order to consistently use one equation of state in the model for the BLEVE simulation, it is necessary to replace the SRK-EOS by the PRSV-EOS in the Delale et al. 2003 model. Therefore these two equations of state have to be compared with respect to the calculation of the relevant properties of the kinetic superheat limit and corresponding liquid and vapour properties.

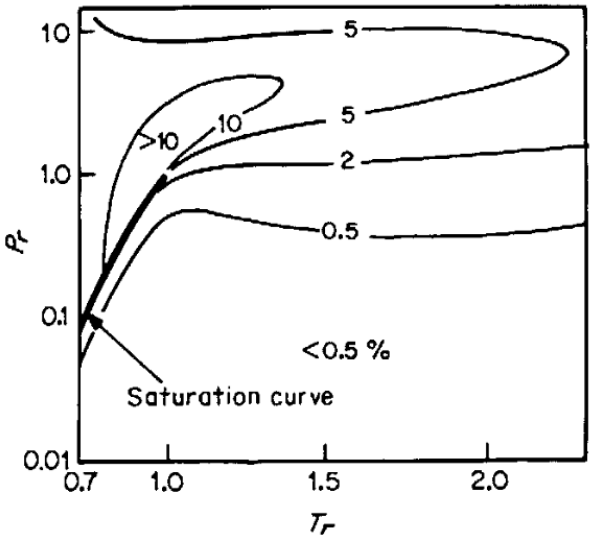

Figure 6.4: Percent error in molar volume calculated for CO_2 by using the RK-EOS with Soave parameters, reproduced from (69)

Fig.(6.4) from (69) demonstrates the percent error of the SRK-EOS in predicting the liquid molar volume from the experimental data. Fig.(6.5) from (84) demonstrates the percent deviation of the PRSV-EOS in predicting the saturated liquid molar volumes. When Fig.(6.4) and (6.5) are compared, the conclusion can be easily drawn that the SRK-EOS and the PRSV-EOS are at the same level in predicting the liquid molar volume or the liquid density[5].

[5]The cubic equations of state are generally poor in predicting the liquid density, hence only the liquid densities are checked when the improvements are carried out.

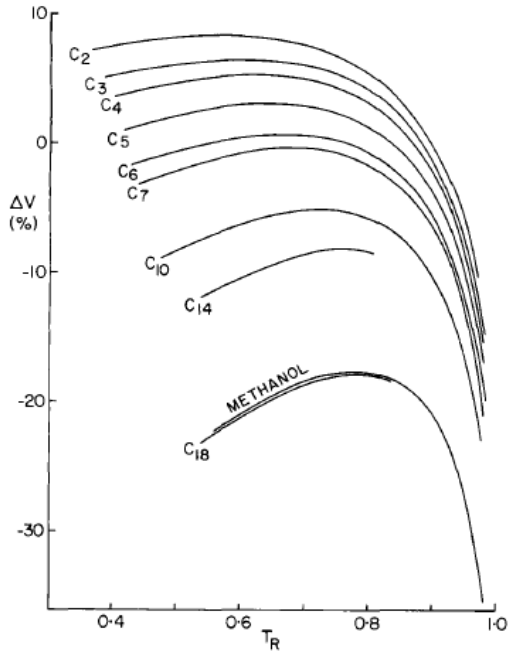

Figure 6.5: Percent deviations in liquid molar volumes at saturation calculated with the PRSV-EOS (C_n, represents the alkane C_nH_{2n+2}), reproduced from (84)

On the other hand, Delale et al. also simplified $\mathbf{f}\omega$ in Eqn.(6.11). In Tab.(6.1), the predictions from three equations of state are compared with the data from the gas encyclopedia of Air Liquide (http://encyclopedia.airliquide.com). As can be seen, simplifying $\mathbf{f}\omega$ gives the largest error and the largest percent deviation in ρ_l from the PRSV-EOS matches Fig.(6.5).

When the PRSV-EOS is introduced into the Delale et al. 2003 model, as Fig.(6.6) shows, it gives a lower kinetic superheat limit pressure than the one from the SRK-EOS and the difference is acceptable. A similar conclusion can be drawn for the critical bubble radius in Fig.(6.7). When critical bubbles become smaller, it is reasonable to have higher critical bubble nucleation rate in Fig.(6.8) and again the deviation is acceptable.

In conclusion we can say, i) it is improper to simplify $\mathbf{f}\omega$ in the SRK-EOS; ii) replacing the SRK-EOS with the PRSV-EOS does not introduce unacceptable error into

Table 6.1: Percent deviation in predicting the liquid density of propane at $1\,atm$

Propane	p (bar)	T_{sat} (K)	T^r_{sat}	ρ_l (kg/m^3)	Perc. dev. in ρ_l
Air Liquide Gas Encyclopedia	1.013	231.05	0.6248	582.00	-
SRK-EOS + Wagner equation $\mathbf{f}\omega = 0.48$	1.013	231.00	0.6246	533.03	8.41%
SRK-EOS + Wagner equation $\mathbf{f}\omega = 0.48 + 1.574\omega - 0.176\omega^2$	1.013	231.00	0.6246	550.26	5.45%
PRSV-EOS	1.013	231.24	0.6246	621.73	6.82%

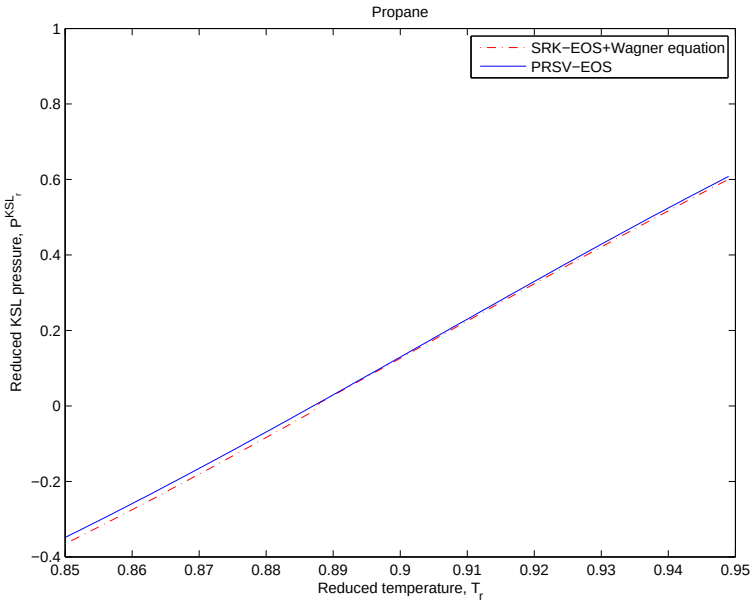

Figure 6.6: Kinetic superheat limit pressure predicted by the Delale et al. 2003 model with the SRK-EOS and the PRSV-EOS

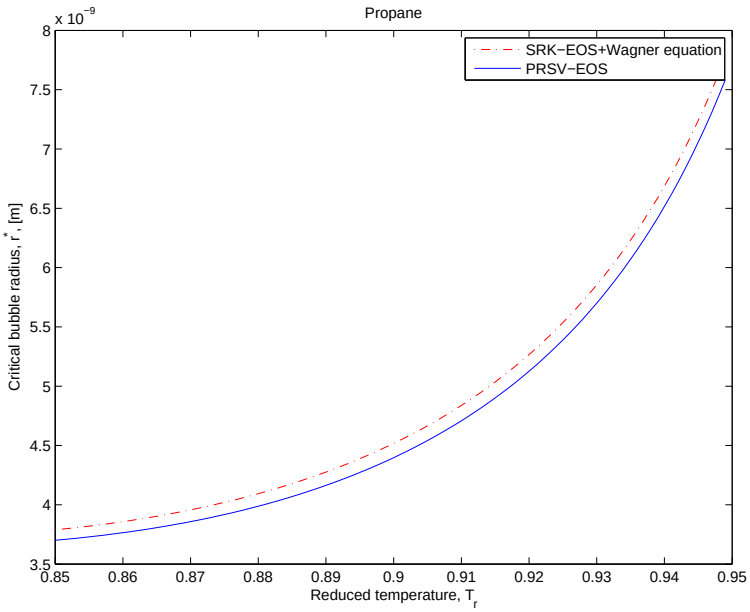

Figure 6.7: Critical bubble radius predicted by the Delale et al. 2003 model with the SRK-EOS and the PRSV-EOS

the calculations. Therefore the PRSV-EOS already available in the modified StanMix of FluidProp, will be used in the construction of the interfacial source term models.

Application of the bubble nucleation model

The Delale et al. 2003 model forms a complete system to predict the kinetic superheat limit, the nucleation rate of the critical bubbles and the properties of the liquid surrounding and the vapour inside the critical bubbles. The nucleation theory aims at predicting the KSL and the critical bubble nucleation rate at the KSL. But in our BLEVE simulation, the depressurisation process will not automatically stop at the KSL, which means that the bubbles nucleated at the KSL can also grow due to further depressurisation.

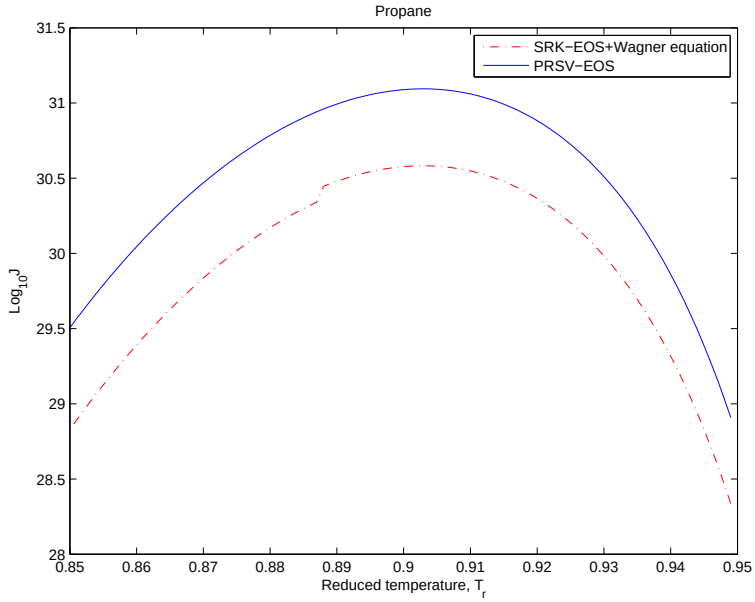

Figure 6.8: Critical bubble nucleation rate predicted by the Delale et al. 2003 model with with the SRK-EOS and the PRSV-EOS

If we want to introduce the nucleation model into our model, the PLG region must be initially in a single-phase state, which means that not the EVUT Euler equations, but the standard single-phase Euler equations have to be used for the air region as well as for the PLG region. After the computation begins, when some PLG particles cross the kinetic superheat limit due to depressurisation, the nucleation model will be activated and transform this single-phase particle into a two-phase particle. From that moment on, the EVUT Euler equations, in stead of the standard single-phase Euler equations, will be solved using these particles.

The numerical algorithm to implement the bubble nucleation model into the BLEVE simulation is illustrated in Fig.(6.9). At certain moment t_i, a PLG particle $L0$ having the pressure $p_{l,0}$ and the specific volume $v_{l,0}$ is represented by the open circle in the p-v-T diagram. It is obvious that $L0$ is above the KSL. At the following moment t_{i+1}, the state of the particle moves from $L0$ to $M2$ which is represented by the black dot and below the KSL. Because the particle has crossed the KSL during the depressurisation process, the PLG particle at $M2$ has become a two-phase

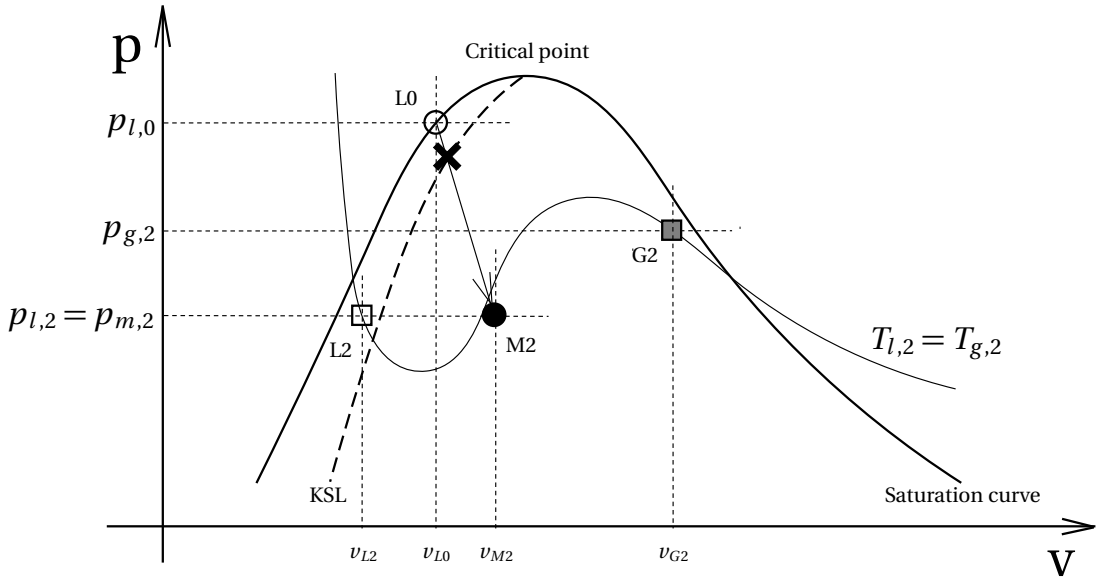

Figure 6.9: Sketch of the action of the bubble nucleation model in the p-v-T diagram

particle with the pressure $p_{m,2}$ and the specific volume $v_{m,2}$. This two-phase mixture particle consists of the liquid located at $L2$ (open square) and the vapour located at $V2$ (gray square). In this process, the liquid particle $L0$, after one time step, becomes a two-phase mixture $M2$ containing the liquid $L2$ and the vapour $V2$ due to depressurisation and bubble nucleation.

The pressure and the specific volume of the two-phase mixture $M2$ are known, but several assumptions and/or simplifications must be made to assure the closure of the estimation on the properties of the liquid and the vapour inside the two-phase mixture at the time t_{i+1}.

1. The liquid pressure is very close to the two-phase mixture pressure, i.e. $p_{l,2} \simeq p_{m,2}$;

2. The liquid and the vapour have the same temperature, $T_{g,2} = T_{l,2} = T_2$ and are in equilibrium with each other;

3. The expansion work in the depressurisation process for the bubble nucleation can be neglected according to the calculations;

4. The nucleated bubbles are all spherical and evenly distributed within the volume of one mixture particle;

The mass balance equation at t_{i+1} gives

$$\rho_{m,2} = \alpha\rho_{g,2} + (1-\alpha)\rho_{l,2} \tag{6.18}$$

and the energy balance

$$\rho_{l,0}h_{l,0} - \Delta W = \alpha\rho_{g,2}h_{g,2} + (1-\alpha)\rho_{l,2}h_{l,2} + \sigma 4\pi r_b^2 n_b \tag{6.19}$$

in which r_b is the radius of the spherical bubbles and n_b is the number density of the bubbles. Neglecting the expansion work ΔW and assuming the bubbles are all spherical

$$\begin{aligned} \Delta W &\sim 0 \\ 4\pi r_b^2 n_b &= 3\alpha/r_b \end{aligned}$$

the energy equation becomes

$$\rho_{l,0}h_{l,0} = \alpha\rho_{g,2}h_{g,2} + (1-\alpha)\rho_{l,2}h_{l,2} + 3\sigma\alpha/r_b \tag{6.20}$$

in which the unknowns are α, $\rho_{l,2}$, $\rho_{g,2}$, $h_{l,2}$, $h_{g,2}$, σ and r_b. They are obtained by

$$\begin{aligned} \rho_{l,2} &= EOS(p_{l,2}, T_2) \\ h_{l,2} &= EOS(p_{l,2}, T_2) \\ \rho_{g,2} &= EOS(p_{g,2}, T_2) \\ h_{g,2} &= EOS(p_{g,2}, T_2) \\ \sigma &= f(T_2) \quad \text{See Eqn.(6.15)} \\ r_b &= f(p_{l,2}, \sigma, \delta) \quad \text{See Eqn.(6.14)} \\ \delta &= f(p_{l,2}, T_2) \quad \text{See Eqn.(6.12)} \\ p_{g,2} &= f(\delta, p_{l,2}, T_2) \quad \text{See Eqn.(6.9)} \end{aligned}$$

where *EOS* denotes use of an equation of state and in this thesis means use of the PRSV-EOS in the modified StanMix. With above assumptions, seven unknowns can be reduced to two unknowns as T_2 and α, and then it is possible to obtain them by a numerical solution method, e.g. trial-and-error method.

6.2.2 Interfacial area evolution: from bubbles to droplets

Once critical bubbles have nucleated, further vapourisation would prefer to occur at their interface in response to temperature and/or pressure gradients rather than form new bubbles because the energy barriers for bubble nuclei to grow up have been overcome in existing bubbles and vapourisation through existing interfaces becomes easier. When a large amount of nuclei have been formed, the vapourisation by bubble growth soon become the dominant contributor to phase change. Via the phase change and the accompanying temperature and pressure changes, the system evolves to an equilibrium state, subject to prevailing, possibly time-dependent boundary conditions.

The interfacial flux models are developed to describe how the liquid with large numbers of bubbles will react to the temperature change and the pressure change and they are normally formulated in terms of the interfacial area density A_i. However, the current EVUT-Euler equations formulated in previous chapters solve for the volume fraction of the vapour α_g (or the liquid α_l). Therefore in order to use the interfacial flux models in the frame of the Euler equations the relationship between volume fraction α_g and interfacial area density A_i must be known. The interface fluxes can be transformed from an amount 'per m^2 of the interface' to an amount 'per m^3 of the mixture volume' once the interfacial area density A_i is given.

Interfacial area density and Sauter mean diameter

The area density of the interface A_i between liquid and gas in the volume of V_m is defined as

$$A_i = \frac{A_{int}}{V_m} \tag{6.21}$$

where A_{int} is the interfacial area. It can also be written as

$$A_i = \alpha_g \frac{A_{int}}{V_g} = \alpha_l \frac{A_{int}}{V_l} \tag{6.22}$$

The value of the interface area density depends on the structure of the two phase medium. Extreme cases are formed by the situations of disconnected bubbles in a liquid continuum and disconnected droplets in a gaseous continuum. In general the bubbles or droplets will have different sizes, as characterized by a size distribution. The simplest case is the case of mono-sized distribution.

In the case of bubbles in liquid continuum the interface area and volume of gas phase are given by

$$A_{int} = \sum_{i=1}^{N_b} \pi \phi_{b,i}^2 \qquad V_g = \sum_{i=1}^{N_b} \frac{\pi}{6} \phi_{b,i}^3 \tag{6.23}$$

where N_b is the total number of bubbles and $\phi_{b,i}$ refers to the diameter of the i^{th} bubble. In the case of droplets in gaseous continuum the interface are an the volume of the liquid phase are given by

$$A_{int} = \sum_{i=1}^{N_d} \pi \phi_{d,i}^2 \qquad V_l = \sum_{i=1}^{N_d} \frac{\pi}{6} \phi_{d,i}^3 \tag{6.24}$$

where N_d is the total number of droplets and $\phi_{d,i}$ refers to the diameter of the i^{th} droplet.

At this point it is useful to introduce the Sauter mean diameter (SMD). By definition this is the diameter of a bubble/droplet which has the same volume to surface ratio as the total collection of bubbles/droplets.

$$\phi_{SMD,b} = \frac{6V_g}{A_{int}} = \frac{\sum_{i=1}^{N_b} \phi_{b,i}^3}{\sum_{i=1}^{N_b} \phi_{b,i}^2} \qquad \phi_{SMD,d} = \frac{6V_l}{A_{int}} = \frac{\sum_{i=1}^{N_d} \phi_{d,i}^3}{\sum_{i=1}^{N_d} \phi_{d,i}^2} \tag{6.25}$$

Consequently in the two limiting cases the interface area density is given by

$$A_i = \frac{6\alpha_g}{\phi_{SMD,b}} \quad A_i = \frac{6\alpha_l}{\phi_{SMD,d}} \tag{6.26}$$

In order to express the interface area density A_i as a function of the volume fraction, it is necessary to express the Sauter mean diameter as function of the volume fraction. This can only be done after making further assumptions on the evolution

of bubble/droplet number. In general, it is useful to introduce the bubble number density and the droplet number density, as the number of bubbles or droplets in a given diameter range per unit volume of the mixture $n_b(\phi_b)$ and $n_d(\phi_d)$

$$\frac{N_b^{total}}{V_m} \equiv n_b^{total} = \int_0^\infty n_b(\phi_b)d(\phi_b) \quad \frac{N_d^{total}}{V_m} \equiv n_d^{total} = \int_0^\infty n_d(\phi_d)d(\phi_d) \tag{6.27}$$

The volume fraction and the Sauter mean diameter can be obtained from the moments of the distribution. A general quotient of two moments is defined as

$$\phi_{b,mn} = \frac{\int_0^\infty (\phi_b)^m n_b(\phi_b)d(\phi_b)}{\int_0^\infty (\phi_b)^n n_b(\phi_b)d(\phi_b)} \tag{6.28}$$

and in the case of bubbles in liquid continuum

$$SMD_b = \phi_{b,32} \tag{6.29}$$

$$\alpha_g = \int_0^\infty \frac{\pi}{6}\phi_b^3 n_b(\phi_b)d(\phi_b) = \frac{\pi}{6}\phi_{b,30} n_b^{total} \tag{6.30}$$

$$A_i = \int_0^\infty \pi\phi_b^2 n_b(\phi_b)d(\phi_b) = \pi\phi_{b,20} n_b^{total} \tag{6.31}$$

the relationship between the interfacial area density and the vapour volume fraction is given as

$$A_i = 6\alpha_g \frac{\phi_{b,20}}{\phi_{b,30}} = \frac{6\alpha_g}{\phi_{b,32}} \tag{6.32}$$

For every size distribution, the relation between $\phi_{b,30}$ and $\phi_{b,20}$ can be found and it may be possible to find the ratio of $\phi_{b,30}$ and $\phi_{b,20}$. On the other hand if $\phi_{b,20}$ and n_b^{total} can both be expressed in terms of known quantities, we also have an expression for the interface area density.

Evolution of interfacial area density

Let us consider first the situation where the total number of bubbles is constant in time (or in the case of droplets in gas, that the total number of droplets is constant

in time). This situation occurs when nucleation, and breakup and coalescence phenomena are absent. The fact that the total number of bubbles or droplets is constant in time does not imply that the number density is constant because the volume containing a given number of bubbles or droplets can change under the influence of vapourisation or pressure changes.

Consider a liquid with 'infinitely small bubbles' initially contained in an initial volume V_{ini} and with initial density

$$\rho_{ini} = \alpha_{g,ini}\rho_{g,ini} + \alpha_{l,ini}\rho_{l,ini} \tag{6.33}$$

where the subscript ini denotes the initial state. The initial bubble number density and initial bubble size distribution are related to the assumed initial gas volume fraction by

$$\alpha_{g,ini} = \frac{\pi}{6}\phi_{b,30,ini}\, n_{b,ini}^{total} \tag{6.34}$$

The initial bubble number density must be chosen such that above equation is satisfied, but there are many possibilities. In the case of mono-sized initial size distribution

$$\phi_{b,30,ini} = \phi_{b,ini}^3 \tag{6.35}$$

therefore

$$\phi_{b,ini} = \phi_{b,32,ini} = \Big[\frac{6}{\pi}\frac{\alpha_{g,ini}}{n_{b,ini}^{total}}\Big]^{1/3} \tag{6.36}$$

And the initial interface area density is

$$A_{i,ini} = \frac{6\alpha_{g,ini}}{\phi_{b,ini}} = 6\alpha_{g,ini}\Big[\frac{6}{\pi}\frac{\alpha_{g,ini}}{n_{b,ini}^{total}}\Big]^{-1/3} \tag{6.37}$$

When vapourisation proceeds, as a reaction to pressure built up in the bubbles, it will expand to reach a volume $V_g + V_l$, such that mass is conserved

$$\rho_{ini} V_{ini} = \rho_g V_g + \rho_l V_l \tag{6.38}$$

$$\rho_{ini}\frac{V_{ini}}{V_g + V_l} = \rho_g\frac{V_g}{V_g + V_l} + \rho_l\frac{V_l}{V_g + V_l} = \rho_g\alpha_g + \alpha_l\rho_l = \rho_m \tag{6.39}$$

Here V_g, V_l and ρ_m are time-dependent. If the volume increases from V_{ini} to V_g+V_l with the number of bubbles unchanged, the number of bubbles per unit volume will decrease by the inverse factor

$$n_{b,ini}^{total}(t) = n_{b,ini}^{total}(t_{ini}) \frac{V_{ini}}{V_g(t)+V_l(t)} = n_{b,ini}^{total}(t_{ini}) \frac{\rho_m(t)}{\rho_{ini}} \tag{6.40}$$

Substituting Eqn.(6.40) into Eqn.(6.30, 6.31), one finds

$$\alpha_g(t) = \frac{\pi}{6} \phi_{b,30}(t) n_{b,ini}^{total}(t_{ini}) \frac{\rho_m(t)}{\rho_{ini}} \tag{6.41}$$

$$A_i(t) = \pi \phi_{b,20}(t) n_{b,ini}^{total}(t_{ini}) \frac{\rho_m(t)}{\rho_{ini}} \tag{6.42}$$

Dividing Eqn.(6.42) by Eqn.(6.41) one finds again

$$A_i = 6\alpha_g \frac{\phi_{b,20}}{\phi_{b,30}} = \frac{6\alpha_g}{\phi_{b,32}} \tag{6.43}$$

To express $A_i(t)$ in terms of $\alpha_g(t)$, more information on the size distribution is needed. In case of a mono-sized bubble size distribution $\phi_{b,30} = \phi_b^3$, $\phi_{b,20} = \phi_b^2$ and $\phi_{b,32} = \phi_b$.

Scaling Eqn.(6.43) with Eqn.(6.37), one has

$$A_i(t) = A_{i,ini} \frac{\phi_{b,ini}}{\phi_b(t)} \frac{\alpha_g(t)}{\alpha_{g,ini}} \tag{6.44}$$

Directly from Eqn.(6.41)

$$\phi_b(t) = \Big[\frac{6}{\pi} \frac{1}{n_{b,ini}^{total}(t_{ini})} \frac{\rho_{ini}}{\rho_m(t)} \alpha_g(t) \Big]^{1/3} \tag{6.45}$$

Since Eqn.(6.36), one has

$$\phi_b(t) = \phi_{b,ini} \Big[\frac{\rho_{ini}}{\rho_m(t)} \frac{\alpha_g(t)}{\alpha_{g,ini}} \Big]^{1/3} \tag{6.46}$$

and substituting Eqn.(6.46) in Eqn.(6.44), we find

$$\begin{aligned} A_i &= A_{i,ini}\Big[\frac{\rho_{g,ini}}{\rho_m(t)}\frac{\alpha_g(t)}{\alpha_{g,ini}}\Big]^{-1/3}\Big[\frac{\alpha_g(t)}{\alpha_{g,ini}}\Big] \\ &= A_{i,ini}\Big[\frac{\rho_{g,ini}}{\rho_m(t)}\Big]^{-1/3}\Big[\frac{\alpha_g(t)}{\alpha_{g,ini}}\Big]^{2/3} \\ &= A_{i,ini}\Big[\frac{\rho_m(t)}{\rho_{g,ini}}\Big]^{1/3}\Big[\frac{\alpha_g(t)}{\alpha_{g,ini}}\Big]^{2/3} \end{aligned} \tag{6.47}$$

This is an explicit equation for the interface area density as function of the initial conditions and the vapour volume fraction. It holds as long as the assumption of independent bubbles holds. At high vapour volume fraction, a transition takes place and one makes the transition from bubbles in liquid to droplets in gas.

After the transition we can view the two phase medium as a collection of shrinking liquid droplets surrounded by gas, rather than a collection of growing bubbles in liquid. After the transition the equation for interfacial area density should be given by

$$A_i = A_{i,final}\Big[\frac{\rho_m(t)}{\rho_{l,final}}\Big]^{1/3}\Big[\frac{\alpha_l(t)}{\alpha_{l,final}}\Big]^{2/3} \tag{6.48}$$

Here we have introduced the liquid volume fraction and density in the final state as reference. Since the liquid volume fraction is decreasing in time, the interface area density is now decreasing in time. To use this formula, it is necessary to choose a final state with a little liquid left, in similar way as the initial state had already some vapour present after the critical bubble nucleation.

During a simulation one can switch from using Eqn.(6.47) to using Eqn.(6.48) at the moment they are equal. The determination of the accuracy of such an approach needs further investigation.

In summary, the interface area density is zero before nucleation. After nucleation it grows starting from an initial value. After the transition from bubble growth to shrinking droplet it decreases to a final value near zero.

Flow-regime-dependent interfacial area density model

In (59), Pinhasi et al. proposed a simplified interfacial area model which is flow regime dependent. For bubbly flows ($\alpha_g < 0.3$), it is assumed that the bubbles are spherical and having similar diameters throughout one cross-section. Then, using the notations introduced above, it can be shown that the interfacial area density is given by

$$A_i = (36\pi n_b^{total})^{1/3} \alpha_g^{2/3} \tag{6.49}$$

in which n_b is the bubble number density. For the bubbly-droplets transitional regime or Churn-turbulent flow regime($0.3 < \alpha_g < 0.7$), the interfacial area density is influenced by bubble break-up and bubble coalescence at the same time. The former tends to increase the interfacial area density while the latter tends to decrease. The interfacial area density then is taken as constant in that regime and equal to the value at $\alpha_g = 0.3$

$$A_i = (36\pi n_b^{total})^{1/3} (0.3)^{2/3} \tag{6.50}$$

For droplet flows $\alpha_g > 0.7$, the interfacial area density takes the form as

$$A_i = (36\pi n_d^{total})^{1/3} (1-\alpha_g)^{2/3} \tag{6.51}$$

It should be noted for (59) that the initial bubble number density is from experimental data while no information on the droplet number density has been given.

6.2.3 Interfacial fluxes: phase transition

The quantitative interfacial fluxes model is developed from non-equilibrium thermodynamics. We start with a very brief introduction to non-equilibrium thermodynamics, mainly concentrating on the two cornerstones of the theory, the entropy production rate and the local-equilibrium hypothesis. Then we shall introduce the interfacial fluxes model developed by Kjelstrup and Bedeaux for heterogeneous non-equilibrium system (43) which will allow us to include the influence of phenomena at the liquid-vapour interface into the interfacial models.

Introduction of non-equilibrium thermodynamics

The fundament of classic thermodynamics is based on thermodynamic equilibrium. However, many natural processes are irreversible processes in thermodynamic non-equilibrium, including heat conduction, mass diffusion, electrokinetic phenomena, electrode reactions and chemical reactions. As the time proceeds, systems in those processes are continuously changing and spontaneously approaching thermodynamic equilibrium. The research on those irreversible thermodynamic processes boosted the development of non-equilibrium thermodynamics, which can be traced back to the nineteenth century. But it is from the $1930s$, when Lars Onsager, a Norwegian researcher, started his pioneering research works, that the research on non-equilibrium thermodynamics bloomed. Onsager is regarded as the founder of non-equilibrium thermodynamics and received the Noble Prize in Chemistry in 1968 (43).

Non-equilibrium thermodynamics describes transport processes in systems that are in global non-equilibrium. But some thermodynamic parameters like temperature, pressure and entropy etc. have clear definitions in thermodynamic equilibrium systems only. To overcome this difficulty, non-equilibrium thermodynamics uses a local-equilibrium hypothesis, which assumes the system in non-equilibrium can be separated into many system elements. One system element is so small from a macroscopic perspective that its properties can be represented by the properties of one point inside of it, but big enough from a microscopic perspective that it contains sufficiently many molecules that its properties can be evaluated statistically. At moment t, the system is separated into n pieces of system elements. Assuming after time interval dt, each system element has reached its own equilibrium states, it is possible to define the thermodynamic parameters, e.g. T_i, p_i or s_i etc. for every system element. In this way, the whole system, still not in global equilibrium, can be described by the thermodynamic parameters of all system elements.

The key feature in non-equilibrium thermodynamics is entropy production. Using the local equilibrium hypothesis, the second law of thermodynamics can be reformulated in terms of the local entropy production rate in the system, σ_s, which is given by the product sum of the so-called conjugate fluxes, J_i and forces X_i, in the system. The second law becomes

$$\sigma_s = \sum_i J_i X_i \geq 0 \tag{6.52}$$

Each flux is a linear combination of all forces and the corresponding phenomenological coefficients L_{ij},

$$J_i = \sum_j L_{ij} X_j \tag{6.53}$$

The applications of non-equilibrium thermodynamics concentrate on

- distinguishing and deriving the driving forces X_j;
- modeling and validating the phenomenological coefficients L_{ij};
- estimating and validating the fluxes J_i.

The Kjelstrup-Bedeaux model

Kjelstrup and Bedeaux developed a non-equilibrium thermodynamics theory in great detail for heterogeneous systems, which distinguishes itself from the one for homogeneous systems in considering interfaces, or phase boundaries. Their theory is suitable for the BLEVE simulation for the careful considerations on the interfaces when the interfacial fluxes are evaluated. Meanwhile, Kjelstrup and Bedeaux also give many application examples, of which the case of 'evaporation and condensation' can be used as the interfacial fluxes model directly (43).

In Chapter 11 of (43), the entropy production σ_s in the interface between the vapour and the liquid is expressed in term of the adjacent liquid temperature T^l or the adjacent vapour temperature T^g as

$$\begin{aligned}
\sigma_s(T^l) &= J_q^{'g}\Big[\frac{1}{T^g}-\frac{1}{T^l}\Big]+J\Big[-\frac{\mu^g(T^l)-\mu^l(T^l)}{T^l}\Big] \\
&\equiv J_q^{'g}\Delta_{l,g}(\frac{1}{T})+J\Big[-\frac{\Delta_{l,g}\mu(T^l)}{T^l}\Big] \qquad (6.54) \\
\sigma_s(T^g) &= J_q^{'l}\Big[\frac{1}{T^g}-\frac{1}{T^l}\Big]+J\Big[-\frac{\mu^g(T^g)-\mu^l(T^g)}{T^g}\Big] \\
&\equiv J_q^{'l}\Delta_{l,g}(\frac{1}{T})+J\Big[-\frac{\Delta_{l,g}\mu(T^g)}{T^g}\Big] \qquad (6.55)
\end{aligned}$$

in which

$\Delta_{l,g}(\frac{1}{T})$	denotes the thermal driving force
$-\frac{\Delta_{l,g}\mu(T^k)}{T^k}$	denotes the chemical driving force
J	is the mass flux
$J_q^{'g}$	is the measurable heat flux from the vapour into the interface
$J_q^{'l}$	is the measurable heat flux from the liquid into the interface

For non-ideal gases concerned in this research, the chemical force is expressed as

$$-\frac{\Delta_{l,g}\mu(T)}{T} = -\mathbb{R}\,l\,n\frac{f}{f_{sat}(T)} \tag{6.56}$$

where f is the fugacity and $f_{sat}(T)$ is the saturation fugacity at the temperature T. Because the total heat flux through the interface J_q is constant and satisfies the identity

$$J_q = J_q^{'g} + h^g J = J_q^{'l} + h^l J \tag{6.57}$$

we need to evaluate the fluxes from one side of the interface only, e.g. the liquid side. The flux equations derived from Eqn.(6.54) are

$$\begin{aligned} \Delta_{l,g}\left(\frac{1}{T}\right) &= r_{qq}^{s,g} J_q^{'g} + r_{q\mu}^{s,g} J \\ -\mathbb{R}\,l\,n\frac{f^l}{f_{sat}(T^l)} &= r_{\mu q}^{s,g} J_q^{'g} + r_{\mu\mu}^{s,g} J \end{aligned} \tag{6.58}$$

Eqn.(6.58) expresses that the interfacial fluxes are coupled with the driving forces by the corresponding interface resistivities, which can be derived from kinetic the-

ory as (page 165 in (43))

$$
\begin{aligned}
r_{qq}^{s,g} &= \frac{\sqrt{\pi}(T^s)^{-2}}{4\mathbb{R}\rho_e^g v_{mp}}\left(1+\frac{104}{25\pi}\right) \\
r_{q\mu}^{s,g} = r_{\mu q}^{s,g} &= \frac{\sqrt{\pi}(T^s)^{-1}}{8\rho_e^g v_{mp}}\left(1+\frac{16}{5\pi}\right) \\
r_{\mu\mu}^{s,g} &= \frac{2\mathbb{R}\sqrt{\pi}}{\rho_e^g v_{mp}}\left(\sigma_c^{-1}+\frac{1}{\pi}-\frac{23}{32}\right)
\end{aligned}
\tag{6.59}
$$

in which T^s is the interface temperature; $v_{mp}(T^s)=\sqrt{2\mathbb{R}T^s/m_M}$ is the most probable thermal velocity; ρ_e^g is the equilibrium coexistence molar density of the gas; σ_c, the condensation coefficient and m_M the molar mass.

For σ_c, values between 0.1 and 1.0 have been reported (101) and later, σ_c is found to increase from a value of about 0.4 close to the critical point to a value of about 0.8 close to the triple point in non-equilibrium molecular dynamics (NEMD) simulations (100). An averaged value of 0.6 is chosen for the BLEVE simulation since no analytical expression for σ_c can be derived from the NEMD data. For the interface temperature T^s, this temperature can be well approximated by the liquid temperature very close to the interface (73). In our BLEVE simulation, the interface temperature T^s has to be approximated by the liquid temperature T^l because the temperature distribution with one fluid particle in the particle-path algorithm is not available in general and we have to assume the liquid temperature very close to the interface is not different from the ones away from the interface within one fluid particle.

In the BLEVE simulation, the liquid/vapour pressure p, the liquid enthalpy h^l and the vapour enthalpy h^g are numerically solved from EVUT Euler equations. Then the liquid temperature T^l, the vapour temperature T^g, the liquid fugacity f_l and the saturation fugacity $f_{sat}(T_l)$ are known from the equation of state. As the result, Eqn.(6.58, 6.59) can be used to solve for $J_q^{'g}$ and J as long as the interface temperature T^s is known. When $J_q^{'g}$ and J are known, the interfacial fluxes at the liquid side can then be solved from Eqn.(6.57).

The interfacial fluxes model developed by Kjelstrup and Bedeaux is interfacial area dependent and together with the interfacial area density model, the interfacial mass flux $m_{i,g}$ and the interfacial heat flux $q_{i,k}$ for EVUT-Euler equations can been derived as

$$m_{i,g} = JA_iA \tag{6.60}$$

$$q_{i,k} = J_q^{'k}A_iA \tag{6.61}$$

6.3 The wall and tunnel geometry terms

Including the tunnel geometry terms is quite straight forward. In 1D geometry, the cross-sectional area $A(x)$ and the altitude $Z(x)$ of the tunnel are given functions of the locations in the tunnel axial direction. For the reason of simplification, we assume the tunnel has constant cross-sectional area and is placed horizontally, therefore $dA/dx = 0$ and $dZ/dx = 0$.

More importantly, we also simplify the wall source terms by setting the wall adiabatic $q_{w,k} = 0$ and frictionless $\tau_{w,k} = 0$ because

1. When a BLEVE occurs in a tunnel, the heat transfer between the tunnel wall and the fluids in the tunnel is a process much slower than the shock blasting phenomena. Therefore the amount of heat transferred, if existing, is relatively small. On the other hand, the feature of a BLEVE we want to capture is the rapid phase transition triggered by homogeneous nucleation and driven by the excessive energy stored in PLG itself instead of transferred from the ambient. If the heat transferred from the tunnel wall is comparable to the excessive energy stored in PLG, the nucleation will most probably occur on the wall taking the form of heterogeneous bubble nucleation, instead of homogeneous bubble nucleation;

2. As the length scale of a BLEVE transits from centimeters in the lab to meters in the reality, the influence of the wall (friction and heat transfer) on the bulk fluid in average in 1D simulation will definitely decrease, no matter from the dynamic or the thermodynamic point of view.

For above reasons, we think our simplifications on the wall geometry terms are reasonable and proper.

CHAPTER 7

INTEGRATION OF THE TUD MODEL FOR BLEVE SIMULATION

In previous chapters, components for BLEVE simulation has been introduced separately, including

- The conservative equations: the EVUT Euler equations for two-phase flow and the normal Euler equation for single-phase flow;
- The solution algorithm: the particle-path algorithm of the method of characteristics;
- The equation of state: the Peng-Robinson-Stryjek-Vera EOS in the modified StanMix of FluidProp;
- The source term models
  - the interfacial fluxes models: the relaxation-time model; the Kjelstrup-Bedeaux interfacial fluxes model with the Delale et al. 2003 bubble nucleation model and the interfacial area evolution model;
  - the model for the wall and tunnel geometry terms: the adiabatic, frictionless wall and the horizontal tunnel with constant cross-sectional area.

In this chapter, we will introduce how to integrate the four parts together to predict the peak pressure of a shock blast generated by a BLEVE. For the purpose of convenient description and being in line with the Pinhasi et al. model and the TNO model, our model will be collectively named as 'the TUD model' in which the model using the relaxation time model for the interfacial fluxes is named as 'the TUD-RT model' and the model using the interfacial fluxes model derived from non-equilibrium thermodynamics is named as 'the TUD-NET model'.

7.1 Solution algorithm for the TUD-RT model

The TUD-RT model using the relaxation time model follows the path of previous researches (28) (58) and consists of

- **Conservation equations** The two-phase EVUT Euler equations for the PLG region and the single-phase Euler equations for the air region;
- **Solution algorithm** The two-phase PP-MOC algorithm for the PLG region and the single-phase PP-MOC algorithm for the air region;
- **E.O.S.** The PRSV-EOS;
- **Source term models**
  - Interfacial fluxes: the relaxation-time model;
  - Tunnel relevant models: horizontal tunnel with uniform cross-section and adiabatic, frictionless wall.

Using EVUT Euler equation for the PLG region from the very beginning of the computation means automatically excluding bubble nucleation because obviously EVUT Euler equations can describe neither the single-phase flow nor the transition of single-phase flow to the two-phase flow (bubble nucleation). As the result, PLG must be initially two-phase and normally it is assumed that PLG is a two-phase mixture with very low vapour volume fraction, e.g. 10^{-6}. The low void fraction assures that, with certain mixing rule, the thermophysical properties of the PLG two-phase mixture is very close to the ones of the PLG liquid. Such treatments have been found in (28) (58) and (74).

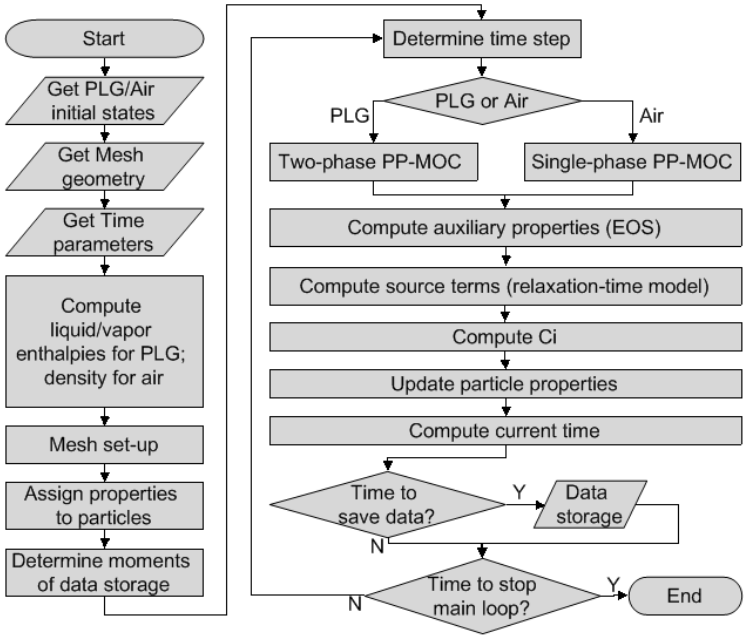

Figure 7.1: The TUD-RT model

The relaxation-time model is selected for the reason of simplicity and robustness. Similar to the arbitrary initial void fraction of the PLG mixture, the relaxation-time model also brings in another arbitrary parameter - the relaxation time. Therefore it will be revealed later that the TUD-RT model is not predictive on the peak pressure generated by shock blasts because shock blasts are sensitivity to the relaxation times.

The schematic plot of the integration of the TUD-RT model is in Fig.(7.1) and the computational steps are explained below:

- Step 1 - Get PLG/Air initial states: the initial pressure/temperature and arbitrary initial void fraction of PLG, the initial pressure/temperature of air and the inlet/outlet boundary conditions;
- Step 2 - Get Mesh geometry: the length, the mesh size (or the particle numbers) of the PLG region and the air region respectively;

- Step 3 - Get Time parameter: the total computational time and the frequency of data storage;
- Step 4 - Compute liquid/vapour enthalpies for PLG; density for air;
- Step 5 - Mesh set-up: build up the mesh, including the normal particles, the contact face, the inlet and the outlet;
- Step 6 - Assign properties to particles: assign properties to the normal particles, the contact face particles and the inlet/outlet particles;
- Step 7 - Determine the moments of data storage: because the time step of PP-MOC is random, the moments of data storage must be predefined for comparing the outputs from different computations;
- Step 8 - Determine time step: as explained in previous chapters, the minimum of the maximum time steps of all particles is chosen;
- Step 9 - PLG or Air: if the particle is PLG, two-phase PP-MOC is chosen for solving the pressure, velocity, void fraction, liquid/vapour enthalpies of that particle; if the particle is air, single-phase PP-MOC is chosen for solving the pressure, velocity and density of that particle;
- Step 10 - Compute auxiliary properties: use EOS to compute other auxiliary properties including densities and sonic speeds of PLG liquid/vapour/mixture; sonic speed of air etc.;
- Step 11 - Compute source terms: compute the wall and tunnel geometry terms and use the relaxation-time model to compute the interfacial fluxes for PLG particles;
- Step 12 - Compute C_i coefficients;
- Step 13 - Update particles properties;
- Step 14 - Compute current time;
- Step 15 - Time to save data: Yes to store data and proceed; No to proceed;
- Step 16 - Time to stop main loop: No to return to Step 8 ; Yes to stop.

7.2 Solution algorithm for the TUD-NET model

The TUD-NET model consists of

- **Conservation equations** The two-phase EVUT Euler equations for the two-phase particles and the single-phase Euler equations for the single-phase particles;
- **Solution algorithm** The two-phase PP-MOC algorithm for the two-phase particles and the single-phase PP-MOC algorithm for the single-phase particles;
- **E.O.S.** The PRSV-EOS;
- **Source term models**
  - Interfacial fluxes: the Kjelstrup-Bedeaux model with the Delale et al. 2003 bubble nucleation model and the interfacial area evolution model;
  - Tunnel relevant settings: Horizontal tunnel with uniform cross-section and adiabatic, frictionless wall.

Compared with the TUD-RT model, the TUD-NET model is phase-dependent instead of fluid-dependent, which means for two-phase particles (only possible for PLG), two-phase PP-MOC is chosen while for single-phase particle (PLG or air), single-phase PP-MOC is applied. In this way, it is possible to implement bubble nucleation in the model because PLG particles can be initially single-phase. The function of bubble nucleation model is to describe the generation of bubble, or mathematically to say, to allow the vapour volume fraction jump from zero to a finite value in the process of bubble nucleation. When the criteria of bubble nucleation are fulfilled, single-phase PLG particles will become two-phase PLG particles and correspondingly, the solution algorithm for solving their properties is switched.

The schematic plot of the integration of the TUD-NET model is in Fig.(7.2) and the computational steps are explained below:

- Step 1 - Get PLG/Air initial states: the initial pressure/temperature of PLG liquid, the initial pressure/temperature of air and the inlet/outlet boundary conditions;

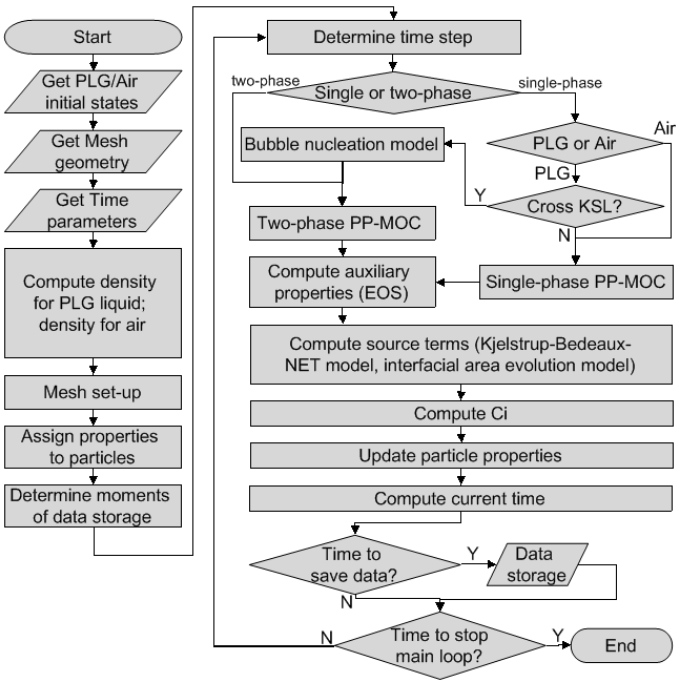

Figure 7.2: The TUD-NET model

- Step 2 - Get Mesh geometry: the length, the mesh size (or the particle numbers) of the PLG region and the air region respectively;
- Step 3 - Get Time parameter: the total computational time and the frequency of data storage;
- Step 4 - Compute enthalpy for PLG liquid; density for air;
- Step 5 - Mesh set-up: build up the mesh, including the normal particles, the contact face, the inlet and the outlet;
- Step 6 - Assign properties to particles: assign properties to the normal particles, the contact face particles and the inlet/outlet particles;
- Step 7 - Determine the moments of data storage: because the time step of PP-MOC is random, the moments of data storage must be predefined for comparing the outputs from different computations;

- Step 8 - Determine time step: as explained in previous chapters, the minimum of the maximum time steps of all particles is chosen;
- Step 9 - Single or two-phase: if the particle is two-phase (only possible for PLG), two-phase PP-MOC is chosen for solving the pressure, velocity, void fraction, liquid/vapour enthalpies of that particle. If the particle is a single-phase particle, single-phase PP-MOC is chosen for solving the pressure, velocity and density of that particle. If the particle is a single-phase PLG particle which will cross the KSL at the following moment, bubble nucleation model will be applied, which transforms that particle into two-phase. From the next moment on, two-phase PP-MOC will be chosen for solving the pressure, velocity, void fraction, liquid/vapour enthalpies of that particle;
- Step 10 - Compute auxiliary properties: use EOS to compute other auxiliary properties including densities and sonic speeds of two-phase particles; sonic speed of single-phase particles etc.;
- Step 11 - Compute source terms: compute the wall and tunnel geometry terms and use the Kjelstrup-Bedeaux model and the interfacial area evolution model to compute the interfacial fluxes terms of two-phase particles;
- Step 12 - Compute C_i coefficients;
- Step 13 - Update particles properties;
- Step 14 - Compute current time;
- Step 15 - Time to save data: Yes to store data and proceed; No to proceed;
- Step 16 - Time to stop main loop: No to return to Step 8 ; Yes to stop.

CHAPTER 8

RESULTS FROM THE TUD-RT MODEL

In this chapter, we will give the results from the TUD-RT model using the relaxation time model for the interfacial fluxes. Those results can be used to qualitatively understand the BLEVE phenomena in 1D tunnel geometry. A precondition for using the relaxation time model is that PLG must initially consist of two phases, because there is no bubble nucleation model that takes the zero-to-non-zero jump of the void fraction into account, therefore the initial void fraction throughout the PLG region is chosen to be an arbitrary non-zero small value.

The ambient air is initially in the normal state, $1\,atm$ and $25°C$. The computational domain is taking the exact formation as Fig.(2.4) demonstrates.

8.1 Initially saturated PLG two-phase mixture

In this section, it is assumed that the PLG liquid and the PLG vapour are initially at their saturated states. For the standard case, the design pressure of the PLG tank is used as the initial PLG pressure when the tank ruptures. Several important features can be observed from the computational results, including the rarefaction wave, the pressure-drop, the pressure-recovery, the moving of the contact face as well as the development of the shock wave. The influences of the initial PLG pressures and the relaxation times on those phenomena have been examined. The

relaxation time model is adequate for the qualitatively analysis of a BLEVE only.

8.1.1 The standard case: tank ruptured at the design pressure

The design pressure of PLG tank is $17.7\,bar$, therefore the initial settings for this standard case computation are given as

- PLG: Propane
- Initial PLG pressure: $p_0 = 17.7\,bar$
- Initial PLG liquid/vapour temperature: $T_0 = T_{sat}(p_0) = 324.25K = 0.877\,T_c$
- Initial void fraction: $\alpha = 10^{-6}$
- Relaxation time: $t_{i,k} = 0.1\,ms$

The tank is assumed to be fully loaded. Fig.(8.1, 8.2, 8.3, 8.4, 8.5) give the profile evolution for pressure, velocity, density, sonic speed and void fraction, respectively. We will explain some important features from those figures. The red dot in the profiles represents the location of the contact face between the PLG and the air.

In Fig.(8.1) of the pressure profile, initially the system consists of two parts, the PLG region at high pressure and the air region at $1\,atm$. As the time proceeds, the contact face is moving rightwards meaning the PLG region is expanding and there is no pressure jump at the contact face meaning the pressure continuity always holds at the contact face. A shock gradually forms during its propagating to the right end. A rarefaction wave followed by a pressure-recovery is propagating to the left end. The pressure-recovery is due to liquid-to-vapour transition and results in temporary liquid-vapour equilibrium at a pressure lower than the initial PLG pressure. When the rarefaction wave hits the left wall, the pressure on the wall drops to a level lower than ever due to the reflection of the rarefaction wave, which can cause more liquid to vapourise closing to the left wall, see Fig.(8.5). Later on, the rarefaction wave disappears and the system consists of three parts, an expanding PLG two-phase mixture, the compressed air and the undisturbed air.

In Fig.(8.2) of the velocity profile, the system is initially at rest. As the time proceeds, the PLG and the air near the contact face start to move. Gradually, a shock is formed and propagating to the right end, represented by the velocity jump in

the air region. The velocity continuity also holds at the contact face. In Fig.(8.3) of the density profile, two density jumps occur at the shock and the contact face, respectively.

In Fig.(8.4) of the sonic speed profile, it is physically correct to observe the lowest sonic speed in the PLG region appears in the region with medium void fraction. The existence of the two-phase interface, especially in the form of bubble surface, can slow down the propagation of the sound wave within the fluid.

In Fig.(8.5) of the void fraction profile, the rapid vapourisation results in rapid growth in the void fraction, e.g. within $0.2\,ms$, the PLG near the contact face has almost fully vapourised. It can also be observed that the reflection of the rarefaction wave causes faster void fraction increasing closing to the left end wall.

Compared with the experiments on evaporation fronts discussed in Chpt.(2), the simulated 1D BLEVE using the TUD-RT model has demonstrated not a compression wave but a shock wave and the combination of the expansion wave and the evaporation front, which all attributes to the nature of rapid vapourisation of PLG liquid at relatively high superheat.

In following discussions, evolution of the profiles will take compact forms as shown in Fig.(8.6).

8.1.2 Influence of the initial PLG pressure

The initial PLG pressure has direct influences on the shock wave. Fig.(8.7) gives the evolution of the pressure profile of three initial PLG pressures, $8\,bar$, $18\,bar$ and $28\,bar$ using the same relaxation time $0.2\,ms$ and the same initial void fraction 1.0^{-6}. The profiles evolve in similar manners, but with different magnitudes. Faster shock waves also cause higher pressure jumps, which is physically correct.

8.1.3 Influence of the relaxation time

The value of the relaxation time influences the magnitude of the pressure-recovery and the shock wave. Fig.(8.8) demonstrates the evolution of the pressure profile of three relaxation times, $0.1\,ms$, $0.5\,ms$ and $2\,ms$ for the same initial PLG pressure $28\,bar$ and the same initial void fraction 10^{-6}. In the three cases, the propagation of the rarefaction wave are the same, however, the pressure-drop after the rarefac-

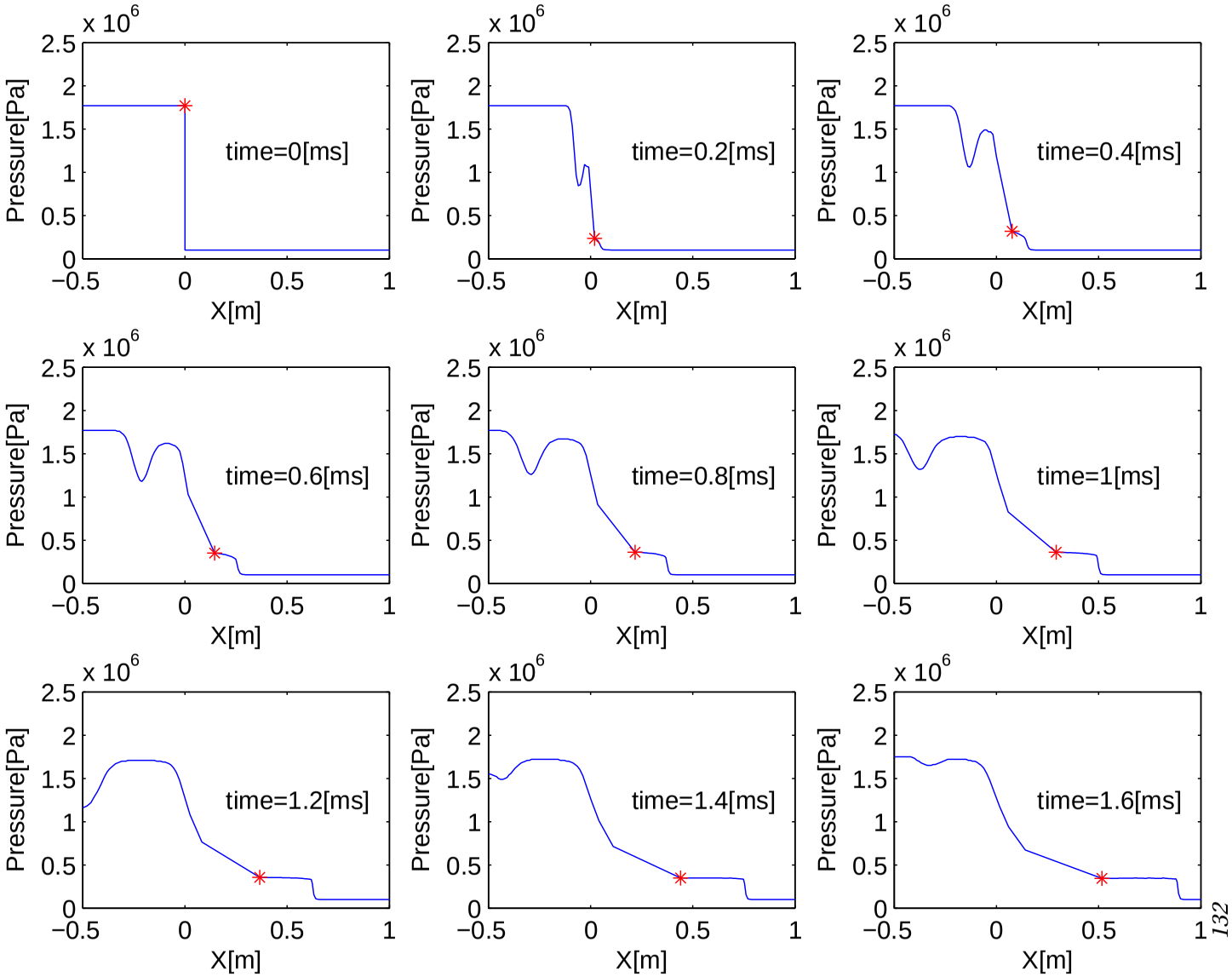

Figure 8.1: Evolution of pressure profile

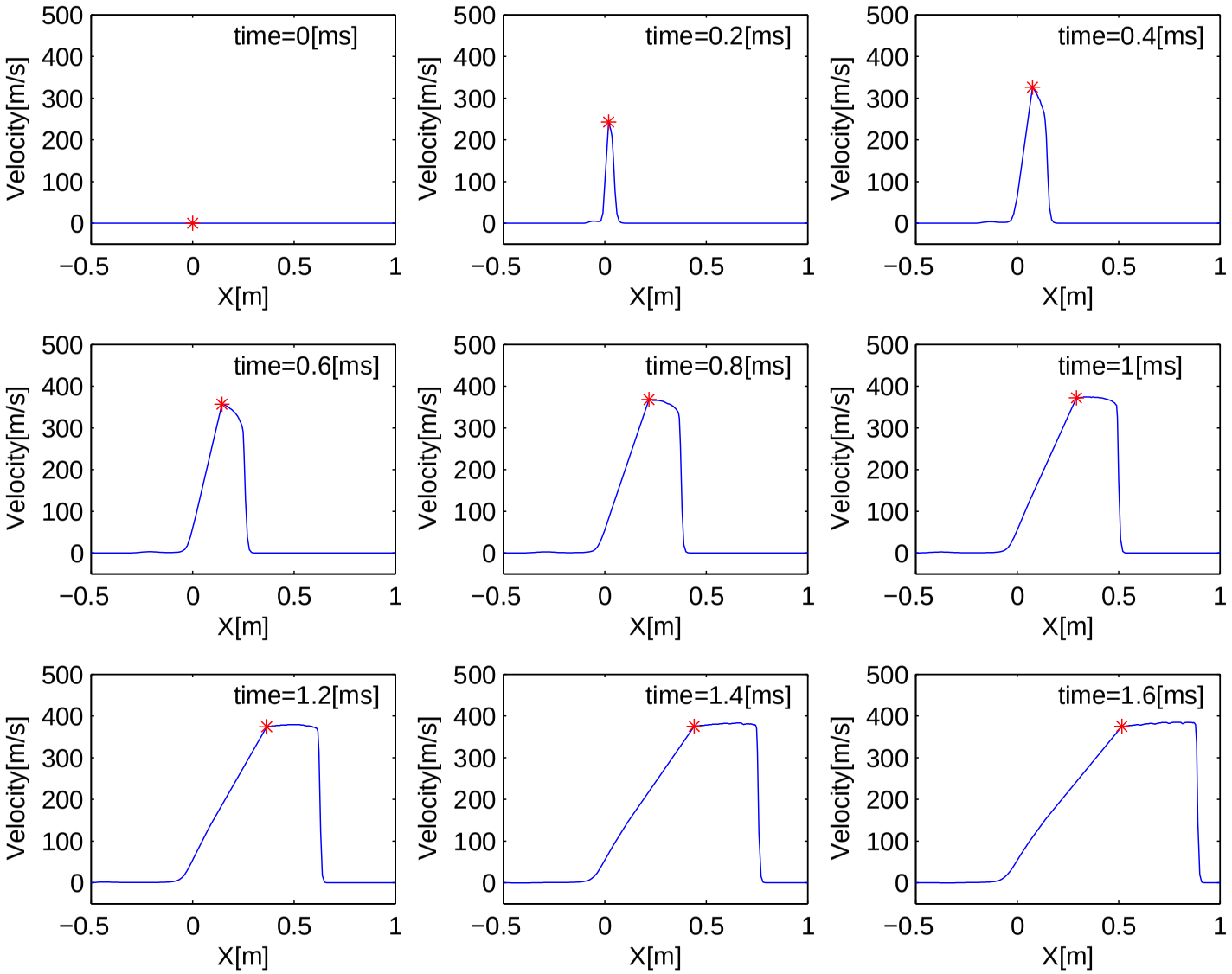

Figure 8.2: Evolution of velocity profile

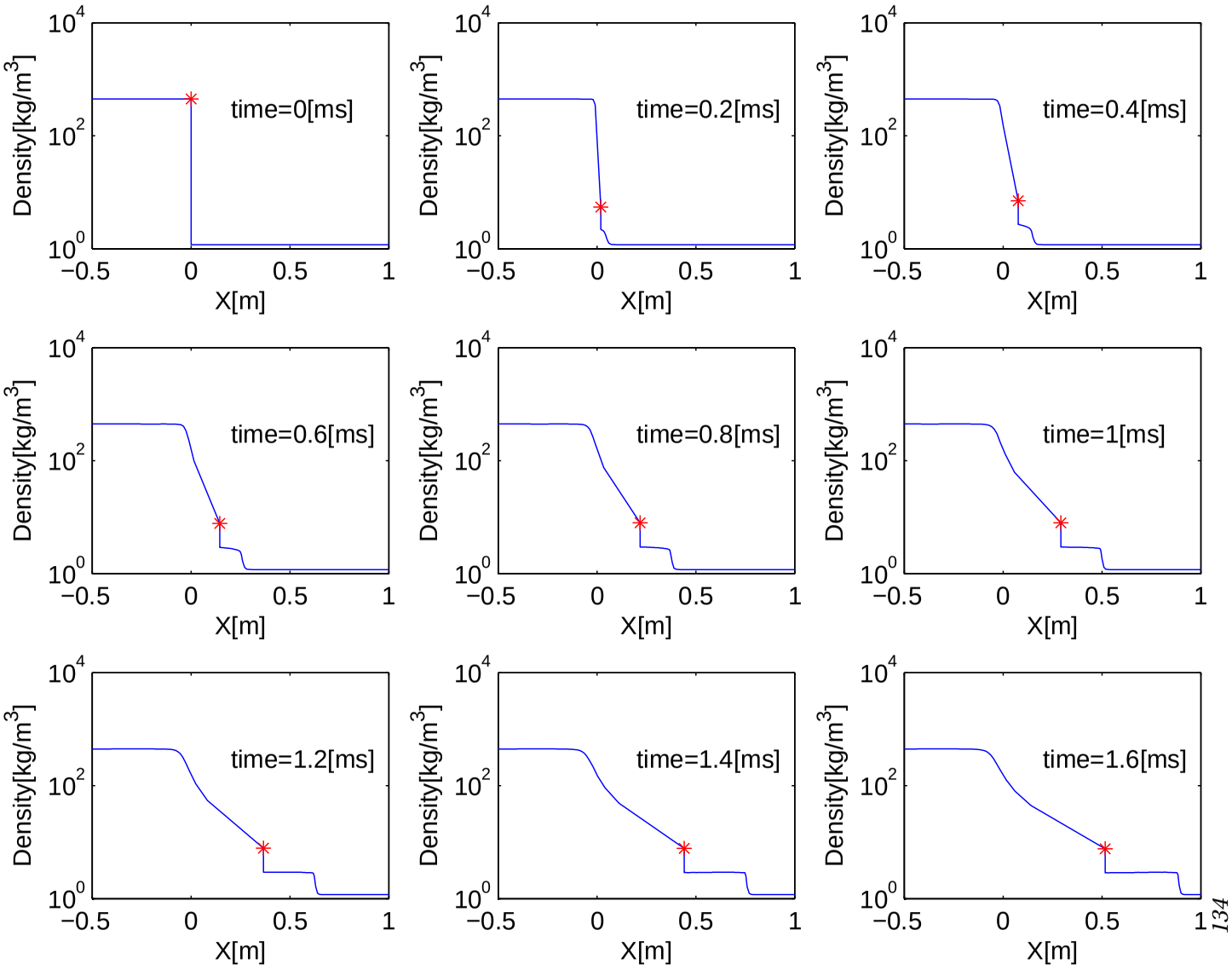

Figure 8.3: Evolution of density profile

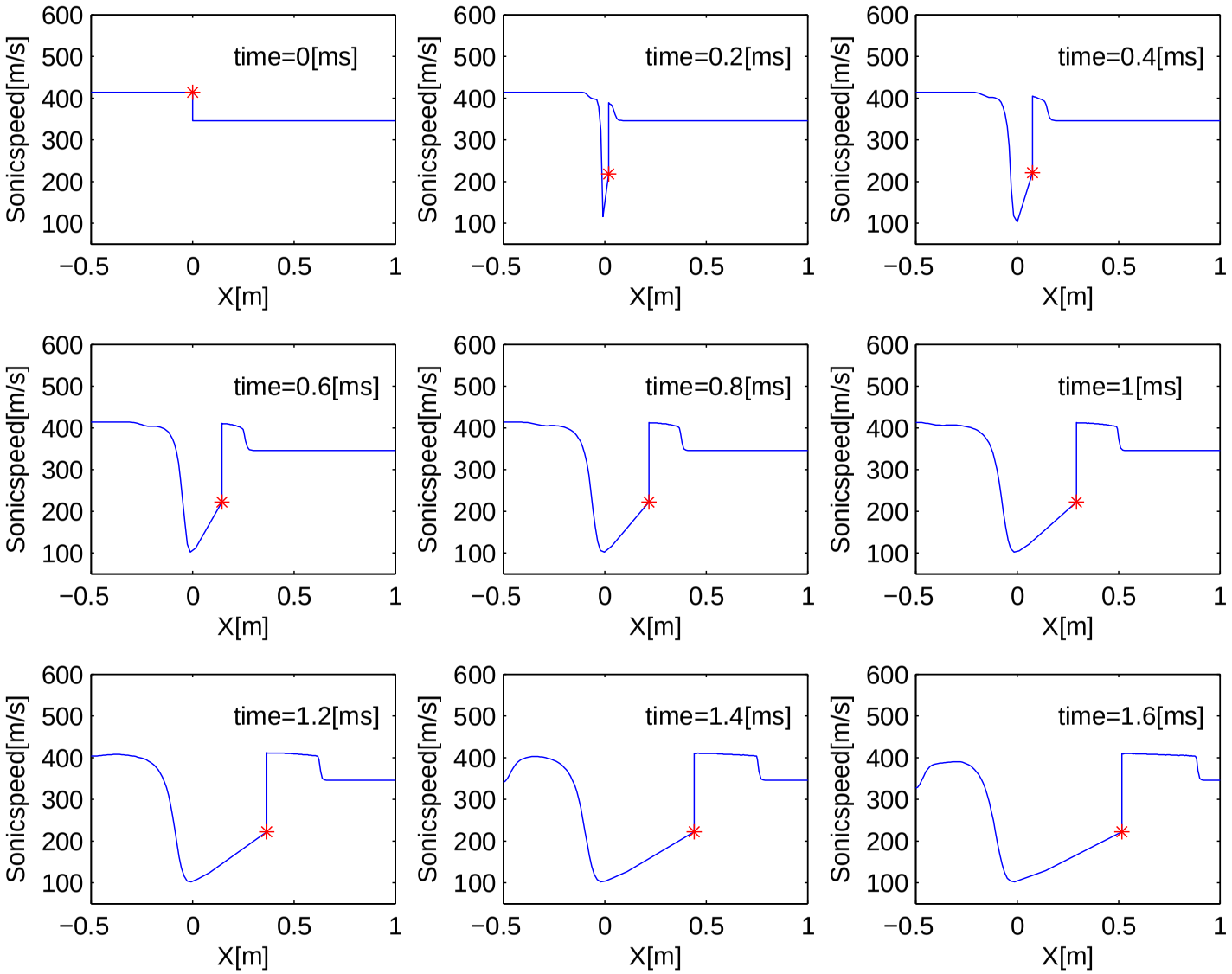

Figure 8.4: Evolution of sonic speed profile

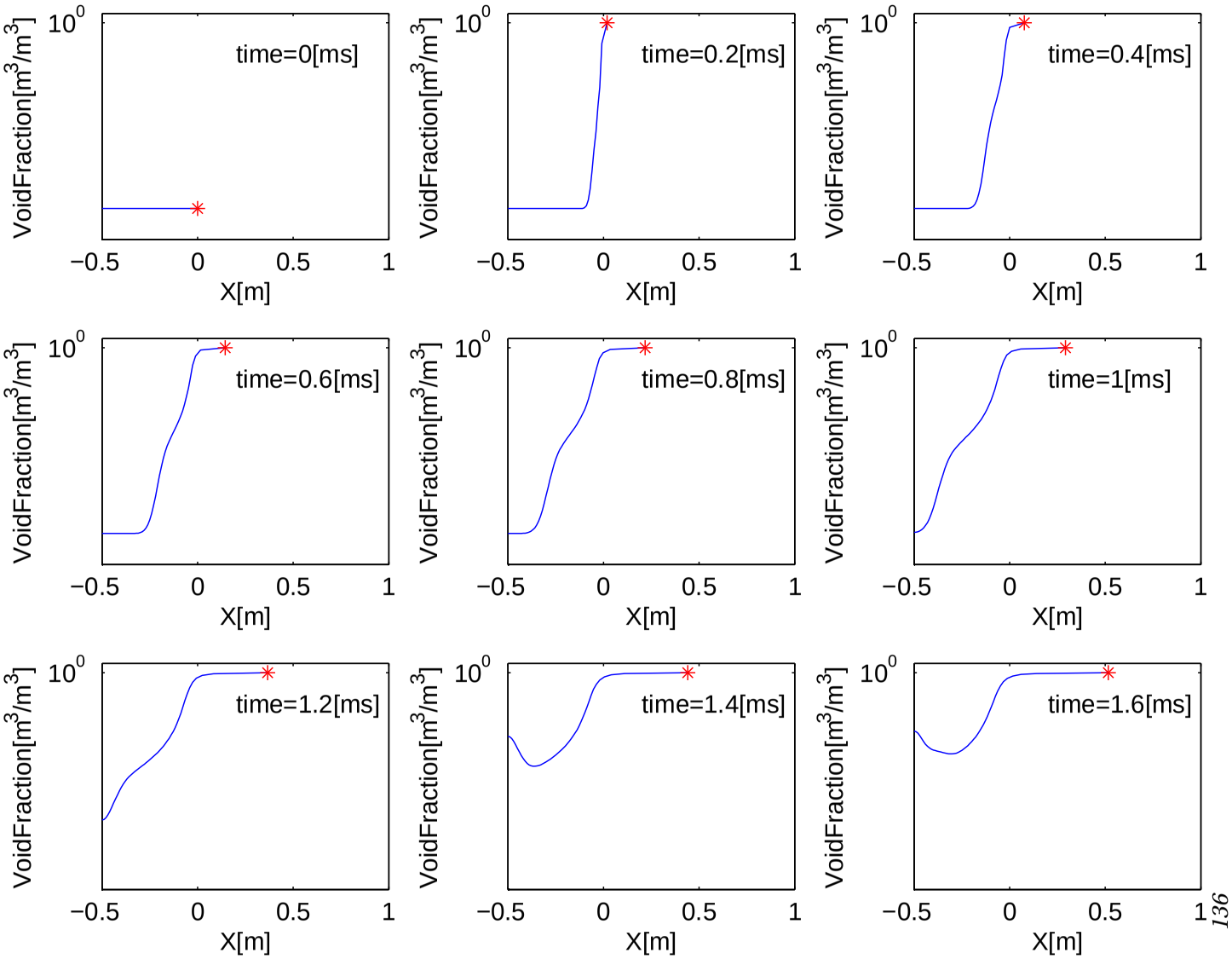

Figure 8.5: Evolution of void fraction profile

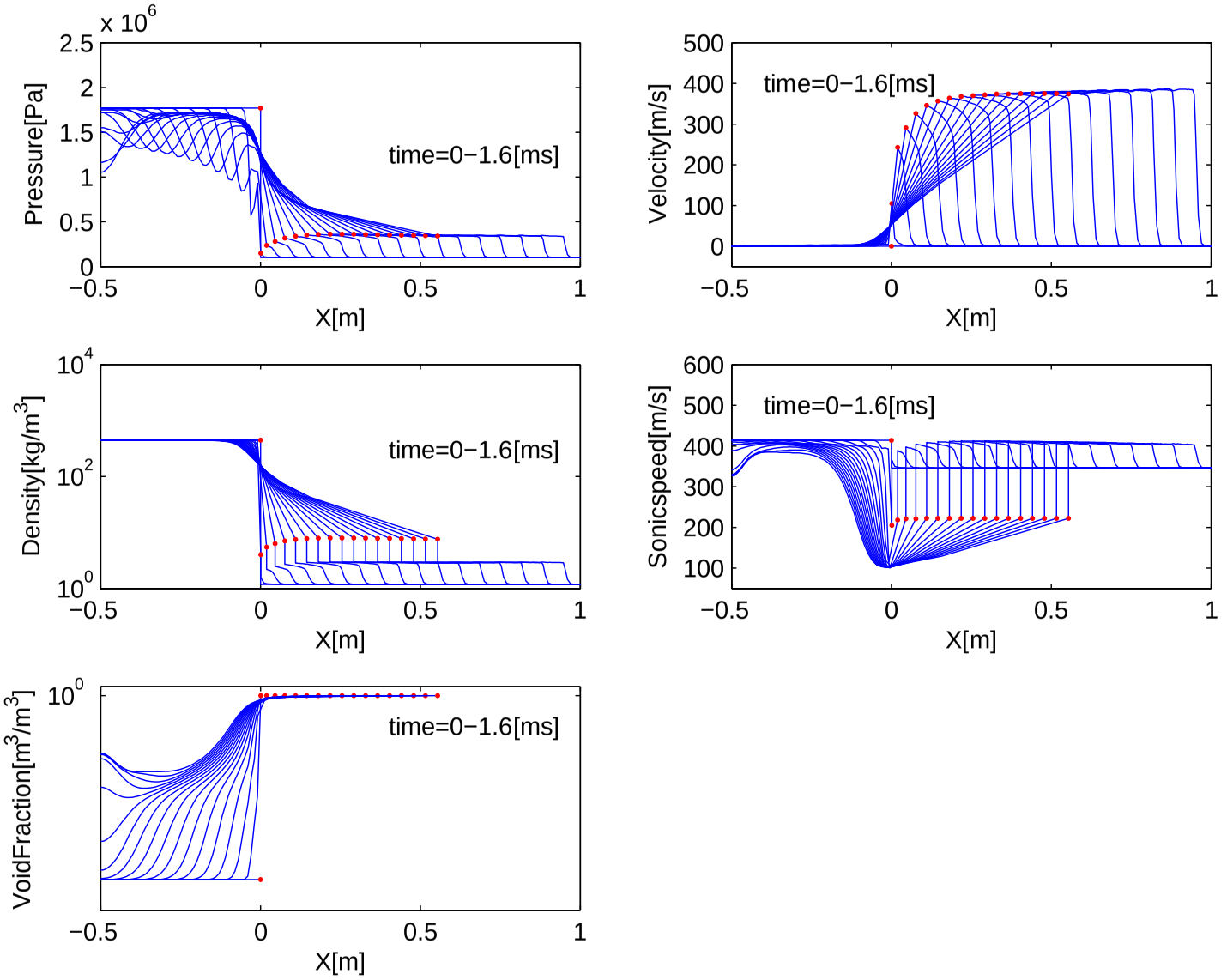

Figure 8.6: Evolution of the profiles

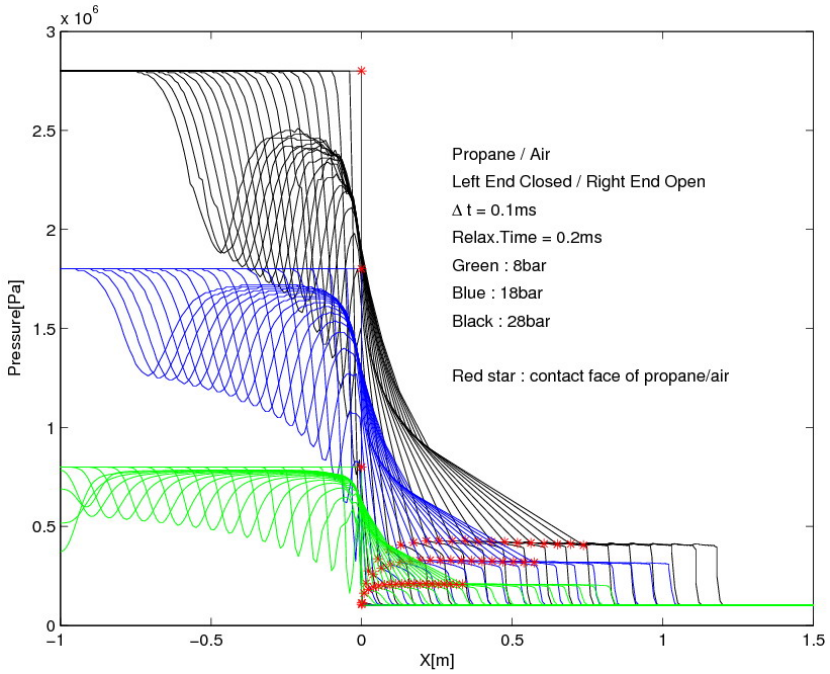

Figure 8.7: Influence of the initial PLG pressures

tion wave and the following pressure-recovery are different in magnitude. The shock speeds and the pressure jumps after the shock waves are also different in magnitude. Therefore, the relaxation time model can not be used as a predictive model.

8.2 Initially superheated PLG liquid with saturated PLG vapour

In this section, it is assumed that the PLG liquid is in a superheated state and the vapour is on the saturation curve with the same pressure as the liquid. This case may represent the scenario that bubble nucleation has already started in the PLG tank and keeps going due to external heating before the sudden tank rupture.

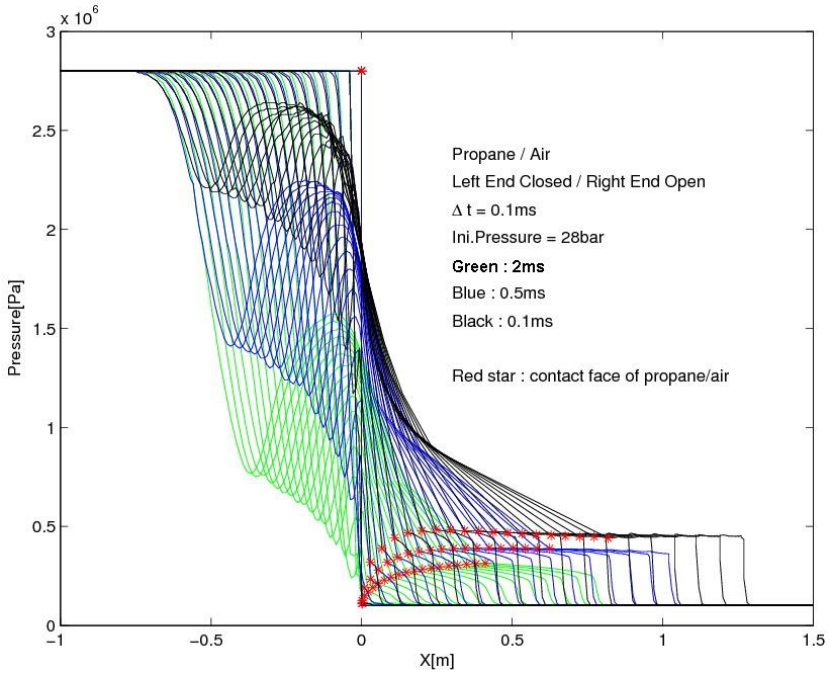

Figure 8.8: Influence of the relaxation time

The initial settings for the computation are given as below,

- PLG: Propane
- Initial PLG pressure: $p_0 = 17.7$ bar
- Initial PLG liquid temperature: $T_{0,l} = 1.05 \times T_{sat}(p_0) = 340.46K = 0.921\,T_c$
- Initial PLG vapour temperature: $T_{0,g} = T_{sat}(p_0) = 324.25K = 0.877\,T_c$
- Initial void fraction: $\alpha = 10^{-6}$
- Relaxation time: $t_{i,k} = 0.2\,ms$

Magnificent differences can be observed in the pressure profile and the void fraction profile in Fig.(8.9) from the ones in Fig.(8.6). The pressure and the void frac-

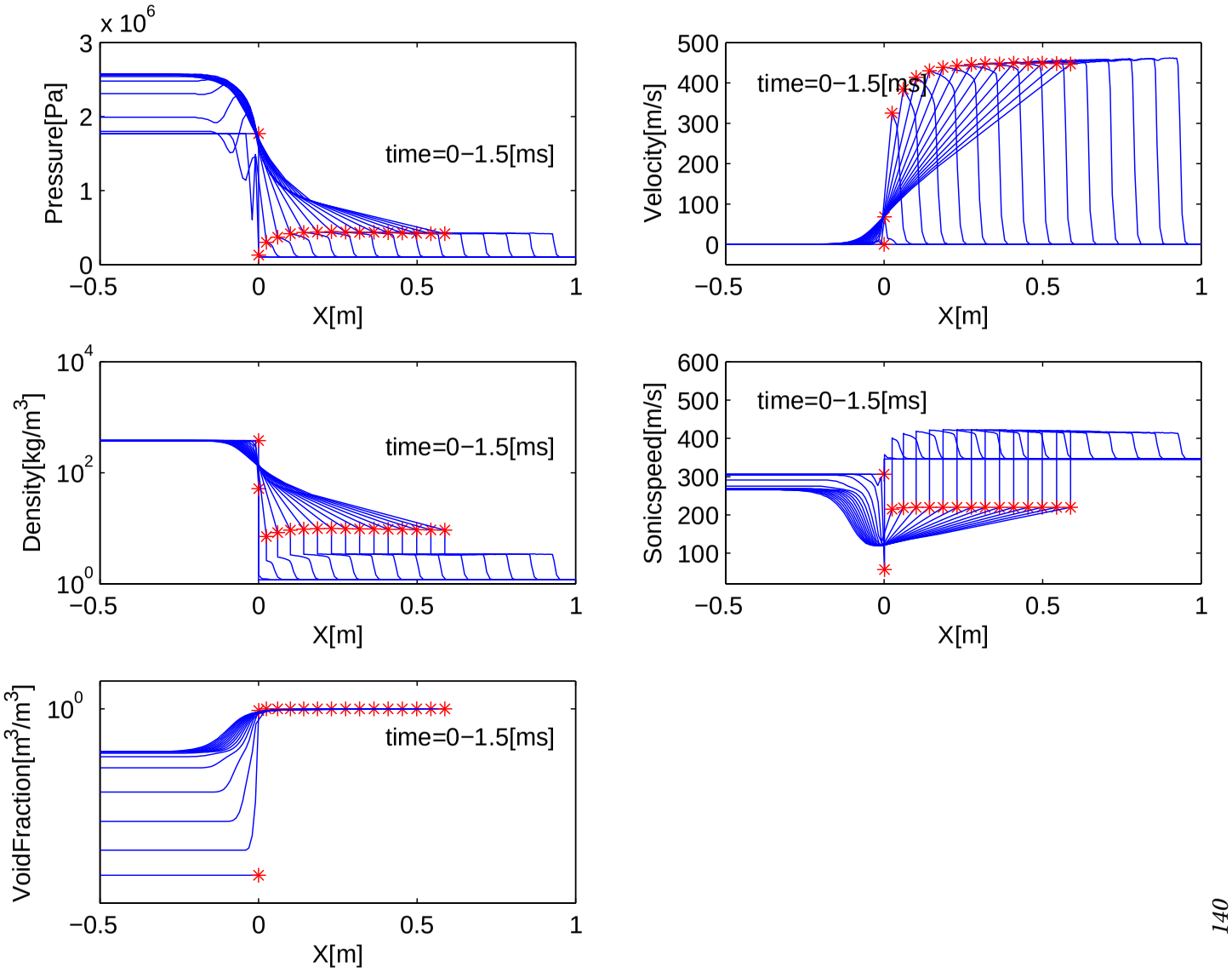

Figure 8.9: Evolution of the profiles: initially superheated liquid with initially saturated vapour

tion of the PLG mixture automatically increases before the rarefaction wave arrives. The reason is that the liquid is initially superheated and not in equilibrium with the neighbouring vapour which is saturated, the liquid-to-vapour phase transition starts automatically before the rarefaction wave arrives. As the result, the pressure of the PLG increases to a level higher than its initial value as well as the void fraction. It is also interesting to observe that the pressure of PLG mixture passed by the rarefaction wave becomes higher than the pressure of PLG mixture ahead of the rarefaction wave, which attributes to the larger void fraction caused by the depressurisation process of the rarefaction wave.

CHAPTER 9

RESULTS FROM THE TUD-NET MODEL

In this chapter, we will give the results from the TUD-NET model consisting of the Delale et al. 2003 model for the homogeneous bubble nucleation, the interfacial area evolution model and the Kjelstrup-Bedeaux model for the interfacial fluxes introduced in Chpt.(6). The introduction of homogeneous bubble nucleation model allows i) to set the initial PLG state as pure liquid instead of two-phase mixture; ii) the discussion on the possibilities of shock generation for the first time. Computations are carried out based on several parameters that may influence the shock, including the initial PLG temperature, the initial PLG pressure and the initial PLG volume.

The simulations use a very small time step and to keep the total computational cost affordable, the size of the computational domain is limited to μm scale. This does not prevent that relevant conclusions can be drawn.

The ambient air is initially in the normal state, $1 atm$ and $25°C$. The computational domain is taking the exact formation as Fig.(2.4) demonstrates.

9.1 The standard case: tank ruptured at the design pressure

The initial settings for the computation of the standard case are given as

- PLG: Propane
- Initial PLG pressure: $p_0 = 17.7\,bar$
- Initial PLG temperature: $T_{0,l} = T_{sat}(p_0) = 324.25\,K = 0.877\,T_c$

Fig.(9.1) demonstrates that the spacial profiles of the pressure, the velocity, the density, the sonic speed and the void fraction evolve in time. The position of the contact face is marked with a red star and the computation will stop if the shock is close to the left end or the outlet.

After observing those profiles, we can draw the conclusion that if the tank containing saturated PLG ruptures at the design pressure $17.7\,bar$, a BLEVE will not occur in the subsequent processes. As seen in the pressure evolution profile in Fig.(9.1), the contact face hardly moves outwards even after the rarefaction wave has reached the left end wall and no obvious pressure jump has been observed in the air region. The relatively slow movement of the contact face represents that the whole PLG region neither increases greatly in its total volume nor pushes the air aside rapidly. Therefore no shock has been generated. The velocity profile in Fig.(9.1) evolves in a roughly symmetric manner around the contact face showing that both fluids are flowing to the outlet together and there is no clear indication that PLG is pushing the air.

BLEVE does not occur because pure PLG liquid has not reached the superheat limit during the depressurisation process, hence homogeneous bubble nucleation has not been triggered to generate critical bubbles. Without large numbers of critical bubbles, phase transition from the liquid to the vapour through the bubbly interfaces becomes impossible. As the direct evidence, the void fraction evolution profile in Fig.(9.1) remains zero throughout the whole computation.

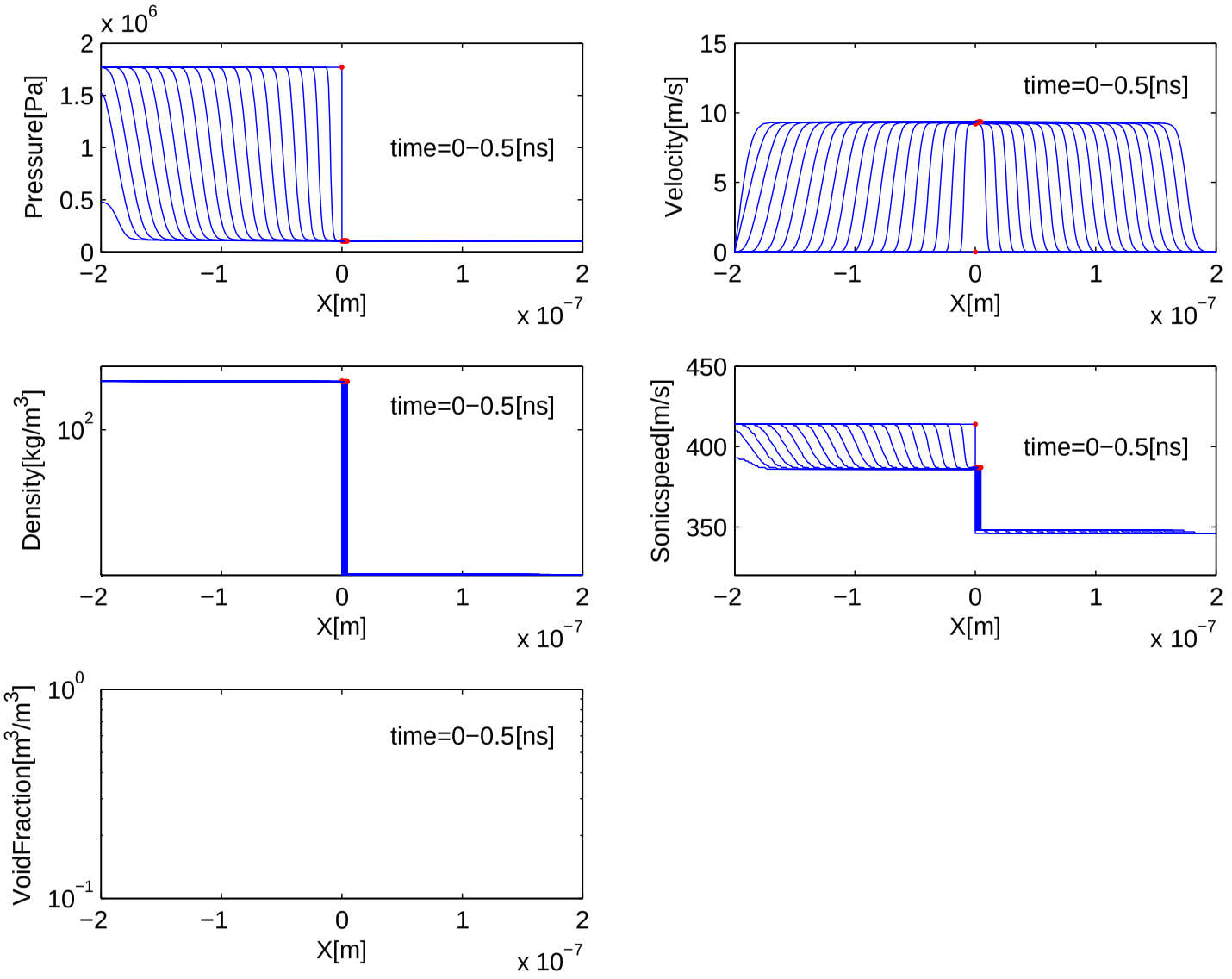

Figure 9.1: Evolution of the profiles: initially saturated pure liquid at $17.7bar$

9.2 Tank ruptured with $25\,bar$ saturated PLG

In this section, the initial pressures of the saturated PLG are taking a higher value, i.e. $25\,bar$ so that homogeneous bubble nucleation will occur during the depressurisation process as

- PLG: Propane
- Initial PLG pressure: $p_0 = 25\,bar$
- Initial PLG temperature: $T_0 = T_{sat}(p_0) = 340.92\,K = 0.922\,T_{cr}$

The results are demonstrated in Fig.(9.2). As shown in the pressure profiles, a shock with the pressure jump of approx. $0.47\,bar$ has been developed and further propagates to the outlet. The velocity jump at the shock has reached $100\,m/s$, almost 10 times the one in the standard case, which can not be completely explained by the difference in the PLG initial pressures. In the density evolution profile, two jumps can be clearly observed at the contact face and at the front of moving air respectively.

The void fraction profiles include several interesting observations. To the right of the contact face, the void fraction remains zero since it is in the air region. Jumps from zero void fraction to non-zero void fraction due to homogeneous bubble nucleation occur throughout the PLG region as the rarefaction wave propagates. Once the critical bubbles are formed, the vapourisation proceeds gradually compared with the sudden jump due to homogeneous bubble nucleation. It is speculated that the faster increasing of the void fraction close to the left end wall than in the region away from the left end wall is due to the reflection of the rarefaction wave on the solid surface.

Compared with the computation in the previous section, three key phenomena of a BLEVE have been recognized: i) the rapid boiling of the liquid recognized by the rapid increase of the void fraction in the PLG region; ii) the expansion of the PLG region recognized by the rapid motion of the contact face and iii) a shock generated in the air recognized by the pressure jump at the leading edge of the moving air. So we can say a BLEVE occurs.

The simulated BLEVE consists of the expansion wave, the contact discontinuity and the compression wave (in shock format) mentioned in Sec.(2.1.4). Because

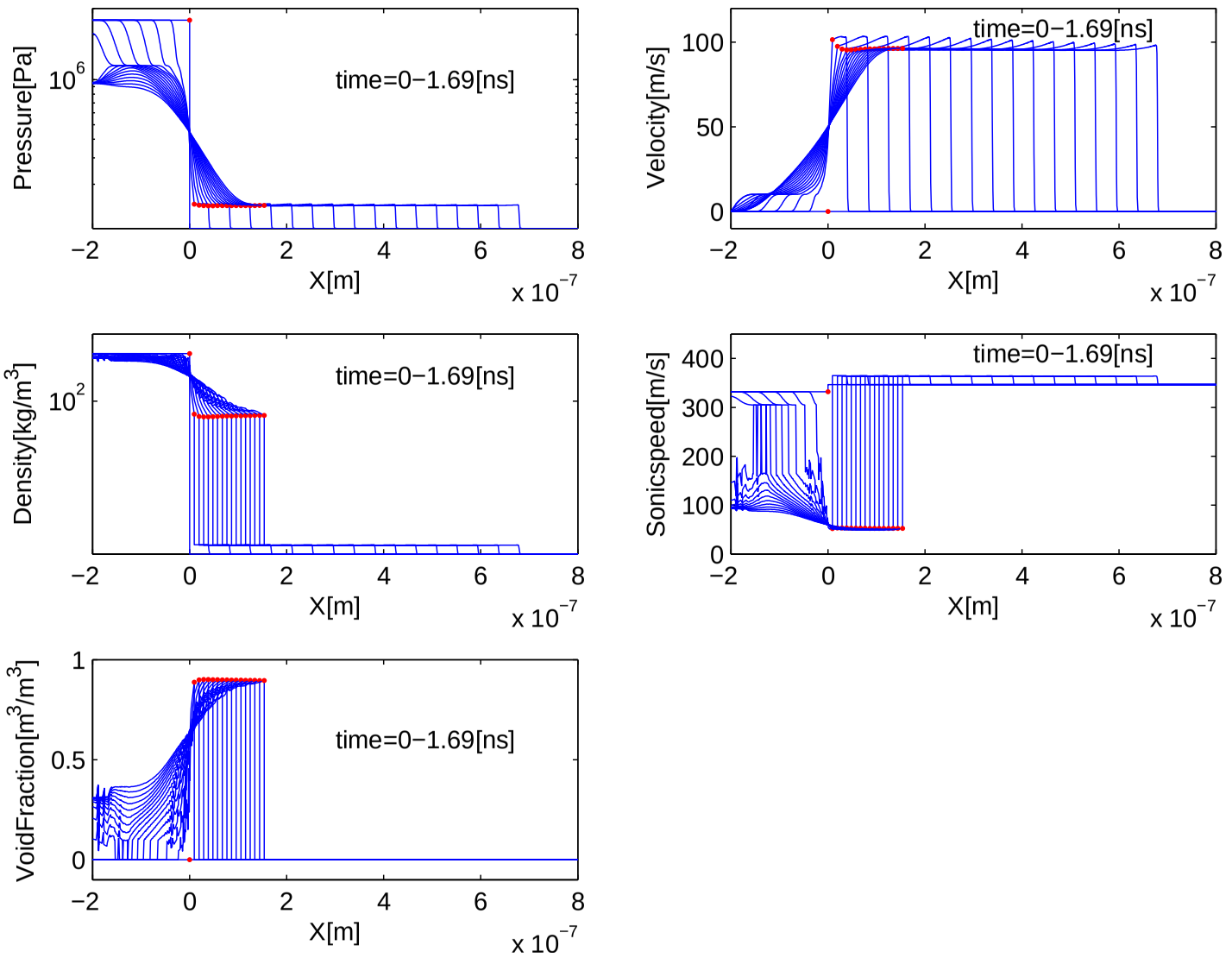

Figure 9.2: Evolution of the profiles: initially saturated pure liquid at 25 bar

the PLG in the simulation has reached the KSL during the depressurisation process, the evaporation wave or the evaporation front is attached to the rarefaction wave. In other words, the dwell time for the onset of the evaporation wave is extremely short in the BLEVE simulation. This difference is determined by the difference in the level of superheat between the BLEVE simulation and the experimental studies in Sec.(2.1.4).

9.3 The shock location and the shock properties

Before the research on the shock properties further proceeds, we need first locate the shock in the air region.

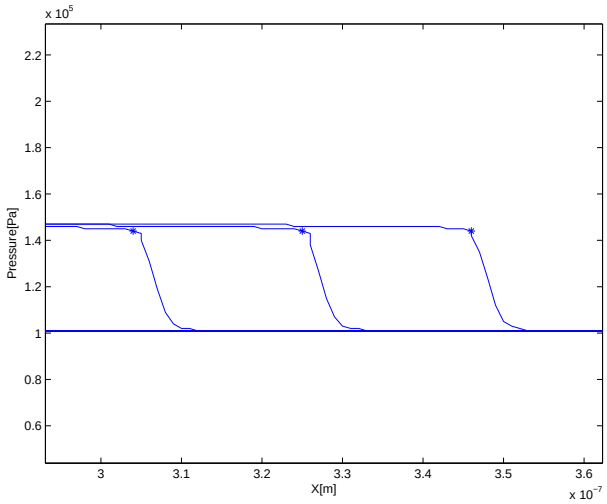

Figure 9.3: Diffused shock with shock locations marked by blue stars

If we zoom in at the front end of the moving air in the pressure profile in Fig.(9.3), we can see that the shock is captured by several particles as a slope instead of a real discontinuity. It is because that that first-order differencing scheme is applied in the particle-path algorithm. The numerical diffusion at the shock location is inevitable, which brings problems to accurately allocate the position of the shock as well as to accurately get the fluid properties there. Although in the research of tunnel safety, the magnitude of the pressure jump at the shock location is more

interesting than the location itself, a criterion to select a representative location for the shock is still essential.

It is known that both the pressure gradient and the velocity gradient at the discontinuity are infinity, therefore we select the location of the particle with the largest velocity spacial gradient referring to its nearest stationary particle in the air region as the representative location of the shock. In Fig.(9.3), those locations are marked with blue stars. From now on, we will use the properties at the shock locations as the properties of the particles that the shock just passed by or the properties of the shock tail particle as introduced in Chpt.(5).

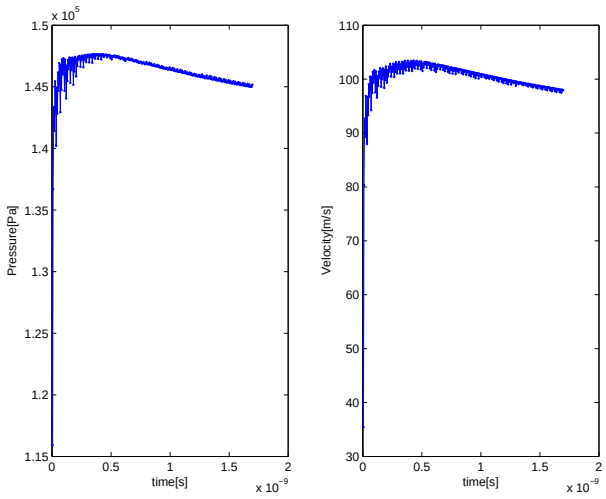

Figure 9.4: The evolution in time of the pressure and the velocity at the shock location

For the case of tank ruptured with 25 bar saturated PLG, the time evolution of the pressure and the velocity at the shock location is demonstrated in Fig.(9.4). The pressure and the velocity at the shock locations demonstrate consistency in their variation. They both quickly jump to relatively high values, then gradually reach their maxima and finally start to decay. The decay of shocks has been well studied in (44) and we will discuss it later.

It should be noted that the shock pressure fluctuates intensively in the early stage as seen in Fig.(9.4). It is neither a numerical effect nor a physical effect, but only caused by the definition of the shock location. As seen in Fig.(9.5), the shock is

gradually being generated after the computation starts. The shock locations, according to our definition, are not stable because the particle with the largest velocity spacial gradient does not locate stably on the shock. Therefore the shock pressures fluctuate intensively. As time passes by, the fluctuation of the shock pressure tends to be stable because the shock profile becomes more and more stable. So the fluctuation in the shock pressure in the early stage is completely caused by the method of data post-processing to obtain the shock properties.

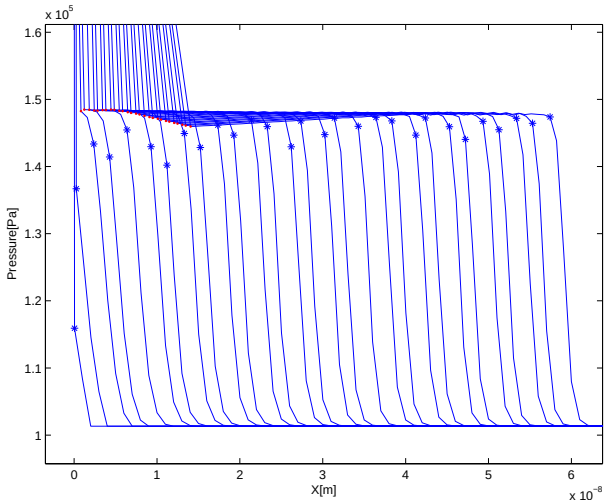

Figure 9.5: The pressure profiles in the early stage, shock locations marked by blue stars

9.4 Minimal pressure needed for BLEVE

From previous computations, we know that the shock can only be generated if the PLG near the contact face vapourises rapidly. This relationship can be used to find out the hazardous initial conditions of the PLG that can generate a shock when the tank ruptures. For each initial pressure, three temperatures are tested, i.e. the normal temperature $T_1 = 298.15\,K$, the saturation temperature $T_2 = T_{sat}(p_0)$ and a temperature close to the kinetic superheat limit temperature of the initial pressure $T_3 = 0.999\,T_{KSL}(p_0)$. For the calculation of T_{KSL}, the reader can refer to Chpt.(6).

The initial conditions and the results are both listed in Tab.(9.1) and plotted in Fig.(9.6). Note: For the cases of initial pressure higher than $32\,bar$, homogeneous bubble nucleation is triggered but the computation for finding the solution of homogeneous bubble nucleation is stuck in dead loop. Adjusting the bracketing method by using finer steps can solve this problem. Since the pressures have been much larger than the design pressure of the tank, we think limiting the initial pressures lower than $31.5\,bar$ is more convenient and practical.

Irrespective of temperature, a shock can only be generated if the initial PLG pressure is higher than $20.5\,bar$ and no shock will be generated if the initial PLG pressure is lower than $20\,bar$. Therefore $20.5\,bar$ is the minimal pressure needed for propane BLEVE surrounded by the ambient air in normal conditions.

Table 9.1: Initial states and shock generation

p_0 $[bar]$	T_1 $[K]$	Shock	$T_2 = T_{sat}(p_0)$ $[K]$	Shock	$T_3 = 0.999 T_{KSL}(T_0)$ $[K]$	Shock
36	298.15	Yes*	360.33	Yes*	361.14	Yes*
34	298.15	Yes*	357.16	Yes*	358.85	Yes*
32	298.15	Yes*	353.85	Yes*	356.66	Yes*
31.5	298.15	Yes	353.00	Yes	356.13	Yes
31	298.15	Yes	352.14	Yes	355.60	Yes
30	298.15	Yes	350.38	Yes	354.55	Yes
29	298.15	Yes	348.59	Yes	353.51	Yes
28	298.15	Yes	346.75	Yes	352.49	Yes
27	298.15	Yes	344.85	Yes	351.48	Yes
26	298.15	Yes	342.92	Yes	350.48	Yes
25	298.15	Yes	340.92	Yes	349.49	Yes
24	298.15	Yes	338.87	Yes	348.51	Yes
23	298.15	Yes	336.75	Yes	347.53	Yes
22	298.15	Yes	334.57	Yes	346.56	Yes
21	298.15	Yes	332.21	Yes	345.59	Yes
20.5	298.15	Yes	331.15	Yes	345.11	Yes
20	298.15	No	329.97	No	344.63	No
19	298.15	No	327.54	No	343.67	No
18	298.15	No	325.03	No	342.71	No
17	298.15	No	322.40	No	341.75	No

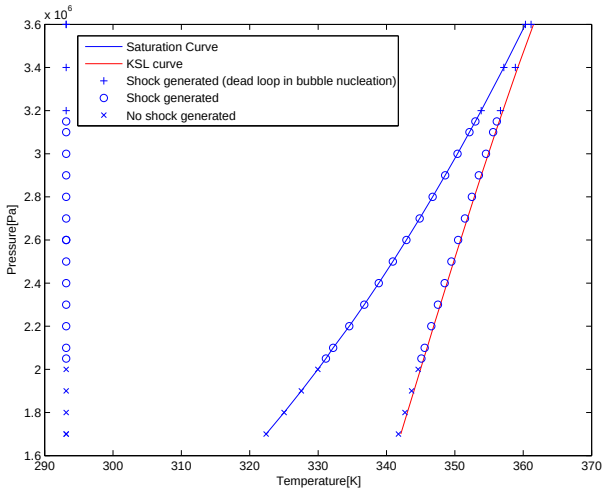

Figure 9.6: The initial conditions of the PLG and the shock generation

9.5 Influence of the initial PLG temperature

In this section, the influence of the initial PLG temperature is investigated. We carry out computations with three initial PLG temperatures listed in Tab.(9.1) for pressure $25\,bar$. The volumes of the PLG in three cases are the same.

- PLG: Propane
- Initial PLG pressure: $p_0 = 25\,bar$
- Case-1 Initial PLG temperature: $T_{0,1} = 293.15\,K = 0.793\,T_c$
- Case-2 Initial PLG temperature: $T_{0,2} = T_{sat}(p_0) = 340.92\,K = 0.922\,T_c$
- Case-3 Initial PLG temperature: $T_{0,3=}0.999\,T_{KSL}(p_0) = 349.49\,K = 0.945\,T_c$

The evolutions of the shock pressure for the three cases are shown in Fig.(9.7). The difference between the results of Case-2 and Case-3 is minor because the difference in the initial temperature is minor, therefore the difference in the initial PLG

states is minor. On the other hand, same initial pressures with similar initial temperatures in Case-2 and Case-3 will result in similar homogeneous bubble nucleation in those two cases, therefore the following vapourisation and expansion of the PLG in Case-2 and Case-3 are taking similar manners. As we observe the contact face pressure evolutions of Case-2 and Case-3 in Fig.(9.8), we can directly draw the conclusion that the contact face pressures also evolves with negligible difference in those two cases. Because the air is 'pushed' by PLG in similar manners, it is not strange that the shocks generated in Case-2 and Case-3 are similar.

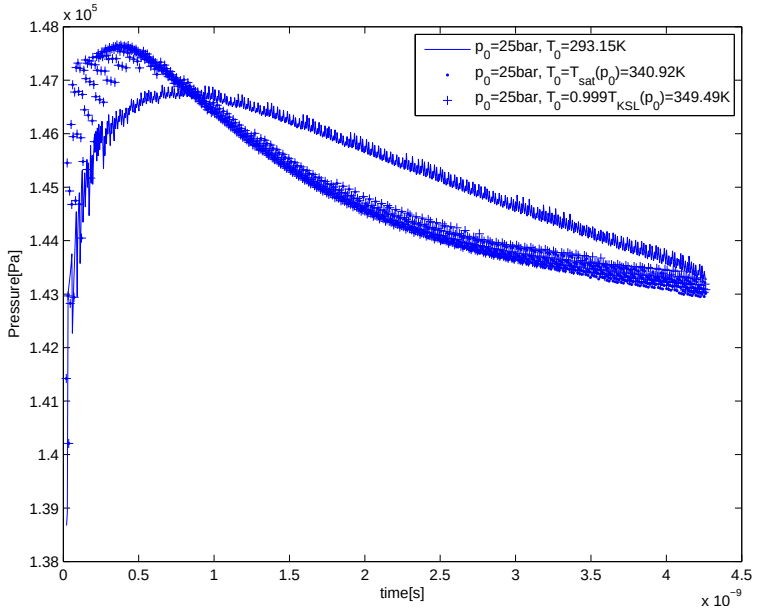

Figure 9.7: The influence of the initial PLG temperature on the time evolution of the shock pressure

If we compare the shock pressure in Case-2 and Case-3 with the one in Case-1, we find in Fig.(9.7) that the shock pressures in the high temperature cases (Case-2 and Case-3) first become higher, then become lower than the one in low temperature case (Case-1) and finally show the trend of becoming higher than the one in low temperature case again. It brings an interesting conclusion on evaluating the shock blast of a BLEVE. When the initial pressures and the volumes of PLG are the same, the dependence of the shock pressure on the the initial PLG temperature

are not as straightforward as we thought: higher initial PLG temperatures result in higher shock pressures. It turns out that there exists a time window (or a spacial window considering the shock propagation in space) in which the shock blast caused by low temperature PLG are stronger than the one caused by high temperature PLG, although the difference is minor in current simulations.

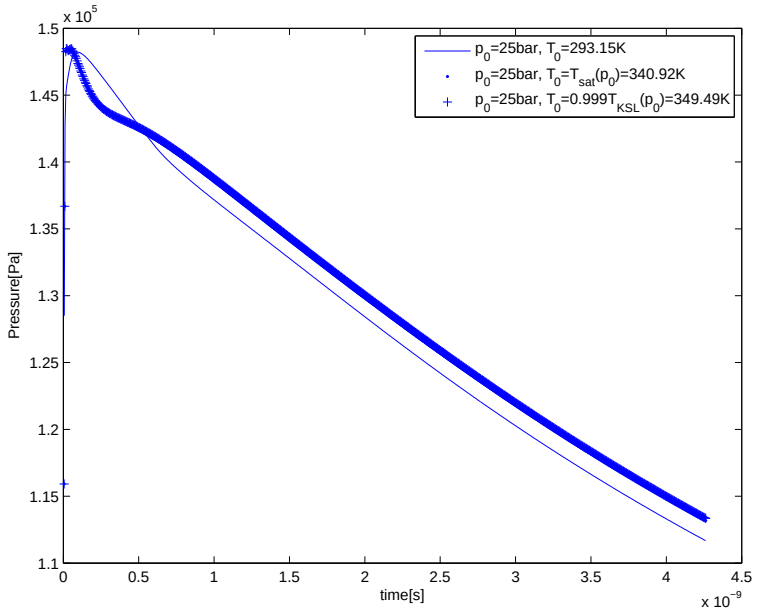

Figure 9.8: The influence of the initial PLG temperature on the time evolution of the contact face pressure

The contact face pressures in Fig.(9.8) and (9.9) show the similar behavior as the shock pressure, but in a faster pace, i.e. the contact face pressures in high temperature cases become lower than the one in low temperature case at about $0.08\,ns$ while for the shock pressure, the time is about $0.8\,ns$; the contact face pressures in high temperature cases become higher than the one in low temperature case at about $0.5\,ns$ while for the shock pressure, it will probably occur after $4.5\,ns$. The positive correlation between the contact face pressure and the shock pressure is confirmed. The variation of the contact face pressure is the cause of the variation of the shock pressure, which also proves that the decay of the shock pressure is not a numerical effect. Otherwise, the decay of the shock pressures in all three cases

will be similar after the shock pressure in high temperatures cases become equal to the one in the low temperature case at about $0.9\,ns$ in Fig.(9.7).

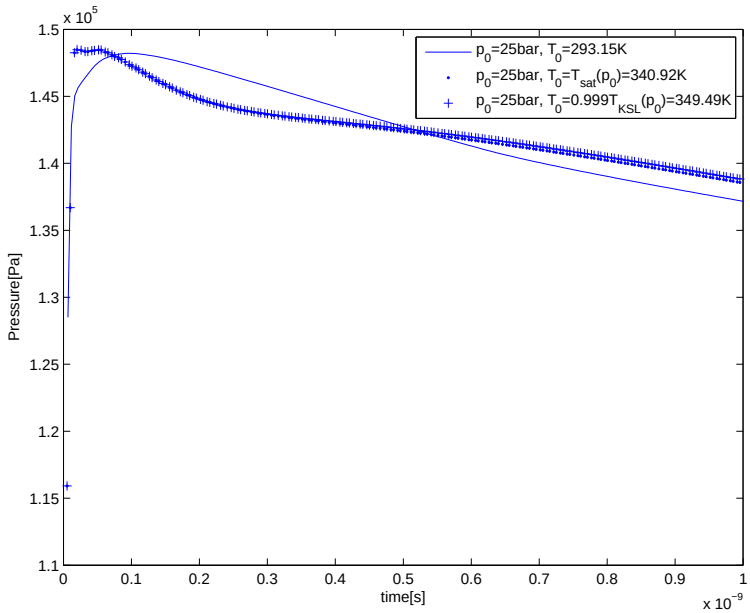

Figure 9.9: The influence of the initial PLG temperature on the time evolution of the contact face pressure, $0-1\,ns$

We also notice in Fig.(9.9) that immediately after the tank ruptures, the contact face pressure drops to about $1.16\,bar$ in high temperature cases while to about $1.28\,bar$ in the low temperature case. So the magnitude of the pressure drop in high temperature cases is larger than the one in the low temperature case, which indicates that a more superheated state is reached in high temperature cases than in the low temperature case. Therefore the vapourisation of the liquid PLG at the contact face proceeds more violently in high temperature cases. Consequently, the contact face pressures in high temperature cases recover to a higher level of approx. $1.48\,bar$, which leads to the generation of a stronger shock in the early stage. A stronger shock will cause the air moving faster to the outlet, leaving larger space for the PLG. When the vapourisation of the contact face PLG is almost done, the contact face pressure in high temperature cases can not sustain a higher level, which could be the reason of the more rapid decay of the contact face pressure

between $0.08-0.2\,ns$ in Fig.(9.9).

9.6 Influence of the initial saturated PLG state

Because the initial PLG temperature has minor influence on the shock pressure, three saturated states of the PLG are chosen for comparing their influences on the shock pressure instead of using three initial PLG pressures at the same temperature. The volumes of the PLG are the same in three cases, therefore the influence of the PLG volume has been excluded.

- PLG: Propane
- Case-1 Initial PLG state: $p_{0,1}=25\,bar$, $T_{0,1}=T_{sat}(p_{0,1})=340.92\,K=0.922\,T_c$
- Case-2 Initial PLG state: $p_{0,2}=28\,bar$, $T_{0,2}=T_{sat}(p_{0,2})=346.75\,K=0.938\,T_c$
- Case-3 Initial PLG state: $p_{0,3}=31\,bar$, $T_{0,3}=T_{sat}(p_{0,3})=352.14\,K=0.952\,T_c$

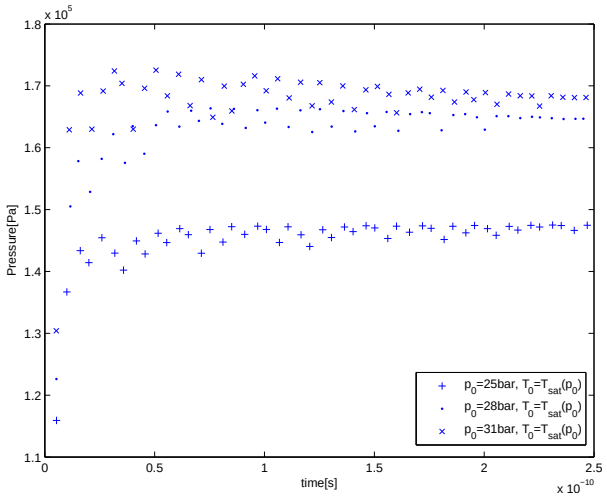

Figure 9.10: The influence of the initial saturated states on the time evolution of the shock pressure: $0-0.25\,ns$

The shock pressures in the early stage $(0-0.25\,ns)$ are shown in Fig.(9.10). One remarkable feature in Fig.(9.10) is that the shock pressure of Case-2 is closer to the shock pressure of Case-3 than to the one of Case-1. This asymptotic behavior is because the saturation point and the KSL are converging to the critical point as the pressure increases. When the PLG state approaches to the critical point, both the difference in the initial states and the difference in homogeneous bubble nucleation start to vanish.

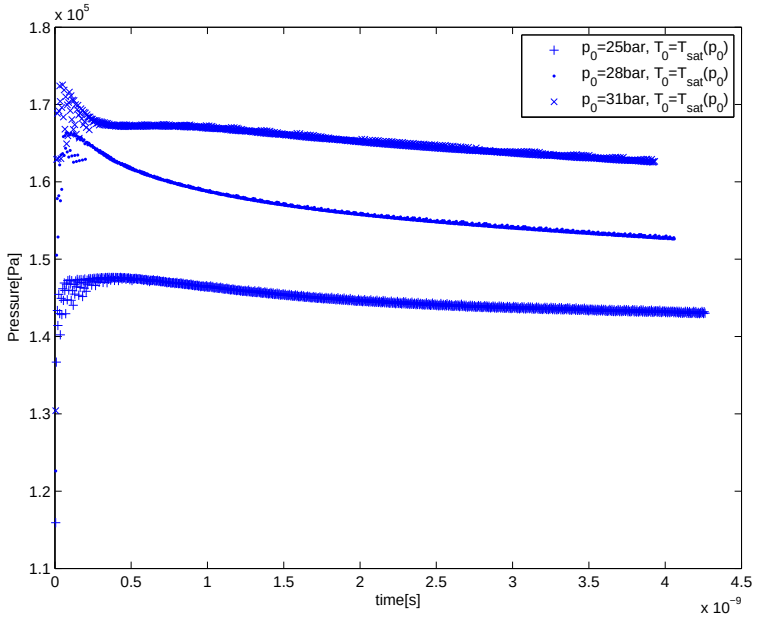

Figure 9.11: The influence of the initial saturated states on the shock pressure

As the computation proceeds in Fig.(9.11), the shock pressure of Case-2 gradually moves to the locations in the middle of the shock pressures of Case-1 and Case-3 representing that the difference in the shock pressure finally becomes proportional to the difference in the initial states, especially the difference in the initial pressures. Comparing the difference in the shock pressure in the concerned temperature range in Fig.(9.7) with the one in the concerned pressure range in Fig.(9.11), we can draw the conclusion that the dependence of the shock pressure on the initial PLG pressure is greater than the one on the initial PLG temperature. Therefore when carrying out the experiments of the BLEVE by rapid depressur-

isation, the initial PLG pressure should be better controlled than the initial PLG temperature.

9.7 Influence of the initial PLG volume

In a real BLEVE, the involved PLG may vary not only in initial state but also in volume before the tank ruptures. In this section, we will discuss the influence of the PLG volume on the shock caused by a BLEVE. In 1D simulation, the volume of the PLG has been changed into the domain length of the PLG. The PLG is initially at the saturated state of $25\,bar$ and three PLG domain lengths are taken for the computation as

- PLG: Propane
- Initial PLG state: $p_0 = 25\,bar$, $T_0 = T_{sat}(p_0) = 340.92\,K = 0.922\,T_c$
- Case-1 PLG domain length: $5\,nm$
- Case-2 PLG domain length: $20\,nm$
- Case-3 PLG domain length: $200\,nm$

Fig.(9.12) shows the pressure evolution at the shock location for the three cases. Note that the plots of Case-2 and Case-3 are overlapped while the computation of Case-3 stops at about $1.7\,ns$ and the computation of Case-2 stops at about $2\,ns$. All shock pressures quickly jump to be greater than $1.4\,bar$ within $0.02\,ns$. Later on, the shock pressures in Case-2 and Case-3 gradually reach the same maxima of approx. $1.475\,bar$ while the one in Case-1 does not. Consequently, the shock pressure in Case-1 starts to decay in a manner completely different from the other two.

If we look at Fig.(9.13) of the pressure evolution at the contact face for the three cases, we can see that the contact face pressure in all cases starts to decrease after jumping to a level of about $1.48\,bar$. The contact face pressure in Case-1 decays much earlier than the others. Before $0.4\,ns$, the contact face pressures in Case-2 and Case-3 and are quite similar to each other. As the result of this similarity, the shock pressures in those three cases remain similar. After $0.4\,ns$ the similarity in the contact face pressures of Case-2 and Case-3 disappears, however it does

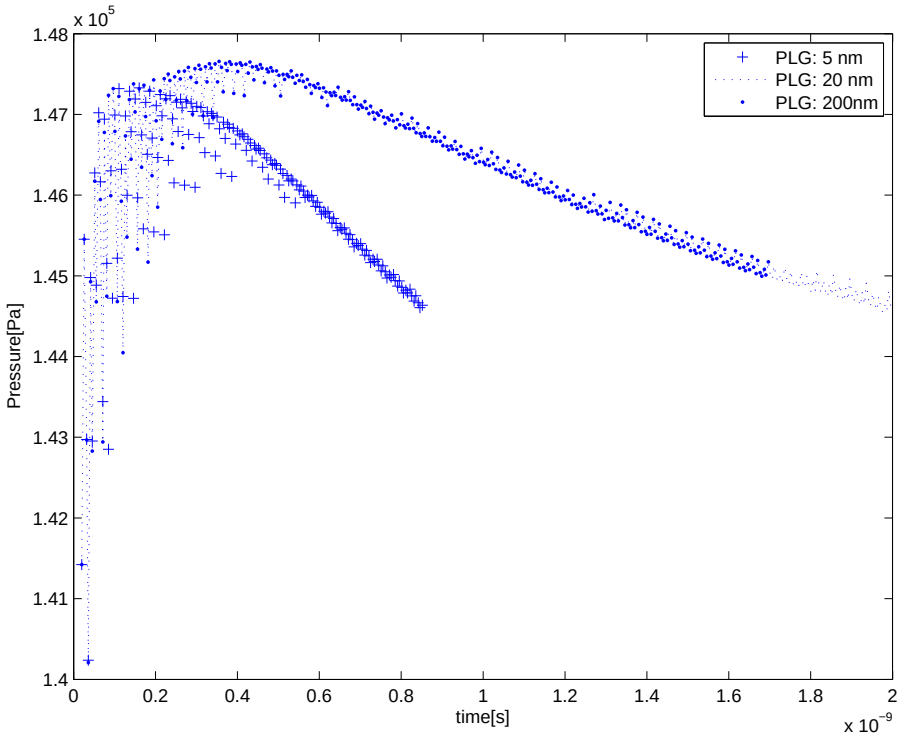

Figure 9.12: Influence of the PLG domain length on the shock pressure

not influence the shock pressures immediately which decay exactly in the same pace until 1.7 ns. From previous discussions, we believe that the vanishing of the similarity in the contact face pressures of Case-2 and Case-3 will eventually make the similarity in the shock pressures vanish.

The similarity and difference in the shock pressures in all three cases can be explained by the existence of the shock generation stage in the beginning of a BLEVE. In the shock generation stage, a pressure wave is gradually developed into a shock. This development relies on the continuous 'pushing' from PLG to the air. If the 'pushing' due to the vapourisation and expansion of PLG can last long enough, a shock is formed. Otherwise the pressure wave generated by the vapourisation and expansion of the PLG will vanish rapidly. For the saturated propane between 25 bar, it seems that 0.4 ns is the duration of the shock generation stage.

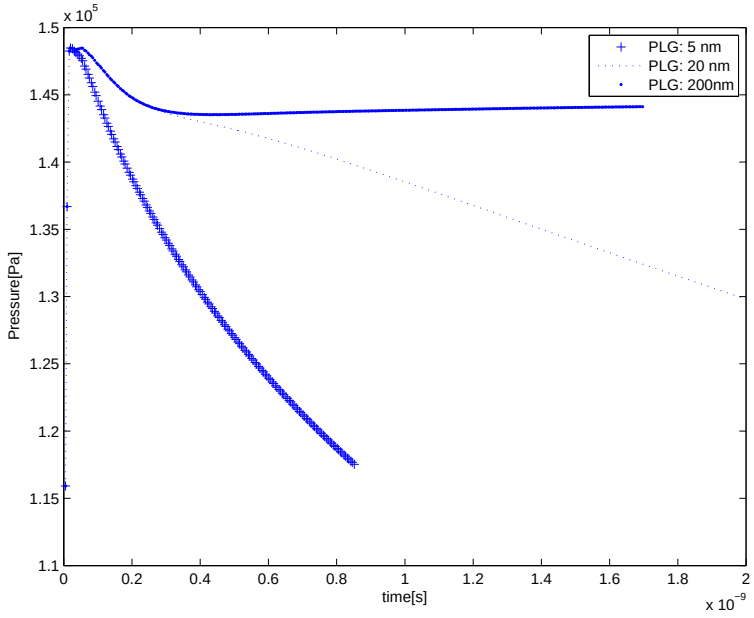

Figure 9.13: The contact face pressure for three PLG domain lengthes

The shock is not fully generated in Case-1 because the PLG volume is so small that the vapourisation and expansion of the bulk PLG is almost over before the shock is generated. In Case-2 and Case-3, the shocks are fully generated and propagate on themselves. The decay of the contact face pressure after the shock generation stage does not influence the shock immediately. On the other hand, although the volume of PLG becomes 10 times larger in Case-3 than in Case-2, the volume increasing does not result in a stronger shock because the shock generation of a BLEVE is mainly due to the vapourisation of the PLG near the contact face. Larger volume (large enough to fully generate a shock) PLG will not lead to a stronger shock, but a higher pressurized air region between the contact face and the shock, which can be proven by the difference in the contact face pressure in Fig.(9.13).

To confirm our analysis, we also carried out computations for the PLG initially at 31 bar saturated state. The PLG domain lengthes are set to be 20 nm and 200 nm respectively. As Fig.(9.14) shows, the evolution of the shock pressure in two cases are overlapped as well and the similarity in the contact face pressure vanishes at about 0.4 ns.

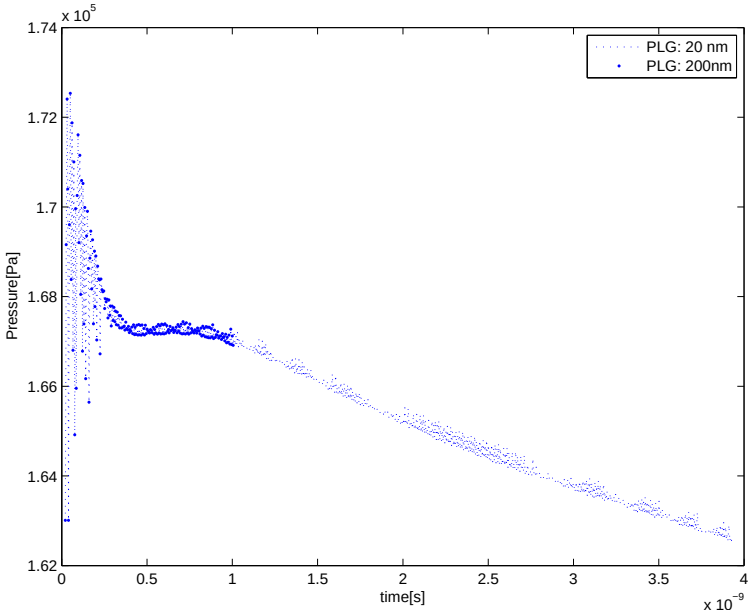

Figure 9.14: Influence of the PLG domain length on the shock pressure with 31 bar initial saturated PLG

The most important conclusion can be drawn here is that the shock is generated by the PLG close to the contact face. In lab-scale experiments or real-scale accidents, the volume of the involved PLG is large enough for the shock to be fully generated. Therefore the maximal shock pressure predicted from small length scale computations in this section can be used for the tunnel safety research in larger scales. This conclusion also matches with the observations from the experimental study of (32) in Sec.(2.2.2) as 'the peak value of the pressure however is practically independent of the mass of liquid.'

CHAPTER 10

MODEL COMPARISONS, CONCLUSIONS AND FUTURE WORK

In this chapter, we give the conclusions on the TUD model developed in this research work as well as on the corresponding numerical simulations. Regarding the TUD model, it is clear that most emphasis should be put on the TUD-NET model because the TUD-RT model is neither a state-of-art model nor a predictive one.

In the next two sections the conclusions on the TUD-NET model and on on the numerical results will be elaborated. First the TUD-NET model will be compared with the TNO model and the Pinhasi et al. model in order to reveal the advantage of the TUD-NET model and to enlighten the direction of further improvements. Next simulation of computational results of the TUD-NET model and the TNO model will be compared. The focus is on the overpressure generated by the shock and the possible impact on the tunnel wall caused by the dynamic pressure of the two-phase mixture in response to the requirements of the tunnel safety research. Advices on the further development of the numerical simulation models will be given as the last and the most important part of this chapter.

10.1 On the TUD-NET model

In this research work, we established the TUD-NET model for the simulation of 1D BLEVE in tunnel geometry including

- the Euler equations for single-phase flow and the Equal-Velocity-Unequal-Temperature Euler equations for two-phase flow from (28);
- the particle-path algorithm for the method of characteristics from (58) (59);
- the Peng-Robinson-Stryjek-Vera equation of state from (84) embedded in the modified StanMix program of FluidProp (19);
- the source term modeling, particularly the bubble nucleation model from (24) for the interfacial area generation, the interfacial area evolution model and the interfacial fluxes model for the liquid-to-vapour phase transition from (43).

10.1.1 Comparison with the TNO model

If compared with the TNO model introduced in Sec.(2.2.2), the TUD-NET model is more advanced in that

- The local thermodynamic properties of the PLG mixture can be numerically solved while in the TNO model the PLG properties must be assumed as spatially uniform;
- Based on the local thermodynamic properties of the PLG mixture, the process of phase transition in the TUD-NET model can be mathematically well defined as a local process rather than being 'assumed to occur with the liquid and vapour at spatially uniform temperature and pressure, decreasing in time, following the saturation curve of the evaporating substance' in the TNO model (96). Therefore using the TUD-NET model, it is possible to demonstrate the relevant phenomena in the PLG region like the decreasing pressure drop following the rarefaction wave and the pressure recovery due to rapid vapourisation of the PLG liquid etc.

10.1.2 Comparison with the Pinhasi et al. model

If compared with the Pinhasi et al. model (58) (59) introduced in Sec.(2.2.2), several improvements and/or modifications have been made in the TUD-NET model as follows

- In some computations of the Pinhasi et al. model, the rarefaction wave propagating into the undisturbed PLG region and the shock wave propagating into the uncompressed air region apparently have been treated as moving boundaries while as demonstrated by the computations presented in this thesis work, the particle-path algorithm for the method of characteristics is capable of automatically generating and capturing the rarefaction wave and the shock wave and the results are satisfactory;

- In the Pinhasi et al. model, the initial state of the PLG was a two-phase mixture with arbitrary low initial void fraction while in the TUD-NET model, bubble nucleation model has been introduced so that the initial state of PLG can be set as pure liquid;

- Pinhasi et al. did not give the exact form of the equation of state they have chosen. In the TUD-NET model, PRSV-EOS in modified StanMix from the thermodynamics library code FluidProp has been adapted for predicting the thermo-physical properties of metastable liquids;

- In the Pinhasi et al. model, the interfacial flux model was derived from the kinetic theory, in which only the temperature was considered as the driven force and the development of interfacial area was not considered. In the TUD-NET model, interfacial flux models are developed from non-equilibrium thermodynamics, in which both the temperature and the pressure can be considered as driven forces (although the assumption of EVUT cancels out the pressure as the driven force) and the evolution of the interfacial area density is taken into account.

10.1.3 Recommendations on the improvements

The TUD-NET model in principle is having the following limitations with related direction of further improvements:

- The method of characteristics can be easily applied for 1D unsteady or 2D steady problems and is difficult to be applied for 2D unsteady problems or for higher dimension problems. At present, the method of characteristics also limits the mesh size of the computational domain and makes its application to large-scale simulations very expensive. In order to fully exploit the benefits of the TUD-NET model a numerical implementation using a finite volume approach is recommended;

- The reliability of a cubic equations of state, including PRSV-EOS, for predicting thermo-physical properties of metastable liquids, especially for highly superheated liquid states, has not been proven;

- In the current bubble nucleation model, bubble nucleation is triggered when the liquid crosses the KSL, which means bubble nucleation will not occur no matter how close the liquid state is to the KSL. This simplification may give the wrong impression that the bubble nucleation rate jumps from zero to an extremely high value at the KSL. The truth is that the bubble nucleation rate slowly increases from a negligible value when the saturated liquid is getting more and more superheated until the KSL is approaching where the bubble nucleation rate tremendously increases from negligible values to extremely high values. So precisely to say, bubble nucleation can occur in any superheated liquid, however for slightly and moderately superheated liquid, the bubble nucleation is too slow or the possibility of bubble generation is too low to be observed. Back to the BLEVE, if the bubble nucleation is too slow compared with the time scale of the fluid motion of PLG after the vessel is totally disintegrated, the bulk liquid will fall onto the ground forming a pool in which flashing instead of BLEVE will occur. This scenario has been excluded in the TUD-NET model and could be of importance in evaluating the hazards of a combination of BLEVE and pool-flashing in future works;

- The model for the evolution of interfacial area density contains a number of assumptions: critical bubbles are assumed to be spherical; the bubble number density is assumed to be constant after bubble nucleation; the influence of flow regimes on the interfacial area density is poorly represented and should be improved in more refined models;

- In the interfacial fluxes model, the curvature effect of the interface has been ignored. The model guarantees the heat and mass fluxes are conserved

through the interface, but the exact values still need to be calibrated by other means such as molecular dynamics simulations;

10.2 On the simulation results of the TUD-NET model

The simulations in Chpt.(9) using the TUD-NET model allow to make the following conclusions

- Whether or not homogeneous bubble nucleation is triggered or equivalently whether or not the PLG state has crossed its KSL during the early stage of the tank rupture can be used as a quick check for BLEVE occurrence. Applying this general principle it can be concluded that if a tank containing saturated liquefied propane is ruptured at its design pressure (17.7 bar), no BLEVE will occur since homogeneous bubble nucleation as the necessary condition for BLEVE will not be triggered.
- There exists a minimal pressure for each PLG below which no BLEVE will occur. For propane, this value is 20.5 bar according to our simulation;
- The dependence of the shock pressure on the initial PLG temperature in a BLEVE is not straightforward: higher initial PLG temperature results in higher shock pressure, which is true in most of the time for two BLEVEs with the same PLG involved but at two different temperatures. However there exists a time window in which the shock blast caused by low temperature PLG are stronger than the one caused by high temperature despite the minor influence of the initial PLG temperature on the shock pressure.
- In general, the dependence of the shock pressure on the initial PLG pressure is larger than the one on the initial PLG temperature. Therefore when carrying out the experiments of the BLEVE by rapid depressurisation, the initial PLG pressure should be better controlled than the initial PLG temperature;
- The shock is generated by the PLG close to the contact face. The maximal shock pressure obtained from small scale computations or experiments is also meaningful for large-scale experiments or real-scale accidents.

Although these conclusion are drawn from one-dimensional simulations they are believed to be of general validity either because they concern the evolution in state

space (thermodynamics) or they are dominated by phenomena close to the contact face.

The TUD-NET model differs from the Pinhase et al. model and from the TNO model and it is of interest compare the predictions of the models in specific test cases. Since the code developed by Pinhasi et al. is not available, and some relevant model details have not been described in the literature, as described in the previous section, a direct comparison of predictions of Pinhasi model and the TUD-NET model was not possible. Instead, here some conclusions will be presented of a comparison of the numerical simulations results of the TNO model and the TUD-RT and TUD-NET models. For the simulations of the TNO model use was made of a computer code made available by B. van den Berg (TNO). The comparison between the TNO model and the TUD-RT model has been first presented in the project report Ref. (52). In that report the TUD-RT model is called CBB-model, referring to committee 'Commissie Bijzondere Belastingen' executing the project. The author of this thesis was member of the CBB. The results of the TUD-NET model are published here for the first time and provide more information on the degree in which the TNO model is overpredicting the peak pressure.

10.2.1 Comparison with the TNO model

As introduced in Chpt.(2), Van den Berg et al. (91, 92, 94) have developed the TNO model for the prediction of BLEVE blasts. For a description of the model which is more detailed than the one given in Chpt.(2), we refer to M.M. van der Voort et al. (2012). According to the underlying assumptions, the TNO model is regarded as the most conservative one, giving the largest maximum pressure possibly generated by a BLEVE. It is of interest for us and for the users of the TNO model to compare the shock blasts predicted by the TUD models with the ones by the TNO model in order to evaluate the consequences of the conservative assumptions made in the TNO model.

It has been noticed in experiments and simulations carried out by TNO that in certain circumstances also the expanding two-phase mixture can arrive at the tunnel wall and generate severe impact on the tunnel wall (52). In 1D BLEVE, this impact will be experienced by the downstream objects including vehicles and human beings. Therefore, it is of interest to evaluate, in addition to the blast overpressure in the air region, also the maximum PLG dynamic pressure at the contact face as predicted by the two models.

10.2.2 The blast overpressure in the air region

In 2009, the first comparison was carried out. At that time, the TUD-NET model was not completed yet and only results of the TUD-RT model were published in the final project report (52). Here, after the presentation of the TUD-RT model, also the results of the TUD-NET model will be reported. The TNO model and the TUD-RT model both have been applied to a 1-dimensional simulation of a BLEVE of PLG (propane) at saturated states of $18\,bar$ and $25\,bar$. The maximum blast overpressures predicted by both models have been compared in Table (10.1). The term 'overpressure' refers to the relative pressure difference compared to the ambient pressure. The blast overpressure, in our calculation, is the shock pressure minus $1\,atm$.

Propane	The TNO model	The TUD-RT model	
Initial state (bar, K)	Max. blast overpressure (bar)	Max. blast overpressure (bar)	Relaxation time (s)
18 325	3.8	3.0	2×10^{-5}
25 341	4.7	3.4	2×10^{-5}

Table 10.1: Comparison of the maximum blast overpressure predicted for a 1-dimensional configuration by the TNO model and the TUD-RT model

The computations of a 1-dimensional situation using both the TNO model and the TUD-RT model have shown that the TNO model predicts the higher pressures, in agreement with the conservative model assumptions. The height of the pressure peak becomes larger when PLG is at initially higher pressure/temperature along the saturation curve. This trend is well predicted by both models.

The calculation using the TUD-RT model has been done using an assumed value of the relaxation time of $2\times10^{-5}\,s$. The time scale was chosen so short in order to create a conservative estimate in line with the assumptions underlying the TNO model. In the presence of a short relaxation time, the differences in the predictions between both models then mainly result from the differences in dealing with the rapid depressurisation process of the liquid. The TNO model uses a global temperature and pressure decrease. The TUD-RT model is local and predicts the pressure profile in the liquid-vapour mixture. Apart from the initial pressure decrease it describes also the subsequent reversal of the pressure evolution or the pressure

recovery because of the fast generation of vapour.

If the predictions from the TUD-NET model are added, the conservative nature of the TNO model becomes more obvious as demonstrated in Table (10.2). It also turns out that according the TUD-NET model the relaxation time value of $2\times10^{-5}\,s$ used in the application of the TUD-RT model is too small for a BLEVE of saturated liquid propane at $25\,bar$. To have agreement between TUD-RT model and TUD-NET model a larger relaxation time would have to be used in the TUD-RT model.

Propane	The TNO model	The TUD-RT model	The TUD-NET model
Initial state (bar, K)	Max. blast overpressure (bar)	Max. blast overpressure (bar)	Max. blast overpressure (bar)
18 325	3.8	3.0	No shock
25 341	4.7	3.4	0.47

Table 10.2: Comparison of the maximum blast overpressure predicted for a 1-dimensional configuration by the TNO model, the TUD-RT model and the TUD-NET model

In fact, the TNO model and the TUD-NET model are equivalent in the simulation of the gas dynamics of the single-phase air, which means giving the same contact face properties as the boundary conditions, the shock generation and propagation predicted by the TNO model and the TUD-NET model should be similar. It is the differences in dealing with thermodynamics of the two-phase PLG that make the shocks predicted by two models widely different. The TNO model, not taking into account rate of phase change limitations, represents the largest amount of energy released in the fastest pace which leads to the maximum overpressure compatible with the aerodynamics described by the Euler equations.

10.2.3 The PLG dynamic pressure at the contact face

The predictions of the TNO model and the TUD-NET model for the evolution of the PLG dynamic pressure at the contact face have been compared to each other in four cases as given below

- PLG: Propane

- PLG domain length: $20\,nm$
- Case-1 Initial PLG state: $p_0 = 22\,bar$, $T_0 = T_{sat}(p_0)$
- Case-2 Initial PLG state: $p_0 = 25\,bar$, $T_0 = T_{sat}(p_0)$
- Case-3 Initial PLG state: $p_0 = 28\,bar$, $T_0 = T_{sat}(p_0)$
- Case-4 Initial PLG state: $p_0 = 31\,bar$, $T_0 = T_{sat}(p_0)$

The reader should note that the PLG dynamic pressure p_{CM}^{dyn} is taking the value of $\frac{1}{2}\rho_m u_m^2$ from the PLG mixture properties.

As shown in Fig.(10.1), the development of the contact face dynamic pressure predicted by the TUD-NET model looks familiar, starting with a rapid increase then continuously decreasing. The higher the initial saturated PLG pressure, the higher the jump in the contact face dynamic pressure and the faster the following decrease. If a real tunnel is considered, the downstream objects will be less impacted by the expanding two-phase mixture involved in a BLEVE if it is further away from the ruptured tank according to the TUD-NET model.

However the situation is different according to the TNO model. The contact face dynamic pressure starts with a period with oscillations but rapidly evolves to a constant value. The oscillation in every prediction of the TNO model is caused by the numerical method and parameter settings (Flux-correct transport algorithm) applied in that model. the fact that the TNO model gives a constant contact face dynamic pressure, which means the downstream objects will suffer the same impact no matter how far they are away from the ruptured tank. This is the result in a Cartesian one-dimensional simulation. In case of an expansion in higher dimensions there will be a decay for geometric reasons. Here we compare 1D simulations representative for phenomena close to the contact phase or for evolution along the length of a tunnel.

The constant contact face dynamic pressure comes from the assumption made in the TNO model: the vapourisation of the bulk PLG in reaction to the depressurisation is instantaneous and strong enough to counterbalance the pressure drop, therefore the contact face dynamic pressure (and the contact pressure) can maintain a constant value. Another direct evidence of this assumption in the TNO model is the independence of the contact face dynamic pressure on the PLG volume. As demonstrated in Fig.(10.2), the evolution of the contact face dynamic

pressure are exactly the same in the computations with three initial PLG volumes ($5\,nm$, $20\,nm$ or $200\,nm$).

Apart from some initial moments, in the computed short time interval the TNO model gives higher contact face dynamic pressure than the TUD-NET model. This confirms the conservative nature of the TNO model. However it is not known from the current simulation results how the dynamic pressure predicted by the TUD-NET model evolve over a longer time interval. The proof of accuracy of the model and its application to larger time intervals and spatial domains remains a topic for further studies.

10.2.4 Suggestions for future work

The first priority for future work regarding the numerical simulation of BLEVE is model validation. As far as we know, there were no adequate and complete data sets that can be directly used to validate the TUD-NET model for 1D BLEVE. For example, Edwards and O'brien conducted very good experiments on rapid depressurisation of water, but no air is involved (63). Simões-Moreira and Shepherd may get the dodecane highly superheated, but there was no data of the compressed air, let alone the shock that could be possibly generated (80). Gelfand et al. measured the shock generated by sudden expansion of hot water, but the data sets were too few (32). Different from the tunnel geometry we are concerned with, most medium-scale or large-scale BLEVE experiments were carried out in open space (10).

TNO has sufficient data on BLEVE in urban tunnel geometry (92, 93, 94). So a recommended approach for model validation is to upgrade the TUD-NET model for 3D problems or implement the source term models of the TUD-NET model in a mature 3D solver and validate the 3D model with the TNO experimental data.

If the validation must be carried out for the 1D TUD-NET model, it is suggested that

- Shock tube is chosen as the main part of the test rig as introduced in (32, 63, 80). Nowadays a fast-opening valve may replace the piecing mechanism (a bullet or an arrow against a rupture diaphragm) to simulate the sudden tank rupture. By controlling the exposure of PLG to the ambient air, the repeatability of experiments is definitely increased. The opening of the fast-open

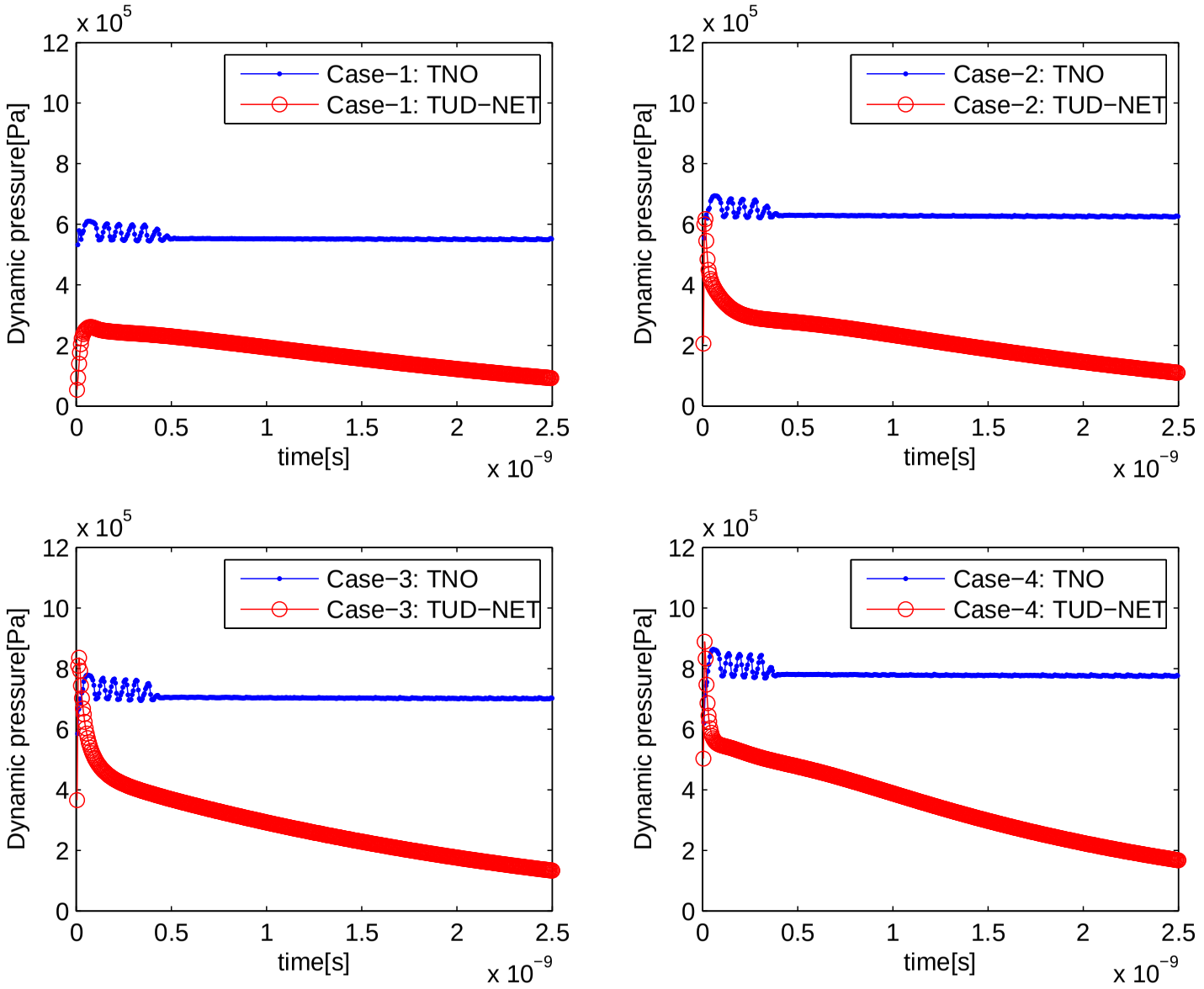

Figure 10.1: The dynamic pressure at the contact face by the TNO model and the TUD-NET model

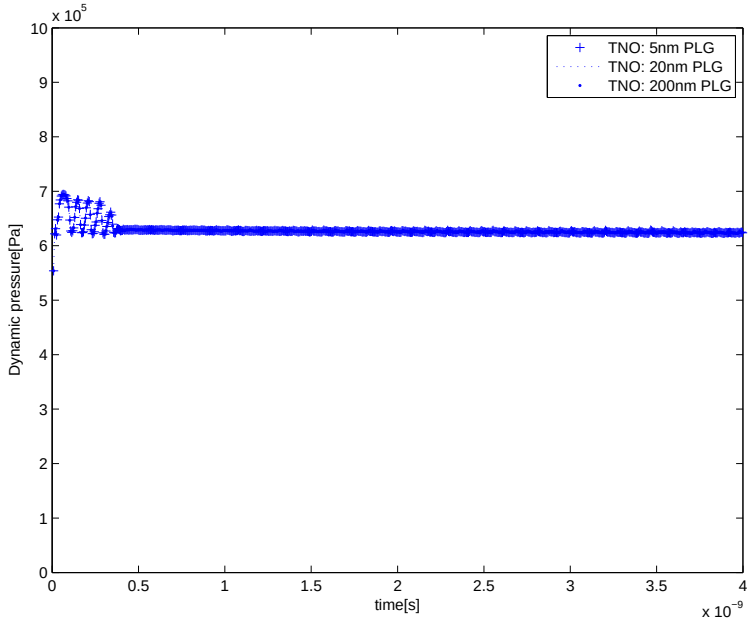

Figure 10.2: The independence of the contact face dynamic pressure on the PLG volume by the TNO model

valve should disturb the PLG as least as possible because the disturbance will entrain the air into PLG and those air bubbles will act as nuclei for heterogeneous nucleation;

- Most PLG ever used in previous experiments e.g. propane, dodecane, carbon-dioxide, nitrogen, ethanol and Freon-113 have been included in StanMix of FluidProp. It is highly recommended to compute the KSL curve of each PLG and make sure the PLG state will cross the KSL curve during the rapid depressurisation process. Caution should be used when the flammable fluids are being operated;

- The pressure and temperature sensors should be evenly placed on the shock tube and simultaneously record the data so the history of pressure and temperature profiles can be obtained. The transient void growth as an important parameter can be measured by X-ray absorption technique (63);

- The inner surface of the shock tube should be fine polished to suppress heterogeneous nucleation on the wall. Using adiabatic wall is also helpful to suppress heterogeneous nucleation.

As the first step of the model validation process, it might be proper to exclude the air and start with PLG in shock tube only. An experiment similar to the blowdown experiments in (63) is recommended. The target is to quantitatively describing the phenomena that occurs in PLG including the speed of the rarefaction wave, the onset of the vapourisation and the relationship between the dwell time and the liquid superheat, the number density of the bubble nuclei and their growth rate etc, among which an important parameter that can be used to calibrate the numerical model is the pressure undershoot or the pressure drop after the rarefaction wave. This parameter represents the superheat that PLG can reach during depressurisation. The fast-opening valve in lab-scale experiments should generate pressure undershoots close to the most probable pressure undershoot in real BLEVEs.

When the investigation on PLG is done, the contact face can be introduced as the second step of the model validation process. In current TUD model, it is assumed that the contact face will act as 'a piston' and no heat transfer occurs between PLG and the air. On the other hand, the 'piston' assumption also cancels out the air entrainment and PLG splashing through the contact face. This assumption may have some unknown prerequisites and its influence can not be estimated based on our current knowledge. It is expected that the 'piston' assumption is an acceptable approximation when PLG gets highly superheated and the vapourisation of PLG is much faster than the heat and mass transfer through the interface.

The last step of the model validation is on the hazard of a BLEVE, including but not limited to the shock and the dynamic impact caused by the expanding mixtures. This part of work, as the output of the previous two steps, is indeed the final judgement to the overall model. The experimental data is easy to obtain while the challenge lie in addressing the cause of the deviating of the predictions from the experimental data.

NOMENCLATURE

Roman

A	Cross-sectional area of a tunnel
A_b	Surface area of a bubble
A_i	Interfacial area density
A_{int}	Interfacial area
a	Sonic speed
f	Fugacity
G_T	Derivative of the Gibbs free energy to the temperature
g	Gravitational acceleration
h	Enthalpy
J	Mass flux through the interface
J_{cbn}	Critical bubble nucleation rate
J_i	Conjugate fluxes in non-equilibrium thermodynamics
J_q	Total heat flux through the interface
$J_q^{'g}$	Measurable heat flux from the vapour into the interface
$J_q^{'l}$	Measurable heat flux from the liquid into the interface
$\mathbb{K}$	Boltzmann constant
L_{ij}	Phenomenological coefficients in non-equilibrium thermodynamics
M	Mass
m	Mass flux
m_1	Mass of one single molecule
N	Number of molecules
$\mathbb{N}$	Number density of molecules
N_b	Total number of bubbles
N_d	Total number of droplets
n_b	Number density of bubbles
n_d	Number density of droplets

p	Pressure
$\dot{p}$	Decompression rate
p_e	Equilibrium vapour pressure
p_{CM}^{dyn}	PLG dynamic pressure at the contact face
Q	Heat
q	Heat flux
$\mathbb{R}$	Universal gas constant
r^*	Critical bubble radius
r_b	Radius of a spherical bubble
s	Entropy
T	Absolute temperature
$\dot{T}$	Temperature increase rate
T^s	Interfacial temperature
t	Time
$t_{i,k}$	Relaxation time for phase k
u	Velocity
u_s	Shock speed
V	Volume, $[m^3]$
V_b	Volume of a bubble
v	Specific volume
v_M	Molar volume
v_{mp}	The most probable thermal velocity
W_{min}	Minimum work to form one bubble
W_{min}^*	Minimum work to form one critical bubble
X_i	Forces in non-equilibrium thermodynamics
x	Longitudinal coordinate of a tunnel
Z	Altitude of a tube or a tunnel
$\mathbb{Z}$	Compressibility factor

Greek

α	Void fraction
α_l	Volume fraction of liquid
α_g	Volume fraction of gas or vapour
α_s	Constant in the expression of J_{cbn} in the Delale et al. 2003 model
γ	Heat capacity ratio
Δt	Time step
ΔH_{vap}	Latent heat
δ	Poynting correction factor
κ_D	Substance dependent constant in the Delale et al. 2003 model
κ, κ_0	Polynomial fit of the acentric factor in PR-EOS and its modified versions
κ_1	Adjustable pure component parameter in PRSV-EOS
μ	Chemical potential
ρ	Density
σ	Surface tension
σ_c	Condensation coefficient
σ_s	Local entropy production rate
τ_D	Constant in the Delale et al. 2003 model
τ	Friction force
ω	Acentric factor in equation of state

Superscripts

0	Initial state
KSL	Kinetic superheat limit
l	Liquid
g	Vapour or gas

Subscripts

0	Initial state
a	Air
b	Bubble
CM	Mixture side of the contact face
CA	Air side of the contact face
c	Critical point
d	Droplet
g	Gas or vapour
i	Interface between the liquid and the vapour in two-phase mixture
k	Phase indicator, l for liquid and g for gas or vapour
L	Left
l	Liquid
m	Two-phase mixture
w	Wall
R	Right
r	Reduced values, e.g. reduced temperature or reduced pressure
sat	Saturated state
Y	Mass fraction

Abbreviations

BFP	Boiling front propagation
BLEVE	Boiling Liqid Expanding Vapour Explosion
C+, C-	Characteristics of waves in method of characteristics
CBB	Commissie Bijzondere Belastingen
C_i	C-coefficients in characteristic form of the Euler equations
CNT	Classical nucleation theory
CO_2	Carbon dioxide
EOS	Equation of state
EVET	Equal-velocity-equal-temperature assumption
EVUT	Equal-velocity-unequal-temperature assumption
KNT	Kinetic nucleation theory
KSL	Kinetic superheat limit
LPC	Low pressure chamber
LI	Liquid under investigation
HPV	High pressure volume
NEMD	Non-equilibrium molecular dynamics
PLG	Pressure Liquefied Gas
PP	Characteristics of particle-path in method of characteristics
PP-MOC	Particle-path algorithm of the method of characteristics
PR-EOS	Peng-Robinson equation of state
PRMC-EOS	Peng-Robinson-Mathias-Copeman equation of state

PRSV-EOS	Peng-Robinson-Stryjek-Vera equation of state
RK-EOS	Redlich-Kwong equation of state
SMD	Sauter mean diameter
SRK-EOS	Soave-Redlich-Kwong equation of state
TRK-EOS	Twu-Redlich-Kwong equation of state
TSL	Thermodynamic superheat limit
vdW-EOS	van der Waals equation of state
VLE	Vapour-liquid-equilibrium

Summary

The risk of explosion due to rupture of a tank filled with pressurized liquefied gas (PLG) is one of the risks to be considered in the context of studies on tunnel safety. When a vessel containing liquid well above its boiling point at normal atmospheric pressure fails catastrophically a Boiling Liquid Expanding Vapour Explosion (BLEVE) can occur. A vessel containing a liquefied gas can rupture due to the consequences of mechanical impact and or external fire. Because at ambient pressure the thermodynamic equilibrium state of LPG is the gaseous state, after the sudden depressurisation caused by the vessel rupture a rapid vapourisation takes place possibly leading to blast waves propagating in the surroundings and possibly damaging the tunnel wall and tunnel structure.

The topics of investigation in this thesis are the rapid vapourisation, immediately following rapid depressurisation, and the creation of an overpressure close to the tank. These phenomena can be described using thermodynamics and fluid dynamics. The objective of the investigation was to formulate and solve a physics-based model that can be used to predict whether or not a BLEVE will occur and to predict the strength of the shock waves when a BLEVE occurs.

In order to create an adequate model for BLEVE simulation the following steps were taken. An appropriate simplified form of the conservation equations of mass, momentum and energy was formulated. The flow of the rapidly vapourising liquid was described by the Equal-Velocity-Unequal-Temperature (EVUT) formulation of the Euler equations for two-phase flow. The flow of the surrounding air was described by the single phase Euler equations. In order to have to possibility to study in detail the coupling of thermodynamic and gas dynamic phenomena the flow was restricted to be one-dimensional. This is adequate to represent local phenomena in the direction orthogonal to a PLG/air interface or global phenomena in a tunnel geometry. Because of the short time scale of the phenomena to be described it can be assumed that there is no mass transfer at the interface between the two-phase liquid+vapour region and the air region (the contact face). A numerical scheme for the solution of the model equations of two-fluid two-phase compressible flow was formulated. Because of the restriction to one-dimensional flow the method of characteristics could be selected as solution algorithm. It was solved by the particle-path algorithm, both in the single phase region and the two phase region. An advanced cubic equation of state (EOS) was chosen to describe the relations between the relevant thermodynamic variables. The domain of ap-

plication of the EOS was extended to the description of metastable states, such as superheated liquid, occurring during a BLEVE. Models were formulated for mass, momentum and heat transfer between liquid and vapour phase. Two types of heat and mass transfer models were used: a qualitative model based on the concept of a relaxation time, and a quantitative model using the concepts and formalism of non-equilibrium thermodynamics (NET). To describe the initiation of the rapid vapourisation a homogeneous nucleation model was used. The transfer models provide the source terms due to vapourisation appearing in the momentum and energy equations of the EVUT Euler equations. The two models developed in this way, the TUD-RT model when a relaxation time is used, and the TUD-NET model, when non-equilibrium thermodynamics is used, were solved for scenario's of starting from different initial temperature and pressure of propane. The role of the TUD-RT model is mainly to demonstrate the dependence of shock strength on several parameters, but is cannot be a predictive model because the relaxation time has to be assumed. The TUD-NET model on the other hand can be expected to be predictive because it incorporates the fundamental physical phenomena in the vapourising liquid.

The simulations by the TUD-NET model reveal that homogeneous bubble nucleation is the trigger of BLEVE. For each PLG, there is a minimal pressure needed for BLEVE, below which homogeneous bubble nucleation will not occur. In case of a BLEVE, the shock is mainly generated by PLG close to the PLG-air contact face and once the shock is generated, it will propagate along the tunnel in a pace faster than the expansion of the rest PLG mixture. Hence the vapourisation of the rest of the PLG has no direct influence on the shock generated in the surrounding air. But it will contribute to the dynamic pressure of the expanding two-phase PLG mixture. Both the impact of the shock in air and of the impact of the expanding two-phase mixture can lead to damage to the tunnel wall or objects in the tunnel.

Compared to another simulation model using the EVUT Euler equations - the Pinhasi et al. model - , the TUD-NET model offers the following advantages i) a predictive model for homogeneous bubble nucleation is included. This makes it possible to predict the onset of BLEVE in an accident involving PLG tank rupture; ii) the interfacial fluxes model is based on non-equilibrium thermodynamics taking both the chemical driven force and the thermal driven force for the interfacial heat and mass transfer into account.

Compared to a simpler simulation model - the TNO model -, the TUD-NET model predicts weaker shock blast and the dynamic impact of the two-phase mixture

than the TNO model confirming the role of the TNO model as the most conservative model for BLEVE simulation. The combination of the simulation tools developed in this study with simulation tools for tank rupture and tunnel response provide a comprehensive simulation tool for estimating the consequences of PLG-tank rupture in a tunnel. Implementation of the TUD-NET model in a numerical solver of the three-dimensional Euler equations is needed for further validation of the model and for application to analysis of real BLEVE events, and is recommended.

Samenvatting

Het risico van een explosie ten gevolge van het openscheuren van een vat of tank gevuld met door drukverhoging vloeibaar gemaakt gas (pressurized liquefied gas (PLG)) is een van de risico's die beschouwd moeten worden in de context van studies over tunnelveiligheid. Wanneer een vat dat een vloeistof bevat bij een druk die aanmerkelijk hoger is dan het kookpunt bij normale atmosferisch druk op catastrofale wijze bezwijkt, kan er een 'Boiling Liquid Expanding Vapour Explosion (BLEVE)' optreden. Een vat dat een vloeibaar gemaakt gas bevat kan scheuren door de gevolgen van een mechanische inslag of door een externe brand. Omdat bij omgevingsdruk de thermodynamische evenwichtstoestand een gasvormige toestand is treedt bij een plots wegvallen van de druk veroorzaakt door het openbreken van het vat een snelle verdamping op, die mogelijkerwijs kan leiden tot drukgolven die zich voortplanten in de omgeving en mogelijkerwijs de tunnelwand en de tunnelstructuur kan beschadigen.

De onderwerpen van het onderzoek in dit proefschrift zijn de snelle verdamping onmiddellijk volgend op het wegvallen van de druk en de creatie van een overdruk dicht bij het vat. Deze verschijnselen kunnen beschreven worden met gebruikmaking van thermodynamica en vloeistofdynamica. Het doel van het onderzoek was om een op natuurkundige wetten gebaseerd model te formuleren en op te lossen, dat kan voorspellen of een BLEVE wel of niet zal optreden en wat de sterkte is van de schokgolven bij het optreden van een BLEVE.

Om een adequaat model voor simulatie van een BLEVE te creëeren werden de volgende stappen genomen. Een gepaste vereenvoudigde vorm van de behoudswetten voor massa, impuls en energie werd geformuleerd. De stroming van de snel verdampende vloeistof werd beschreven met een vorm van de Euler vergelijkingen voor twee-fasen stroming, namelijk het Gelijke-Snelheid-Ongelijke-Temperatuur (Equal-Velocity-Unequal-Temperature (EVUT)) model. De stroming van de omgevingslucht werd beschreven door de Euler vergelijkingen voor een-fase stroming. Om de mogelijkheid te hebben om de koppeling van thermodynamische een gasdynamische verschijnselen in detail te bestuderen werd de stroming beperkt tot één-dimensionaal. Dit is geschikt om lokale verschijnselen te representeren in de richting loodrecht op het scheidingsvlak tussen PLG en lucht of globale verschijnselen in een tunnel geometrie. Omwille van de korte tijdschaal van de verschijnselen die beschreven moeten worden, kan aangenomen worden dat er geen massaoverdracht is op het grensvlak tussen het gebied met twee-fasen, vloeistof

en damp, en het gebied met lucht (het contactvlak). Er werd een numeriek oplossingsschema geformuleerd voor de modelvergelijkingen voor samendrukbare twee-fasen stroming. Omwille van de beperking tot één -dimensionale stroming kon de methoden der karakteristieken gekozen worden als oplossingsalgoritme. Dit werd opgelost met de deeltjes-pad algoritme, zowel in het een-fase gebied als in het twee-fasen gebied. Voor de beschrijving van de verbanden tussen de relevante thermodynamische variabelen werd gekozen voor een geavanceerde kubische toestandsvergelijking (Equation of State, EOS). Het toepassingsgebied van de EOS werd uitgebreid tot de beschrijving van metastabiele toestanden, die optreden tijdens een BLEVE. Modellen werden geformuleerd voor overdracht van massa, impuls en warmte tussen de vloeistof- en de dampfase. Er werd gebruik gemaakt van twee types van modellen voor warmte en massa overdracht: een kwalitatief model gebaseerd op het begrip van relaxatietijd, en een kwantitatief model gebruik makend van concepten en formalisme van de niet-evenwichts thermodynamica (NET). Om de initiatie van de snelle verdamping beschrijven werd gebruik gemaakt van een model voor homogene nucleatie. De overdrachtsmodellen leveren de bronterm ten gevolge van verdamping die optreden in de EVUT Euler impuls en energie vergelijking. De twee modellen die op deze manier ontwikkeld werden, het TUD-RT model wanneer gebruik gemaakt wordt van een relaxatietijd, en het TUD-NET model wanneer niet-evenwichtsthermodynamica wordt gebruikt, werden opgelost voor scenario's uitgaand van verschillende begintemperatuur en -druk van propaan. De rol van het TUD-RT model is voornamelijk het demonstreren hoe de schoksterkte afhangt van verschillende parameters, maar het kan geen voorspellend model zijn omdat de waarde van de relaxatietijd verondersteld moet worden. Van het TUD-NET model daarentegen kan verwacht worden dat het voorspellend is, omdat het fundamentele fysische verschijnselen in de verdampende vloeistof incorporeert.

De simulaties met het TUD-NET model brengen aan het licht dat homogene bel-nucleatie de 'onsteker' is van een BLEVE. Voor elk LPG is er een minimale waarde van de druk waaronder homogene bel-nucleatie niet zal optreden. In het geval van een BLEVE, wordt de schok voornamelijk gegenereerd door het LPG dat zich dicht bij het PLG-lucht contact vlak bevindt en eens de schok gegenereerd is, zal hij zich voortplanten aan een tempo groter dan de expansie van de rest van het PLG mengsel. De verdamping van de rest van het LPG heeft geen directe invloed op de schok gegenereerd in de omgevingslucht. Maar zij zal wel bijdragen aan de dynamische druk van het expanderende twee-fasen LPG mengsel. Zowel de impact van de schok in de lucht als de impact van het expanderende twee-fasen

mengsel kan leiden tot schade aan de tunnel wand als aan objecten in de tunnel.

In vergelijking met een andere simulatiemodel gebruikmakend van de EVUT Euler vergelijkingen - het Pinhasi et al. model - biedt het TUD-NET model de volgende voordelen: i) het bevat een voorspellend model voor homogene bel-nucleatie. Dit maakt het mogelijk het starten van een BLEVE in een ongeval met breuk van een PLG tank te voorspellen; ii) het model voor de fluxen aan het scheidingsvlak tussen de twee fasen is gebaseerd op niet-evenwichtsthermodynamica, en brengt zowel de chemische drijvende kracht als de thermische drijvende kracht voor de warmte- en massoverdracht aan het grensvlak in rekening.

In vergelijking met een eenvoudiger simulatiemodel - het TNO model - voorspelt het TUD-NET model een zwakkere schokgolf en dynamische impact van het tweefasen mengsel dan het TNO model, en is hiermee de rol van het TNO model als meest conservatieve model voor BLEVE simulatie bevestigd. De combinatie van de simulatietechnieken die in deze studie zijn ontwikkeld met simulatietechnieken voor tankbreuk en met simulatietechnieken voor tunnelrespons, leveren een alomvattende simulatietechniek voor het schatten van de gevolgen van de breuk van een LPG-tank in een tunnel. Implementatie van het TUD-NET model in een computer programma voor oplossing van de driedimensionale Eulervergelijkingen is nodig voor verdere validatie van het model en voor toepassing van de analyse op reële BLEVE's, en is aanbevolen.

Acknowledgements

At the point of finishing this thesis work, I would like to take this opportunity to show my sincere gratitude to my promotor, Prof.dr. D.J.E.M. Roekaerts for offering me this valuable opportunity to work on this PhD project. I benefited a lot from his expertise in reactive flows and explosions and tremendous discussions between us. I would like to thank him for the support and encouragement that he gave to me in my four-year life in the Netherlands. I am indebted to him for providing me with valuable guidance in every stage of the writing of this thesis.

I am sincerely grateful to Dr. G.A. Pinhasi (Flow-sim Ltd., Israel) for the fruitful discussion with me on WCCM8 and ECCOMAS 2008 in Venice. He clarified lots of doubts and questions in my brain at that time which results in great progress in my research. I would like to give my appreciation to Dr. Piero Colonna for sharing the precious source code of FluidProp/Stanmix with me and ing. Teus van der Stelt for assisting me in solving many practical problems in the adaption of StanMix to metastable states. I am also thankful to Prof. D. Bedeaux (Norwegian University of Science and Technology) and Prof.dr.ing. S.H. Kjelstrup for their kind guidance to me on non-equilibrium thermodynamics. I would like to thank Mr. A.C. van den Berg and Dr. J. Weerheijm from TNO for their valuable advice, kind cooperation and active support to me in participating the project of 'Tunnel Safety'.

I would like to give my appreciation to the colleagues of the Department of Multi-Scale Physics, TUDelft, especially Prof.dr.ir. H.E.A. Van den Akker, Prof.dr.ir. C.R. Kleijn, Prof.dr. R.F. Mudde, Dr. E.H. van Veen, Dr.ir. M. Tummers, Dr. E. Oldenhof, Mr. Z. Saladi and Mr. A. Toader. I am also thankful to my Chinese friends who made my personal life in the Netherlands colorful and wonderful. They are Mr. Chen Hui, Dr. Zhu Xuan, Dr. Chen Yue, Ms. Yang Huiling, Dr. Bi Yu, Mrs. Xiang Yang, Mrs. Shan Xuming, Dr. Mo Liantong, Dr. Xu Qiang, Dr. Gu Lei, Ms. Tang Yao, Dr. Xu Min, Ms. Bai Yuqian and Mr. Yang Xiaogang.

I am deeply grateful to my parents for their love and trust over the years. Without their encouragement and support, I can not imagine myself to go this far in the academic field. I appreciate my beloved Wang Yi for her sacrifice, understanding and love.

Xie Mengmeng
Wuxi, China
March 2013

Bibliography

[1] T. Abbasi and S. A. Abbasi. Accidental risk of superheated liquids and a framework for predicting the superheat limit. Journal of Loss Prevention in the Process Industries, 20(2):165–181, 2007.

[2] T. Abbasi and S. A. Abbasi. The boiling liquid expanding vapour explosion (BLEVE): Mechanism, consequence assessment, management. Journal of Hazardous Materials, 141(3):489–519, 2007.

[3] T. Abbasi and S. A. Abbasi. The boiling liquid expanding vapour explosion (BLEVE) is fifty ... and lives on! Journal of Loss Prevention in the Process Industries, 21(4):485–487, 2008.

[4] Md. Alamgir, C. Y. Kan, and J. H. Lienhard. An experimental study of the rapid depressurization of hot water. Journal of Heat Transfer, 102(3):433–438, 1980.

[5] Md. Alamgir and J. H. Lienhard. Correlation of pressure undershoot during hot water depressurization. Journal of Heat Transfer, 103(1):52–55, 1981.

[6] A. A. Avdeev and Y. B. Zudin. Inertial-thermal governed vapor bubble growth in highly superheated liquid. Heat and Mass Transfer/Waerme- und Stoffuebertragung, 41(10):855–863, 2005.

[7] C. T. Avedisian. The homogeneous nucleation limits of liquids. Journal of Physical and Chemical Reference Data, 14(3):695–729, July 1985.

[8] M. R. Baer and J. W. Nunziato. A two-phase mixture theory for the deflagration-to-detonation transition (ddt) in reactive granular materials. International Journal of Multiphase Flow, 12(6):861–889, 1986.

[9] R. Barbone. Explosive boiling of a depressurized volatile liquid. Master's thesis, Department of Mech. Eng., McGill University, Canada, 1994.

[10] A. M. Birk, C. Davison, and M. Cunningham. Blast overpressures from medium scale BLEVE tests. Journal of Loss Prevention in the Process Industries, 20(3):194–206, 2007.

[11] D. Bjerketvedt, K. Egeberg, W. Ke, A. Gaathaug, K. Vaagsaether, and S.H. Nilsen. Boiling liquid expanding vapour explosion in CO2. Small scale experiments. Energy Procedia, 4:2285–2292, 2011.

[12] M. Blander and J. L. Katz. Bubble nucleation in liquids. AIChE Journal, 21(5):833–848, 1975.

[13] Christopher E. Brennen. Cavitation and Bubble Dynamics (Oxford Engineering Science Series). Oxford University Press, USA, 1995.

[14] J. Casal and J. M. Salla. Using liquid superheating energy for a quick estimation of overpressure in BLEVEs and similar explosions. Journal of Hazardous Materials, 137(3):1321–1327, 2006.

[15] S. Chen, J. Sun, and W. Wan. Boiling liquid expanding vapor explosion: experimental research in the evolution of the two-phase flow and overpressure. Journal of Hazardous Materials, 156(1-3):530–537, 2008.

[16] S. N. Chen, J. H. Sun, and G. Q. Chu. Small scale experiments on boiling liquid expanding vapor explosions: vessel over-pressure. Journal of Loss Prevention in the Process Industries, 20(1):45–51, 2007.

[17] Moon-Sun Chung, Keun-Shik Chang, and Sung-Jae Lee. Numerical solution of hyperbolic two-fluid two-phase flow model with non-reflecting boundary conditions. International Journal of Engineering Science, 40(7):789–803, 2002.

[18] P. Cleaver, M. Johnson, and B. Ho. A summary of some experimental data on LNG safety. Journal of Hazardous Materials, 140(3):429–438, 2007.

[19] P. Colonna and T. P. van der Stelt. Fluidprop: a program for the estimation of thermo physical properties of fluids, Energy Technology Section, Delft University of Technology, The Netherlands, (http://www.fluidprop.com), 2004.

[20] Daniel A. Crowl. Understanding Explosions (A CCPS Concept Book). Wiley-AIChE, 2003.

[21] P. K. Das, G. S. Bhat, and V. H. Arakeri. Investigations on the propagation of free surface boiling in a vertical superheated liquid column. International Journal of Heat and Mass Transfer, 30(4):631–638, 1987.

[22] E. M. De Sá, E. Meyer, and V. Soares. Adiabatic nucleation in the liquid-vapor phase transition. Journal of Chemical Physics, 114(19):8505–8510, 2001.

[23] Pablo G. Debenedetti. Metastable Liquids. Princeton University Press, 1996.

[24] C. F. Delale, J. Hruby, and F. Marsik. Homogeneous bubble nucleation in liquids: The classical theory revisited. Journal of Chemical Physics, 118(2):792–806, 2003.

[25] P. Deligiannis and J. W. Cleaver. The role of nucleation in the initial phases of a rapid depressurization of a subcooled liquid. International Journal of Multiphase Flow, 16(6):975–984, 1990.

[26] P. Deligiannis and J. W. Cleaver. Influence of surrounding bubbles on the rate of nucleation. International Journal of Heat and Mass Transfer, 36(15):3697–3701, 1993.

[27] E. Elias and M. Shusser. Lifetime of a superheated liquid. Heat and Mass Transfer/Waerme- und Stoffuebertragung, 42(1):51–55, 2005.

[28] R. L. Ferch. Method of characteristics solutions for non-equilibrium transient flow-boiling. International Journal of Multiphase Flow, 5(4):265–279, 1979.

[29] D. L. Frost. Dynamics of explosive boiling of a droplet. Physics of Fluids, 31(9):2554–2561, 1988.

[30] D. L. Frost, R. Barbone, and J. Nerenberg. Small scale BLEVE tests with refrigerant-22. Report of the Mc Gill University, Montreal, to the Transportation development centre, Safety and Security, Transport Canada, TP 12123E, December 1995 (available on internet), 1995.

[31] D. L. Frost and B. Sturtevant. Effects of ambient pressure on the instability of a liquid boiling explosively at the superheat limit. Journal of Heat Transfer, 108(2):418–424, 1986.

[32] B. Gelfand, S. Medvedev, A. Polenov, and S. Tsyganov. Shock waves by sudden expansion of hot liquid. In 7th Int. Symp. Loss Prevention and Safety Promotion in the Process Industries, volume 2. European Federation of Chemical Engineering, 1992. paper 89, 15 pages.

[33] H. Giesbrecht, K. Hess, W. Leuckel, and B. Maurer. Analysis of explosion hazards on spontaneous release of inflammable gases into the atmosphere - 1. propagation and deflagration of vapour clouds on the basis of bursting tests on model vessels. German Chemical Engineering, 4(5):305–314, 1981.

[34] Ruud Glas. Kokende-vloeistof-dampexpansie-explosies en toestandsvergelijkingen, 2009.

[35] E. Hahne and G. Barthau. Evaporation waves in flashing processes. International Journal of Multiphase Flow, 26(4):531–547, 2000.

[36] O. E. Ivashnev. Specific features of the modeling of boiling-fluid flows. Fluid Dynamics, 43(3):390–401, 2008.

[37] D. M. Johnson and M. J. Pritchad. Large scale experimental study of boiling liquid expanding vapour explosions (BLEVEs). In Gastech 90, 14th Int. LNG/LPG conference and exhibition, 1990.

[38] M. Karl, A. Gross, L. Pirjola, and C. Leck. A new flexible multicomponent model for the study of aerosol dynamics in the marine boundary layer. Tellus, Series B: Chemical and Physical Meteorology, 63(5):1001–1025, 2011.

[39] J. L. Katz and M. D. Donohue. A kinetic approach to homogeneous nucleation theory. Advances in Chemical Physics, 40(137), 1979.

[40] J. L. Katz and H. Wiedersich. Nucleation theory without maxwell demons. Journal of colloid and interface science, 61(2):351–355, 1977.

[41] M. H. Kim, J. Pettersen, and C. W. Bullard. Fundamental process and system design issues in CO2 vapor compression systems. Progress in Energy and Combustion Science, 30(2):119–174, 2004.

[42] M. E. Kim-E and R. C. Reid. Rapid depressurization of hot, high pressure liquids or supercritical fluids, 1983.

[43] Signe Kjelstrup and Dick Bedeaux. Non-Equilibrium Thermodynamics Of Heterogeneous Systems (Series on Advances in Statistical Mechanics). World Scientific Publishing Company, 2008.

[44] Peter D. Lax. The formation and decay of shock waves. The American Mathematical Monthly, 79(3):227–241, 1972.

[45] O. Le Métayer, J. Massoni, and R. Saurel. Modelling evaporation fronts with reactive riemann solvers. Journal of Computational Physics, 205(2):567–610, 2005.

[46] S. Lesin, A. Baron, H. Branover, and J. C. Merchuk. Experimental studies of direct contact boiling at the superheat limit. High Temperature, 31(6):866–884, 1993.

[47] I. R. M. Leslie and A. M. Birk. State of the art review of pressure liquefied gas container failure modes and associated projectile hazards. Journal of Hazardous Materials, 28(3):329–365, 1991.

[48] S. C. Lin. Cylindrical shock waves produced by instantaneous energy release. Journal of Applied Physics, 25(1):54–57, 1954.

[49] H. Mccann, L. J. Clarke, and A. P. Masters. An experimental study of vapour growth at the superheat limit temperature. International Journal of Heat and Mass Transfer, 32(6):1077–1093, 1989.

[50] C. A. McDevitt, C. K. Chan, F. R. Steward, and K. N. Tennankore. Initiation step of boiling liquid expanding vapour explosions. Journal of hazardous materials, 25(1-2):169–180, 1990.

[51] J. McGarry. Correlation and prediction of the vapor pressures of pure liquids over large pressure ranges. Industrial and Engineering Chemistry Process Design and Development, 22(2):313–322, 1983.

[52] D.J. Molenaar, J. Weerheijm, A. Vervuurt, H. Burggraaf, D. Roekaerts, and P. Meijers. Bijzondere belastingen in tunnels: eindrapport. Technical report, Delft Cluster, 2009.

[53] T. Neuhaus, A. Schaffrath, and E. Altstadt. Development and validation of the pressure surge computer code DYVRO mod. 3. Kerntechnik, 73(5-6):221–225, 2008.

[54] D. W. Oxtoby. Homogeneous nucleation: Theory and experiment. Journal of Physics: Condensed Matter, 4(38):7627–7650, 1992.

[55] D. Y. Peng and D. B. Robinson. A new two-constant equation of state. Industrial and Engineering Chemistry Fundamentals, 15(1):59–64, 1976.

[56] R. J. Peterson, S. S. Grewal, and M. M. El-Wakil. Investigations of liquid flashing and evaporation due to sudden depressurization. International Journal of Heat and Mass Transfer, 27(2):301–310, 1984.

[57] G. A. Pinhasi. Source Term Modeling of Gas and Liquid Release from Breached Pressure Vessel. PhD thesis, Tel-Aviv University, 2001.

[58] G. A. Pinhasi, A. Dayan, and A. Ullmann. Numerical model for boiling liquid vapor explosion (BLEVE). In AIAA Paper, pages 1820–1830, 2004.

[59] G. A. Pinhasi, A. Ullmann, and A. Dayan. 1D plane numerical model for boiling liquid expanding vapor explosion (BLEVE). International Journal of Heat and Mass Transfer, 50(23-24):4780–4795, 2007.

[60] E. Planas-Cuchi, J. M. Salla, and J. Casal. Calculating overpressure from bleve explosions. Journal of Loss Prevention in the Process Industries, 17(6):431–436, 2004.

[61] A. Prosperetti and M. S. Plesset. Vapour-bubble growth in a superheated liquid. Journal of Fluid Mechanics, 85(pt 2):349–368, 1978.

[62] Richard W. Prugh. Quantitative evaluation of 'BLEVE' hazards. Journal of Fire Protection Engineering, 3(1):9–24, 1991.

[63] Edwards A. R. and O'Brien T. P. Studies of phenomena connected with the depressurization of water reactors. Journal of British Nuclear Energy Society, 9(2):125–135, 1970.

[64] R. R. Al-Khoury, J. Weerheijm, K. Dingerdis, and L.J. Sluys. An adaptive time integration scheme for blast loading on a saturated soil mass. Computers and Geotechnics, 2011.

[65] O. Redlich and J. N. S. Kwong. On the thermodynamics of solutions. V: An equation of state. fugacities of gaseous solutions. Chemical reviews, 44(1):233–244, 1949.

[66] D. Reguera, J. M. Rubí, and J. M. G. Vilar. The mesoscopic dynamics of thermodynamic systems. Journal of Physical Chemistry B, 109(46):21502–21515, 2005.

[67] R. C. Reid. Superheated liquids. American Scientist, 64(2):146–156, 1976.

[68] R. C. Reid. Possible mechanism for pressurized-liquid tank explosions or BLEVE's. Science, 203(4386):1263–1265, 1979.

[69] Robert Reid, Bruce E. Poling, and John M. Prausnitz. The Properties of Gases and Liquids. McGraw-Hill Companies, 4th edition, 1987.

[70] Robert C. Reid, John M. Prausnitz, and Thomas K. Sherwood. Properties of Gases and Liquids (McGraw-Hill chemical engineering series). McGraw-Hill Book Company, 3rd edition, 1977.

[71] P. Reinke and G. Yadigaroglu. Explosive vaporization of superheated liquids by boiling fronts. International Journal of Multiphase Flow, 27(9):1487–1516, 2001.

[72] J. R. Riznic and M. Ishii. Bubble number density and vapor generation in flashing flow. International Journal of Heat and Mass Transfer, 32(10):1821–1833, 1989.

[73] A. Røsjorde, D. W. Fossmo, D. Bedeaux, S. Kjelstrup, and B. Hafskjold. Nonequilibrium molecular dynamics simulations of steady-state heat and mass transport in condensation. I. Local equilibrium. Journal of colloid and interface science, 232(1):178–185, 2000.

[74] R. Saurel, F. Petitpas, and R. Abgrall. Modelling phase transition in metastable liquids: Application to cavitating and flashing flows. Journal of Fluid Mechanics, 607:313–350, 2008.

[75] D. Saury, S. Harmand, and M. Siroux. Experimental study of flash evaporation of a water film. International Journal of Heat and Mass Transfer, 45(16):3447–3457, 2002.

[76] D. Saury, S. Harmand, and M. Siroux. Flash evaporation from a water pool: Influence of the liquid height and of the depressurization rate. International Journal of Thermal Sciences, 44(10):953–965, 2005.

[77] S. A. Schubach and D. F. Bagster. Some aspects of modelling steam explosions. Journal of Loss Prevention in the Process Industries, 9(3):193–197, 1996.

[78] J. E. Shepherd and B. Sturtevant. Rapid evaporation at the superheat limit. Journal of Fluid Mechanics, 121:379–402, 1982.

[79] E. Sher, T. Bar-Kohany, and A. Rashkovan. Flash-boiling atomization. Progress in Energy and Combustion Science, 34(4):417–439, 2008.

[80] J. R. Simões-Moreira and J. E. Shepherd. Evaporation waves in superheated dodecane. Journal of Fluid Mechanics, 382:63–86, 1999.

[81] G. Soave. Improvement of the Van Der Waals equation of state. Chemical Engineering Science, 39(2):357–369, 1984.

[82] G. A. Sod. A survey of several finite difference methods for systems of nonlinear hyperbolic conservation laws. Journal of Computational Physics, 27(1):1–31, 1978.

[83] J. Stawczyk. Experimental evaluation of LPG tank explosion hazards. Journal of Hazardous Materials, 96(2-3):189–200, 2003.

[84] R. Stryjek and J. H. Vera. PRSV: An improved Peng-Robinson equation of state for pure compounds and mixtures. The Canadian Journal of Chemical Engineering, 64(2):323–333, 1986.

[85] Geoffrey Taylor. The formation of a blast wave by a very intense explosion. i. theoretical discussion. Proceedings of the Royal Society A, 201:159–174, 1950.

[86] I. Tiselj and S. Petelin. Modelling of two-phase flow with second-order accurate scheme. Journal of Computational Physics, 136(2):503–521, 1997.

[87] Eleuterio F. Toro. Riemann Solvers and Numerical Methods for Fluid Dynamics: A Practical Introduction. Springer, 2 edition, 1999.

[88] C. H. Twu, D. Bluck, J. R. Cunningham, and J. E. Coon. A cubic equation of state with a new alpha function and a new mixing rule. Fluid Phase Equilibria, 69(C):33–50, 1991.

[89] C. H. Twu, J. E. Coon, and J. R. Cunningham. A new generalized alpha function for a cubic equation of state part 2. redlich-kwong equation. Fluid Phase Equilibria, 105(1):61–69, 1995.

[90] E. Valero and I. E. Parra. Reactor pressure analysis at the initial stage of a loss of coolant accident. Annals of Nuclear Energy, 30(5):585–601, 2003.

[91] A. C. van den Berg. Blast charts for explosive evaporation of superheated liquids. Process Safety Progress, 27(3):219–224, 2008.

[92] A. C. van den Berg, M. M. van der Voort, J. Weerheijm, and N. H. A. Versloot. Expansion-controlled evaporation: A safe approach to BLEVE blast. Journal of Loss Prevention in the Process Industries, 17(6):397–405, 2004.

[93] A. C. van den Berg, M. M. van der Voort, J. Weerheijm, and N. H. A. Versloot. BLEVE blast by expansion-controlled evaporation. Process Safety Progress, 25(1):44–51, 2006.

[94] A. C. van den Berg and J. Weerheijm. Blast phenomena in urban tunnel systems. Journal of Loss Prevention in the Process Industries, 19:598–603, 2006.

[95] M. M. van der Voort, A. C. van den Berg, P. C. J. de Bruijn, and P. G. A. van Ierschot. BLEVE-blast experimenten. Briefrapportage aan het Ministerie van Verkeer en Waterstaat. Technical report, TNO, 2004.

[96] M. M. van der Voort, A. C. van den Berg, D. J. E. M. Roekaerts, M. Xie, and P. C. J. de Bruijn. Blast from explosive evaporation of carbon dioxide: Experiment, modeling and physics. Shock Waves, 22(2):129–140, 2012.

[97] M. Volmer and A. Weber. Keimbildung in Übersättigten Gebilden. Zeitschrift für Physikalische Chemie, 119:277–301, 1926.

[98] H. Wiedersich and J. L. Katz. The nucleation of voids and other irradiation-produced defect aggregates. Advances in Colloid and Interface Science, 10(1):33–71, 1979.

[99] W. S. Winters Jr. and H. Merte Jr. Experiments and nonequilibrium analysis of pipe blowdown. Nuclear Science and Engineering, 69(3):411–429, 1979.

[100] J. Xu, S. Kjelstrup, D. Bedeaux, A. Røsjorde, and L. Rekvig. Verification of Onsager's reciprocal relations for evaporation and condensation using non-equilibrium molecular dynamics. Journal of Colloid and Interface Science, 299(1):452–463, 2006.

[101] T. Ytrehus. Molecular-flow effects in evaporation and condensation at interfaces. Multiphase Science and Technology, 9(3):205–327, 1997.

About the author

Mengmeng Xie was born on July 23, 1977 in Qingzhou, Shandong Province, China. He spent his childhood there and moved to Qingdao with his parents in 1987. He graduated from Qingdao No.2 Middle School of Shandong Provice in 1996 and studied Thermal Energy Engineering in Tongji University, Shanghai. During his study, Xie received the People's scholarship for three times and the Professional scholarship for one time. He obtained Bachelor degree of Engineering in 2000.

After his study, Xie worked as technical engineer at Tsingtao Brewery Group and after-sales engineer at Maersk Container Industri Qingdao Ltd. for four years before starting his overseas study and research. In 2004-2006, he took the International Master Programme in Chalmers University of Technology, Sweden and obtained his Master degree in Computational and Experimental Turbulence in 2006.

In 2006-2011, Xie conducted his PhD research in the section Reactive Flows and Explosions, of the department Multi-Scale Physics (MSP), of the Delft University of Technology, Delft, The Netherlands. In January 2011, he returned to China and worked as research assistant in Shanghai Jiaotong University. Now Xie is the R&D engineer of high-pressure pump at Bosch Automotive Diesel System Co., Ltd.

Xie's hobbies include traveling, soccer and photography. He is married to Wang Yi. They have one son, Xie Qinglin, born in Delft in 2010. Xie can be reached at xie_mengmeng@hotmail.com.